Identifying Supersymmetry at the CERN LHC and Indirect Dark Matter Detection Experiments

by
Phillip R. Grajek

A dissertation submitted in partial fulfillment
of the requirements for the degree of
Doctor of Philosophy
(Physics)
in The University of Michigan
2009

Doctoral Committee:

Professor Gordon L. Kane, Chairperson
Professor Dante E. Amidei
Associate Professor James T. Liu
Assistant Professor Oleg Y. Gnedin
Assistant Professor Aaron T. Pierce

© Phillip Grajek 2009
All Rights Reserved

To Mom & Dad, and my sister Michelle

ACKNOWLEDGEMENTS

First, I wish to thank my advisor Gordon Kane, for accepting me as his student, and for giving me the opportunity to pursue advanced study in this rich and fascinating area of physics.

I also wish to thank James Wells and Jim Liu, for advice and encouragement early on.

I wish to thank my collaborators: Bobby Acharya, Baris Altunkaynak, Michael Holmes, Eric Kuflik, Brent Nelson, Dan Phalen, Aaron Pierce, Kerim Suruliz, Lian-Tao Wang, and Scott Watson, without whom this work would not have been possible. In particular, I have to give special thanks to Scott Watson, for inspiring me with your enthusiasm for physics, and numerous, stimulating discussions about both research and life.

I must also thank Gabriel Rebeiz, and all of my old friends from the RADLAB, for teaching me how to sail into the storm with confidence.

Finally, I must express my immense gratitude to my Mom and Dad, and my sister Michelle, for your absolute unwavering support and encouragement, and for always believing in me. None of this could have ever been accomplished without you.

TABLE OF CONTENTS

LIST OF FIGURES

Figure

LIST OF TABLES

Table

CHAPTER I

Introduction

The CERN Large Hadron Collider will begin operations by the end of 2009, and will mark the beginning of a new era of particle physics: one where we expect to resolve the mechanism responsible for electroweak symmetry breaking, potentially obtain evidence for new physics beyond the Standard Model, and transition from a period of model-building and speculation to one focused on measurement and verification. While the Standard Model (SM) accurately describes the interactions of observed fundamental particles and forces at energies up to ~ 1 TeV, several issues neccesitate the viewpoint that the SM is incomplete and is instead at best an effective description of a more fundamental theory. Over the last two decades, significant efforts have been made at attempting to solve these issues, as well as extending the SM to higher energy scales. Interestingly, while this research has produced numerous viable models for new physics, none have emerged completely satisfactory from from either a theoretical or phenomenological perspective. However, among the possibilities, arguably the most well-motivated model is supersymmetry (SUSY). SUSY provides a solution to the so-called Hierarchy Problem [1], and allows for dynamical breaking of the electroweak gauge symmetry [2]. Additionally, the SUSY interactions allow the gauge couplings to unify at scale $M_{GUT} \sim 2 \times 10^{16}$ GeV [3],

suggesting that if SUSY is verified, we will immediately understand something about the nature of physics at energy scales far beyond the reach of experiment. With the LHC turn-on imminent, the opportunity to test these ideas has finally arrived.

This thesis focuses on the phenomenological challenge of both identifying SUSY at experiments, and then extracting as much meaningful information regarding its fundamental parameters as possible. Specifically, the work presented here is concerned with the LHC, as well as several astrophysical observation experiments which may be sensitive to a supersymmetric dark matter. As we will discuss shortly, there is strong reason to believe that if nature is indeed supersymmetric, it will be observed at the LHC. Consequently, searches for SUSY are among the primary tasks of the LHC program. However, much of the work in this area has focused on canonical scenarios such as mSUGRA [4], which contain underlying assumptions that greatly reduce the number of unknown parameters. At the LHC, these models often predict long cascade decay sequences, which may be observable through characteristic end-point features in invariant mass distributions [5]. Most people expect, however, that supersymmetry will not present itself in this simple form. It is therefore crucial to explore the implications of SUSY in as many manifestations as possible, in order to facilitate its identification when data becomes available. The remainder of this introduction continues with a concise review of the Hierarchy Problem associated with the Standard Model, and motivates supersymmetry as an elegant solution. This chapter concludes with a discussion about the challenges associated with SUSY phenomenology.

1.1 What we know thus far: The Standard Model

Our current understanding of interactions between the observed fundamental particles and forces is encapsulated in the Standard Model (SM). The SM has been tested experimentally to high precision both at LEP, and more recently at the Tevatron up to energies of approximately 1 TeV. Remarkably, precision measurements at LEP have tested the SM to below the percent level [6], and therefore with sufficient sensitivity to observe deviations from tree-level predictions that arise from quantum mechanical effects. Therefore, the SM has been verified as a quantum theory of particle interactions.

Formally, the SM is a non-abelian gauge theory with invariance under the $U(1)_Y \times SU(2)_L \times SU(3)_C$ symmetry group. Here subscript Y refers to weak hyper-charge, subscript L left-handedness, and subscript C color charge. The $U(1)_Y \times SU(2)_L$ gauge group defines the electroweak interactions, while the $SU(3)_C$ group defines the strong interactions (QCD). All matter fields are charged under $U(1)_Y$. The left-handed helicity component of each lepton and associated lepton-neutrino, and each "up" and "down" quark pair transform as doublets under $SU(2)_L$, while the right-handed components are $SU(2)_L$ singlets. The SM does not incorporate a right-handed neutrino. The quarks transform as color triplets under $SU(3)$, while the leptons remain singlets. Demanding the lagrangian remain invariant under *local* transformations necessitates the introduction of spin 1 vector bosons which mediate the interaction between matter fields (i.e. they enact the rotation between states within a particular multiplet). These gauge fields realize the fundamental forces which physically mediate the interactions. It is remarkable that invariance under certain symmetries not only leads to an organizing principle that configures the

particle interactions, but also appears to explain the origin of at least three of the four fundamental forces.

This framework contains several important attributes. First, the most general form of the SM lagrangian that maintains invariance under $U(1)_Y \times SU(2)_L \times SU(3)_C$ also automatically conserves baryon-number and lepton-number, as observed in nature. Additionally, the particle content is precisely that necessary to ensure cancellation of anomalies (these are conditions whereby an interaction satisfies gauge invariance at tree level, but ultimately is non-invariant as soon as one goes to the 1-loop level). One critical feature of the SM is that it is a chiral theory, meaning that the left- and right-handed helicity eigenstates of each Dirac fermion reside in different representations, and thus transform differently under the gauge symmetry. This behavior protects matter fields from acquiring arbitrarily large masses, since Dirac mass terms $m\bar{\psi}\psi = m\bar{\psi}_L\psi_R + m\psi_L\bar{\psi}_R$ are then forbidden by gauge symmetry, ultimately forcing mass generation through spontaneous symmetry breakdown. In the SM this is accomplished through the Higgs mechanism [7], whereby a fundamental scalar doublet Φ is introduced that is allowed to acquire a vacuum expectation value (vev). This initiates the breaking of the electroweak symmetry $U(1)_Y \times SU(2)_L$ down to $U(1)_{EM}$, thereby preserving the abelian gauge symmetry associated with electromagnetism, while simultaneously generating masses of order $\mathcal{O}(EW)$ scale as observed at experiment.

One significant departure from experiment, however, comes from the fact that neutrinos have been observed to have non-vanishing mass. The SM as described above incorporates no provision for neutrino masses: A right-handed neutrino field ν_R is not included, having not been observed directly. However, neutrino masses can be accommodated in the SM while still preserving the full gauge symmetry

through the so-called seesaw mechanism [8], which introduces a new physical scale at $M_{new} \sim 10^{14}$ GeV (in this case the scale where it is possible to excite quantum fluctuations corresponding to a new super-massive neutrino).

Another departure from experiment comes from the fact that astrophysical observations suggest the presence of non-luminous dark matter (DM) in the universe. The exact composition of the DM is currently unknown. A well-motivated possibility is that DM is composed of weakly interacting massive particles (WIMPs). The SM does not contain a satisfactory DM candidate particle. As we will discuss shortly, the most promising DM candidate particles are predicted by models that extend the SM, and which also introduce new physics at often much higher energy scales.

The question of additional structure above ~ 1 TeV is fundamentally important. At what scale does this picture of the SM break down, and if it does break down, what new physics comes into play? The SM as described has a total of 19 free parameters. These are the three gauge coupling constants, the Higgs-sector parameters μ and λ, 6 quark masses and 3 lepton masses, 3 mixing angles and 1 CP-violating phase, and the QCD parameter θ. Additionally, we expect new physics near the Planck scale, M_{pl}, where it is assumed that gravitational effects will become important. Therefore one may imagine that the SM, augmented with neutrino masses, should hold all the way to the Planck scale, with no additional structure other than the Higgs and a massive neutrino, and that above M_{pl} new physics enters which then fixes the 19 free parameters of the theory. However, the SM has several unresolved issues, for which the solutions usually introduce new physics far below the Planck scale. In what follows we review the most important issue relevant to the work in this thesis, the Hierarchy Problem.

1.2 The Hierarchy Problem

The Higgs mechanism of the SM relies on the inclusion of a fundamental scalar (the Higgs field) which is allowed to acquire a vev and break the electroweak symmetry. However, at the same time, higher order couplings of this scalar to other massive fields can actually destabilize the theory. Let us explore this issue with greater detail, in order to see how it specifically causes problems. Consider the complex scalar Higgs doublet Φ, parametrized as

$$\Phi = \begin{pmatrix} \phi^+ \\ \frac{1}{\sqrt{2}}(v + h + i\phi^0) \end{pmatrix} \tag{1.1}$$

which has a classical potential given by

$$V = \mu^2 \Phi^\dagger \Phi + \lambda (\Phi^\dagger \Phi)^2 \tag{1.2}$$

Here μ is the scalar mass-squared parameter, and λ a coupling. Electroweak symmetry breakdown occurs when the minimum of the potential is non-vanishing. This occurs for $\mu^2 < 0$, and $\lambda > 0$. The minimum occurs at $\Phi^\dagger \Phi = v^2/2$, where $v = \sqrt{-\mu^2/\lambda}$. Setting the Goldstone fields $\phi^+ = \phi^0 = 0$, and expanding about the vacuum, one finds for the Higgs field h the mass term $2\mu^2 h^2 = m_0^2 h^2$, where m_0 is the tree-level (bare) Higgs mass in the absence of additional physics. LEP precision measurements of the W and Z masses require that the vacuum expectation value $\langle \phi \rangle \equiv v/\sqrt{2} \sim 174$ GeV. Therefore, assuming a natural Yukawa coupling of $\mathcal{O}(1)$ we expect that m_0^2 should be order $-(100\ GeV)^2$. Now, the SM provides no prediction for the Higgs mass parameter itself. (Unitarity of longitudinal WW scattering implies a bound on the physical Higgs mass $m_h \lesssim 1$ TeV.) However, it is necessary to examine corrections to m_0^2 due to contributions from quantum effects that arise from all the fields that

couple directly or indirectly to the Higgs. For example, considering the Higgs self coupling

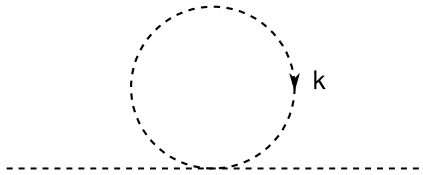

one obtains the correction to m_0^2

$$\delta m_0^2 = \lambda \int^{\Lambda} \frac{d^4k}{(2\pi)^4} \frac{1}{k^2} \sim \frac{\lambda}{16\pi^2} \int^{\Lambda} dk^2 \tag{1.3}$$

which is of order $\lambda\Lambda^2/16\pi^2$ and diverges quadratically with Λ. Thus $m_h^2 = m_0^2 + \alpha\lambda\Lambda^2/16\pi^2$, where α is a number of order 1, m_0 is the bare mass, and m_h is taken as the physical Higgs mass (we have neglected other possible corrections). Here Λ is a cut-off which regulates the integral. From the perspective of an effective theory, one must treat Λ as a *physical* cut-off, at which point it is expected that new physics will begin to take over. Were it possible to take $\Lambda \to \infty$, technology such as dimensional regularization could be used to remove the divergence. Thus, if we take the SM to be an effective theory up to some physical threshold Λ, we must assume a finite cut-off, and the quadratic divergence persists. This scenario leads to an interesting problem because now the quantum corrections become highly sensitive to the cut-off scale, which we want to take as high as possible. Taking Λ to be the unification scale, for example, generates a contribution to δm_0^2 that is many orders of magnitude larger than the fundamental parameter (bare mass) m_0^2. Now, let us rewrite the contribution to m_h as

$$\frac{m_0^2}{\Lambda^2} = \frac{m_h^2}{\Lambda^2} - \alpha\frac{\lambda}{16\pi^2} \tag{1.4}$$

If we take $\Lambda \sim M_{pl} \sim 10^{19}$ GeV, and $m_h \sim 100$ GeV, m_0^2/Λ^2 must be tuned to 30 orders of magnitude in order to provide the physical Higgs mass suggested from measurements. Many consider such extreme fine-tuning to be 'unnatural'. Indeed, one normally expects corrections due to higher-order quantum effects to only *slightly* modify the fundamental parameters (here the bare Higgs mass). In the SM, the 1-loop contribution to the Higgs mass correction comes from [9]

$$\delta m_0^2 = \frac{3\Lambda^2}{8\pi^2 v^2}\left[(4m_t^2 - 2M_W^2 - M_Z^2 - m_0^2) + \mathcal{O}(log\frac{\Lambda}{\mu})\right] \tag{1.5}$$

where here μ is understood to be the renormalization scale. This correction includes contributions from the W and Z, the Higgs self coupling above, and the top-quark. In fact, the largest contribution to δm_0^2 comes from the top quark, indicating that the corrections are sensitive to both the largest mass scales, as well as the physical cut-off. One may imagine engineering $2M_W^2 + M_Z^2 + m_0^2 = 4m_t^2$, which then removes the quadratic divergence. This is known as the Veltman condition [9]. Unfortunately, it is guaranteed not to hold at higher orders. Additionally, when $\Lambda \gtrsim 100$ TeV, undesirable fine-tuning once again is required. One can also imagine simply choosing a lower cut-off, but then it still becomes necessary to devise new physics which takes over at that scale.

What then is the natural scale of m_h, and if $m_h \lesssim 1$ TeV, what mechanism protects it from large quantum corrections? This extreme disparity of scales is known as the Hierarchy Problem, and significant effort has gone towards attempting to find a viable solution. A particularly elegant approach is to arrange for a cancellation that eliminates the quadratic divergences. For example, consider the correction to the Higgs due to a fermion loop

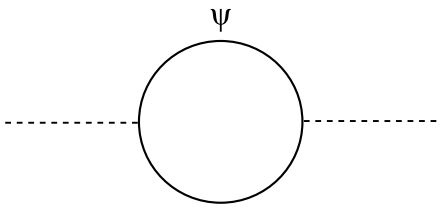

One obtains for the correction

$$\delta m_0^2 = -\frac{|\lambda_f|^2}{8\pi^2}\,\Lambda^2 + \cdots \tag{1.6}$$

where again Λ is the physical cut-off of the theory, and λ_f is the coupling strength associated with the fermion. The critical feature is that here the fermion loop introduces a minus sign relative to the contribution obtained for the scalar self-coupling above. This suggests that by introducing a special relationship between bosons and fermions it is possible cancel out the unwanted quadratic divergences.

1.3 Supersymmetry

By appealing to an idea known as supersymmetry, the cancellation discussed in the previous section is precisely what occurs. A complete treatment of supersymmetry is beyond the scope of this modest introduction. The reader is invited to consult the several excellent references and reviews (see e.g. [10, 11]). Under supersymmetry (SUSY), one postulates the existence of an additional global symmetry relating bosonic and fermionic degrees of freedom. Noether's theorem then implies that invariance of the action under such symmetry transformations leads a conserved current, which here is represented by a generic 4-current J^μ_α with spinorial index α. In this case the current is referred to as a *supercurrent.* From this it is possible to construct a conserved charge

$$Q_\alpha = \int J^0_\alpha d^3x \tag{1.7}$$

which becomes the generator of the SUSY transformation

$$Q\,|f\rangle = |b\rangle \tag{1.8}$$

$$Q\,|b\rangle = |f\rangle \tag{1.9}$$

where $|b\rangle$ and $|f\rangle$ represent bosonic and fermionic states, respectively. The SUSY generator Q_α must have fermionic degrees of freedom because it transforms between fields with integer-spin and fields that are spinorial (spin 1/2). Thus Q is a spinorial object, with spin 1/2 and index α. This implies that $Q^\dagger_{\dot\alpha}$ is also a generator of the symmetry, since spinors are inherently complex objects. It is possible to construct models where there are $N > 1$ sets of generators Q, $Q^\dagger$, corresponding to additional symmetries. These 'extended' supersymmetry models are not phenomenologically viable because they are unable to correctly model the chiral properties present in the SM. In what follows we restrict ourselves to $N = 1$, or only a single set of supersymmetry generators.

Now, the single particle states of supersymmetry are grouped into irreducible representations of the symmetry transformation known as *supermultiplets*. These carry both fermionic and bosonic degrees of freedom by construction. The corresponding fields are known as *superpartners* of each other. The generators Q_α and $Q^\dagger_{\dot\alpha}$ transform between the fields within the supermultiplet. The SUSY generators also commute with the generators of gauge transformations, so the members of a supermultiplet reside in the same representation of the gauge symmetry, and therefore have identical charge, weak iso-spin, and color charge.

Chiral Supermultiplet		Spin 0	Spin 1/2
quarks, squarks	Q	$(\tilde{u}_L,\, \tilde{d}_L)$	$(u_L,\, d_L)$
	$\bar{u}$	$\tilde{u}^*_R$	$u^\dagger_R$
	$\bar{d}$	$\tilde{d}^*_R$	$d^\dagger_R$
leptons, sleptons	L	$(\tilde{\nu}_L,\, \tilde{e}_L)$	$(\nu_L,\, e_L)$
	$\bar{e}$	$\tilde{e}^*_R$	$e^\dagger_R$
Higgs, Higgsinos	H_u	$(H^+_u,\, H^0_u)$	$(\tilde{H}^+_u,\, \tilde{H}^0_u)$
	H_d	$(H^-_d,\, H^0_d)$	$(\tilde{H}^-_d,\, \tilde{H}^0_d)$

Table 1.1: Chiral supermultiplets for the MSSM. Superpartner fields are differentiated from their SM counterparts with a '$\sim$'.

Gauge Supermultiplet	Spin 1/2	Spin 1
gluon, gluino	$\tilde{g}$	g
W bosons, winos	$\tilde{W}^\pm,\, \tilde{W}^0$	$W^\pm,\, W^0$
B boson, bino	$\tilde{B}^0$	B^0

Table 1.2: Gauge supermultiplets for the MSSM. Superpartner fields are differentiated from their SM counterparts with a '$\sim$'.

The simplest supermultiplet consists of a Weyl fermion containing 2 spin degrees of freedom, and a complex scalar with 2 additional real degrees of freedom. This is the only supermultiplet that allows the left- and right-handed helicity eigenstates to transform differently under the gauge symmetry, and is known as a *chiral supermultiplet*. Another supermultiplet, which is equally fundamental, consists of a massless vector field containing 2 transverse spin degrees of freedom, and a single Weyl fermion with again 2 additional degrees of freedom, and is known as a *gauge supermultiplet*. These two supermultiplets are irreducible. Other ways of organizing the particle states can always be reduced to these two fundamental forms. Extending the SM to incorporate supersymmetry requires organizing the SM fields into various supermultiplets, and thus requires that each field acquire a superpartner having spin which differers by 1/2. Tables 1.1 and 1.2 indicate the particle content and organization of supermultiplets for the so-called minimal example of the supersymmetric extension of the Standard Model, known as the MSSM.

The nomenclature used to identify the non-SM superpartners from their SM counterparts involves prepending an 's-' for scalar superpartners, and adding the suffix '-ino' for fermionic superpartners. Under this convention, the scalar superpartners of the SM quarks and leptons are known as squarks and sleptons, respectively. Similarly, the fermionic superpartners of the gauge bosons are collectively known as gauginos. The superpartner to the gluon is known as the gluino, while those for the W and B fields are known as the wino and bino, respectively. In addition, it is normal to distinguish the non-SM superpartner field symbols by including a '$\sim$'. From the tables one can see that gauge multiplets in the SM are combined with multiplets composed of superpartner fields in order to form a supermultiplet. For example, the $SU(2)_L$ doublet $(u_L,\ d_L)$ is combined with another $SU(2)_L$ doublet $(\tilde{u}_L,\ \tilde{d}_L)$ composed of the squark superpartners to form a supermultiplet labeled here as Q. The $SU(2)_L$ singlet quarks u_R and d_R are separately combined with new scalar singlets $\tilde{u}_R$ and $\tilde{d}_R$ to form two additional supermultiplets. Notice that the subscripts L and R attached to the symbols for the scalar particles is only part of the particle name, and does not indicate any sort of helicity projection. This organization scheme is repeated similarly for the leptons/sleptons, and gauge bosons/gauginos, and for each family.

Notice that the Higgs sector contains two supermultiplets, each containing a set of Higgs doublets. Under SUSY it is necessary to include two Higgs supermultiplets in order to ensure that the interaction lagrangian is invariant under supersymmetry transformations (one must ensure the superpotential is an analytic function of the complex scalar fields). Additionally, the model would suffer from a gauge anomaly, and it turns out that only a Higgs doublet with hypercharge $Y = +1/2$ can give mass to $+2/3$ charged quarks, while a doublet with $Y = -1/2$ can only give mass to

$-1/3$ charged quarks.

The framework described above makes an interesting prediction. In order to maintain chiral symmetry as required by the SM, the SUSY generators Q_α and $Q^\dagger_{\dot\alpha}$ must satisfy the following algebra

$$\{Q_\alpha, Q^\dagger_{\dot\alpha}\} = -2\sigma^\mu_{\alpha\dot\alpha} P_\mu \tag{1.10}$$

$$\{Q_\alpha, Q_\beta\} = \{Q^\dagger_{\dot\alpha}, Q^\dagger_{\dot\beta}\} = 0 \tag{1.11}$$

$$\{P^\mu, Q_\alpha\} = \{P^\mu, Q^\dagger_{\dot\alpha}\} = 0 \tag{1.12}$$

Consider two states $|b\rangle$ and $|f\rangle$, with mass eigenvalues m_b and m_f respectively, which reside in the same supermultiplet. From the relations above one finds $[Q_\alpha, P^\mu P_\mu] = 0$. Then

$$\begin{aligned} P^\mu P_\mu Q_\alpha |b\rangle = P^\mu P_\mu |f\rangle = m_f^2 |f\rangle \\ = Q_\alpha P^\mu P_\mu |b\rangle = m_b^2 Q_\alpha |b\rangle = m_b^2 |f\rangle \end{aligned} \tag{1.13}$$

Thus, each member of a particular supermultiplet has the same mass. Clearly this is not allowed phenomenologically, since if supersymmetry were manifest in the particle spectrum, the superpartners would have all been observed quite some time ago. This indicates that SUSY must be a broken symmetry in our vacuum.

It is possible to evade such a phenomenological disaster, however. Notice that for the desired cancellations to occur (which remove the quadratic divergence in δm_0^2), the associated coupling strengths must be properly related to one another. For example, λ and λ_f^2 from eqns. (1.3) and (1.6), should be the same magnitude. If this is not the case the theory will retain residual terms proportional to $(\lambda - \lambda_f^2)\Lambda^2$

and nothing has been gained. It is possible to introduce a shift which lifts the undiscovered superpartner masses to levels allowed by current experimental bounds, while preserving the critical relationships between coupling strengths if we introduce supersymmetry violating terms to the lagrangian in a careful way. Let us write the full lagrangian as

$$\mathcal{L} = \mathcal{L}_{SUSY} + \mathcal{L}_{soft} \tag{1.14}$$

where $\mathcal{L}_{SUSY}$ contains all interactions that explicitly preserve supersymmetry, while $\mathcal{L}_{soft}$ contains only mass-shift terms for superpartner scalars, pseudo-scalars, gauginos, and trilinear couplings that violate supersymmetry. The free parameters of $\mathcal{L}_{soft}$ are known as the 'soft parameters'. Crucially, $\mathcal{L}_{soft}$ *does not* contain mass terms for non-gaugino fermions. Such terms disrupt the cancellation and allows unwanted quadratic divergences to persist. This so-called 'soft breaking' of SUSY allows the critical relationships between the couplings to be maintained, thereby preserving the cancellation of quadratic divergences for all scalar fields. This scheme introduces additional divergences but these only scale logarithmically with Λ. For example, if m_{soft} is the largest mass scale associated with the soft parameters, the contributions to δm_0^2 now go like

$$\delta m_0^2 = m_{soft}^2 \left[\frac{\lambda}{16\pi}^2 ln(\Lambda/m_{soft}) + \cdots \right] \tag{1.15}$$

This provides the greatest motivation for the expectation that at least some of the superpartners should be detected at the LHC, since m_{soft} cannot be too large or else we re-introduce large divergences again, and destroy any progress at stabilizing the scalar fields.

It may appear that breaking SUSY in this manner is somewhat contrived. However, it is possible to dynamically generate the $\mathcal{L}_{soft}$ terms nonperturbatively from a more fundamental framework, such as string theory (See [10] for a discussion).

The full soft lagrangian for the MSSM is given by

$$\begin{aligned}
\mathcal{L}_{soft} &= -\frac{1}{2}\left(M_3\tilde{g}\tilde{g} + M_2\tilde{W}\tilde{W} + M_1\tilde{B}\tilde{B} + c.c.\right) \\
&\quad -\left(\tilde{\bar{u}}\mathbf{a_u}\tilde{Q}H_u - \tilde{\bar{d}}\mathbf{a_d}\tilde{Q}H_d - \tilde{\bar{e}}\mathbf{a_e}\tilde{L}H_d + c.c.\right) \\
&\quad -\tilde{Q}^\dagger\mathbf{m_Q^2}\tilde{Q} - \tilde{L}^\dagger\mathbf{m_L^2}\tilde{L} - \tilde{\bar{u}}\mathbf{m_{\bar{u}}^2}\tilde{\bar{u}}^\dagger - \tilde{\bar{d}}\mathbf{m_{\bar{d}}^2}\tilde{\bar{d}}^\dagger - \tilde{\bar{e}}\mathbf{m_{\bar{e}}^2}\tilde{\bar{e}}^\dagger \\
&\quad -m_{H_u}^2 H_u^* H_u - m_{H_d}^2 H_d^* H_d - (bH_uH_d + c.c.)
\end{aligned} \tag{1.16}$$

where we recognize the superpartners indicated in tables 1.1 and 1.2. The first line contains M_1, M_2, and M_3, which are the mass parameters for the bino, wino, and gluino, respectively. The second line contains trilinear coupling terms, where each of $\mathbf{a_u}$, $\mathbf{a_d}$, and $\mathbf{a_e}$ is a complex 3×3 matrix in family space. The third line contains mass terms for the squarks and sleptons. Each of the $\mathbf{m_Q}$, $\mathbf{m_L}$, $\mathbf{m_{\bar{u}}}$, $\mathbf{m_{\bar{d}}}$, and $\mathbf{m_{\bar{e}}}$ are also complex 3×3 matrices in family space. In this case they must be hermitian so that the total lagrangian is remains real. The last line contains the only allowed mass terms for the Higgsino fields. This lagrangian also assumes the existence of a separate discrete symmetry known as R-parity. Each particle of the theory carries a new quantum number given by

$$P_R = (-1)^{3(B-L)+2s} \tag{1.17}$$

where B and L are lepton- and baryon-number, respectively, and s is the particle spin. Under this new symmetry, the SM fields all have even R-parity, while the super-

symmetric partners have odd R-parity. In the MSSM it is assumed that interactions conserve R-parity. The implications of this are described in what follows.

An interesting feature of this lagrangian is that the interactions allow mixing between the interaction eigenstates. In other words, the superpartners are not necessarily the mass eigestates of the model. Mixing can occur among the sleptons, the squarks, as well as the gauginos and Higgsinos. Only the gluino does not mix with any other field because no other color-octet fermion field exists. Of particular importance to SUSY phenomenology is the mixing that occurs between the neutral $\tilde{B}^0$, $\tilde{W}^0$, and $\tilde{H}_u^0/\tilde{H}_d^0$ fields. Diagonalizing the resulting mass matrix yields mass eigenstates in a new basis denoted as $(\tilde{N}_1,\ \tilde{N}_2,\ \tilde{N}_3,\ \tilde{N}_4)$, which are commonly known as neutralinos. By convention, $m_{\tilde{N}_1} < m_{\tilde{N}_2} < m_{\tilde{N}_3} < m_{\tilde{N}_4}$. The lightest state, $\tilde{N}_1$ is often also the *Lightest Supersymmetric Particle*, or LSP. By demanding that interactions conserve R-parity as described above, the LSP must be stable. This allows the neutralino LSP to have precisely the features required to be a good candidate for cold dark matter in the universe. The fact that a neutralino LSP is composed of an admixture of bino, wino, and Higgsino fields leads to rather challenging phenomenological questions, since this admixture affects the abundance of such particles if produced in the early universe, as well as the nature of new-physics signatures at colliders.

1.4 The Challenge of SUSY Phenomenology

Combined, the soft breaking terms in eq. (1.16) introduce an additional 105 free parameters that must ultimately be set by a more fundamental theory. It may appear that we have taken a step backwards: Relative to the 19 free parameters of the SM, the MSSM introduces considerable uncertainty into the ultimate form that $\mathcal{L}_{soft}$ can

take. In principle, these parameters are calculable from any fundamental theory, such as string theory. However in order to identify what physics operates at energy scales where such ideas become important, we must first determine the soft parameters. Given that we have not observed any of the superpartners, we have significantly less information from which to constrain the form of $\mathcal{L}_{soft}$. Additionally, given that models of dynamical SUSY breaking that generate the soft terms do so at scales far beyond the reach of any experiment, we must infer as much as possible only from low-energy measurements. Ultimately, the mass splittings between the SM fields and their superpartners are controlled by the soft-parameters in $\mathcal{L}_{soft}$. Therefore, a particular choice of soft parameters gives rise to a low-scale superpartner spectrum, and thus controls the nature of phenomenology at experiments. By measuring as much of the spectrum as possible, we hope to gain an understanding of the soft terms, and ultimately the form of the fundamental SUSY lagrangian. This, in turn, may then dictate the nature of physics at very high scales, where the soft-parameters are ultimately generated. Herein lies the core focus of SUSY phenomenology, and the underlying purpose for the work presented in this thesis. This task is particularly difficult, however, because the mapping from SUSY parameter space to experimental signature space is not $1:1$. More specifically, it is in fact highly likely that differing choices for the parameters in $\mathcal{L}_{soft}$ (different models) may yield effectively identical signatures at experiments like the LHC, despite the fact that the models are distinct in that they describe completely different physical situations [12]. This problem is not specific to SUSY model variations either. Several other viable alternatives that propose to extend the SM may also produce signatures that are extremely difficult to distinguish from SUSY, or variations within their own framework. This challenge is collectively known as the 'Inverse Problem', and no unique solution exists.

The approach taken in this thesis, and by the community at large, is to explore the implications of these models at as many experiments as is possible, so one can constrain the parameter space as thoroughly as possible. Additionally, much work has gone towards untangling the signatures themselves, so that degenerate signals become distinct, and can then highlight specific physical scenarios. The work of this thesis contributes to this effort. In the following chapters we present several novel approaches to the problem of determining parameters of the fundamental lagrangian from experimental measurements.

This thesis is organized as follows. In Chapter II we study methods for identifying the challenging scenario whereby gluino pair production at the LHC gives rise to up to four top-quarks in the final state. In Chapter III we address the problem of identifying gaugino mass parameter universality using only simple sets of LHC signatures. In Chapter IV we depart from the LHC and study the role non-thermally produced, wino-like dark matter can play in explaining the positron excess reported by the HEAT and AMS experiments. In Chapter V we revisit the model presented in Chapter IV in light of the recent PAMELA satellite data, and discuss constraints on wino-like non-thermal dark matter. Finally, in Chapter VI we present conclusions and directions for future work.

The discussion in Chapter II is based on [13], done in collaboration with Bobby Acharya, Gordon Kane, Eric Kuflik, Kerim Suruliz, and Lian-Tao Wang. The discussion of Chapter III is based on [14], done in collaboration with Baris Altunkaynak, Michael Holmes, Gordon Kane, and Brent Nelson. Chapters IV and V are based on [15, 16], in collaboration with Gordon Kane, Dan Phalen, Aaron Pierce, and Scott Watson.

CHAPTER II

Multiple Top-Quark Reconstruction at the LHC

The first step towards identifying and interpreting discoveries at the LHC is to establish the presence of new physics beyond the Standard Model. In practice, this will be done using search strategies that are by now well established. However, it is highly possible, and perhaps probable that new physics will appear in a form that is very different than what these methods were designed for. In this chapter, we address the issue of observing and identifying an interesting and particularly difficult signal for new physics. Specifically, we consider that many scenarios for new physics at the TeV scale point toward top rich final states at the LHC. Such scenarios include top compositeness [17], and models in which top partners ensure the naturalness of electroweak symmetry breaking [18, 19, 20, 21]. Compared with the Standard Model QCD production of $t\bar{t}$, top quarks in the final states of new physics production typically either have very different kinematics [22, 23, 24], or different event topology [25, 27, 28, 26, 29], which may make it crucial to develop new techniques to identify them.

Naturalness of the electroweak symmetry breaking typically requires the existence of a light top partner. Additionally, experimental observations, ranging from the existence of Cold Dark Matter in the universe to the constraints of electroweak

precision measurements, strongly motivates the existence of a neutral stable particle. Several scenarios for new physics predict that such particles will be produced at the LHC. These considerations lead to the recent studies of new physics signals with $t\bar{t} + \not{E}_T$ final state [25].

In this chapter, we consider scenarios which also include a gluon partner, such as the gluino in low energy supersymmetry [18, 30], the KK-gluon in universal extra dimension models [19], or other octet states [31, 32, 33]. Due to the nature of proton colliders, production of such color octet gluon partners and their decay typically becomes the main channel of new physics signals. Decay products of the gluon partner typically include an even number of quarks. Combining this scenario with light top partners, we conclude that a typical signature of production of gluon partners will be multiple top quarks in the final states.

In the rest of this chapter, we will study this signature using a particular example, low energy supersymmetry with light gluinos. We will focus on the scenario in which the squarks are heavier than the gluino and the third generation squarks are lighter than those of the first two generations. In this case, the gluino will dominantly decay into top (bottom) quarks. Although not absolutely unavoidable, this is a generic possibility from the point of view of many models being studied recently [35, 34, 36, 37]. Heavier first- and second-generation squark masses are often preferred due to constraints from flavor changing neutral currents [38, 39, 40]. RGE running of scalar masses from the high scale down to the electroweak scale will tend to push the third generation squark masses significantly lower than those of the other generations. Large third generation trilinear couplings will also help further lower one of the stop masses. For earlier studies on gluino decay into third generation quarks, see Refs. [41, 42, 43, 44, 45, 46, 47].

In the minimal case, this scenario has only a single, light top partner, $\tilde{t}_R$. On the other hand, we would like to include in our study the possibility that all the squarks of the full third generation could be light relative to the other two generations. Therefore, we are led to consider decay channels $\tilde{g} \to t\bar{t}\tilde{\chi}^0$, $\tilde{g} \to t\bar{b}\tilde{\chi}^{\pm}$, and $\tilde{g} \to b\bar{b}\tilde{\chi}^0$. As will be clear from our discussion later, many of the leading order features of the signature of different combinations of the above decay channels (from gluino pair production and decay) can be quite similar. Therefore, it is one of the primary purposes of this chapter to study techniques to distinguish them. We remark that such measurement is crucial for understanding both the spectrum of the third generation sfermions and the electroweak-inos. For example, if we measure a non-zero branching ratio for the decay channel $\tilde{g} \to t\bar{b}\tilde{\chi}^{\pm}$, then there must be a light electroweak-ino carrying charge, suggesting that the lightest supersymmetric particle (LSP) has primarily wino/higgsino composition. Moreover, the relative branching ratio $BR(\tilde{g} \to t\bar{t} + \tilde{\chi}^0)/BR(\tilde{g} \to b\bar{b} + \tilde{\chi}^0)$ carries important information about the squark masses. For example, if this ratio is close to 1, it strongly suggests that left-handed squark masses are lighter than the right-handed ones, $m_{\tilde{Q}_3} < m_{\tilde{t}_R},\ m_{\tilde{b}_R}$.

In section 2.2, we will focus on discovering new physics in this class of final states. Decay of multiple top quarks could lead to b-rich and lepton rich final states. Therefore, we expect great potential for early discovery. For example, we show that significant excesses can be observed in many channels even with just 500 pb^{-1} of data. The obvious channel with the best early discovery potential is same-sign dilepton plus additional b-tags.

In section 2.3, we study the problem of direct reconstruction of top quarks. Large combinatorics and high probability of object merging are expected due to the large multiplicity of final state particles. Therefore, while we may gather evidence from

this study that there are *some* top quarks in the decay chain of the gluino, similar to the approaches taken in Ref. [42, 43, 31], the direct reconstruction efficiency for the top quark is low. We find that while the efficiency for reconstructing a single top quark candidate approaches 49%, the efficiency to detect three and four candidates drops dramatically to 1.5% and 0.02%, respectively. As a result, it is less likely we can measure top multiplicity by direct reconstruction.

We will demonstrate in our study a fitting procedure which could allow us to measure the branching ratios of different gluino decay channels. We begin by simulating a number of samples of gluino pair production and decay, each with different final states, such as *tttt*, *tttb*, *ttbb*, and so on. Then we will fit the relative weights of different samples to match a set of experimental signatures. Of course, without precise knowledge of the underlying spectrum, choice of the templates will introduce errors in the estimate of the branching ratios. We studied such effects by using several templates with different hypotheses for the relevant masses. We conclude that such a method will allow us to establish important features of gluino branching ratios.

We carry out our study on several benchmark models with relatively low gluino masses. A detailed scan of the parameter space involving the gluino mass and different branching ratios is beyond the scope of this study. The corresponding results for heavier gluino masses (but with similar decay branching ratio and mass difference between gluino and the LSP) could be roughly obtained by scaling from the present result using relative production cross sections. The mass gap between the gluino and the neutralino or chargino in the next step of the decay chain could also have important effects as it will affect the detection efficiency of various decay products. In general, a larger mass gap will enhance the discovery potential. At the same time, we expect this effect is milder in comparison with the dependence on the gluino mass.

	Model parameters (TeV)							Branching ratios		
	$m_{\tilde{g}}$	$m_{\tilde{q}_{1,2}}$	$m_{\tilde{t}_1}$	$m_{\tilde{t}_2}$	$m_{\tilde{b}_1}$	$m_{\tilde{b}_2}$	$m_{\tilde{N},\tilde{C}}$	$(\tilde{g} \to t\bar{t})$	$(\tilde{g} \to b\bar{b})$	$(\tilde{g} \to tb)$
A	0.65	8	1.3	8	2.5	8.1	0.1	0.92	0.07	0
B	0.65	4	0.8	0.93	0.87	4	0.1	0.71	0.27	0
C	0.65	4	0.64	0.9	0.72	4	0.1	0.52	0.47	0
D	0.65	4	0.63	0.9	0.72	4	0.1	0.09	0.22	0.69

Table 2.1: Model spectra and relevant branching ratios for the benchmark models considered in this study. The models A, B, and C the only particle state lighter than the gluino is the LSP, which is taken as a bino-like neutralino by construction. In Model D, the lightest neutralino and lightest chargino are both winos-like and are therefore nearly degenerate. We adopt a short hand notation where we omit the explicit mention of the identity of the electroweak-ino in the decay, as it can always be inferred from the observable particle content.

We emphasize that our goal in this study is to demonstrate a method which allows us to extract information of the SUSY spectrum, such as the identity of the LSP with relatively low integrated luminosity. This is possible mainly because, unlike the precision measurements of the masses and couplings, our method mainly relies on inclusive counts and general kinematical features. Moreover, since we do not demand direct reconstruction, we are able to take advantage of many channels with multiple leptons. Due to lower background and theoretical uncertainty in comparison with the pure hadronic channel, we expect to have significant excesses in many of these channels. After discovery, we expect our method will yield a first set of clues about the underlying model during the early stages of LHC operation. This discussion is based on the results found in [13].

2.1 Benchmark Models

We consider four benchmark models in our study. The model spectra and relevant decay branching ratios are shown in Table 2.1. The gluino mass is fixed at 650 GeV for each case. For simplicity, in models A, B, and C we consider the scenario that the gluino decay sequence produces only top and bottom quarks in a single decay step. This occurs if the only state lighter than the gluino is the LSP, which in models A,B,

and C is taken to be a bino-like neutralino by setting $(|\mu|, M_2) > M_3 > M_1$. We fix the lightest neutralino mass at 100 GeV.

Model A represents the simplest example of multi-top physics under these assumptions. By construction, the first- and second-generation squark masses, as well as the $\tilde{t}_2$ and $\tilde{b}_2$ masses are all ~ 8 TeV. Only the $\tilde{b}_1$ and $\tilde{t}_1$ are light relative to the other squarks, with the $\tilde{t}_1$ the lightest at ~ 1.3 TeV. Consequently, gluino decays proceed through an off-shell $\tilde{t}_1^*$, resulting in dominant production of four top quarks in the final state.

In models B and C, the sbottom and stop masses are now sub-TeV and of similar order, but still more massive than the gluino. This increases the branching fraction for the decay channel $\tilde{g} \to b\bar{b}\tilde{\chi}_1^0$. Model B has a slightly lighter $\tilde{t}_1$ relative to either sbottom, and therefore exhibits a slightly larger decay fraction to two top quarks. In Model C the stop and bottom squark masses are adjusted in order to achieve a nearly even decay fraction to both top and bottom quarks.

We also consider the possibility of a wino-like neutralino LSP. Here we take $(|\mu|, M_1) > M_3 > M_2$, so that now the only states lighter than the gluino are the neutralino LSP and the light chargino $\tilde{\chi}_1^{\pm}$. In this case the lightest chargino is nearly degenerate with the LSP, and the chargino decay products are too soft to pass selection cuts. Thus, the chargino appears only as missing energy. This scenario is represented by model D.

In Table 2.1 and the rest of this chapter, we adopt a short-hand notation for gluino decay by only including top and bottom quarks and not giving explicitly the electroweak-inos, as it should be evident from the context.

2.2 Signal Isolation and Backgrounds

We begin by discussing the prospects for signal isolation above Standard Model background at the LHC. The relatively large b-jet and lepton multiplicity associated with four-top production provide for potentially striking signatures that are easily distinguishable above the expected SM background. We find that by requesting ≥ 3 b-tagged jets and at least one lepton, it is possible to achieve signal significance $S/\sqrt{B} > 3$ for only 500 pb^{-1} of integrated luminosity. We will demonstrate the discovery potential in three of the four benchmark models.

One of the important backgrounds from the Standard Model for final states with many b-tagged jets, several isolated leptons and very high missing E_T, is top pair production, $t\bar{t}$. The expected cross-section at the LHC for this background is $\sigma = 833$ pb (NLO+NLL result [48]). The $t\bar{t}$ background event samples were produced using Pythia 6.4 [49].

Process	σ [pb]	Process	σ [pb]	Process	σ [pb]
$t\bar{t} + 1, 2, 3$ jets	833	$t\bar{b}Z + 1, 2$ jets	0.67	$ZW^+b + 1, 2$ jets	0.48
$t\bar{t}Z + 1, 2$ jets	0.28	$\bar{t}bZ + 1, 2$ jets	0.58	$ZW^-b + 1, 2$ jets	0.50
$t\bar{t}W^- + 1, 2$ jets	1.5	$t\bar{b}W^+ + 1, 2$ jets	0.18	$ZW^+\bar{b} + 1, 2$ jets	0.85
$t\bar{t}W^+ + 1, 2$ jets	3.4	$\bar{t}bW^- + 1, 2$ jets	0.09	$ZW^-\bar{b} + 1, 2$ jets	0.28

Table 2.2: Standard Model backgrounds and relevant cross sections used.

We have also included in our analysis a set of SM backgrounds involving associated production of W/Z bosons with third generation quarks. These contribute significantly to signals with high lepton multiplicity, or same sign dileptons in the final state. As we will see, the latter case is a particularly important discovery channel early on. All background sources considered, and their respective cross sections are given in Table 2.2. The parton-level SM background event samples were produced with Madgraph v.4.2.3 [50], with the exception of the $t\bar{t}$ background which was pro-

duced using Pythia 6.4. The $t\bar{t}$ cross section was taken from [48], while the cross sections for the other backgrounds are calculated from Madgraph. The subsequent parton shower and hadronization were simulated with Pythia 6.4. We have used the CKKW matching scheme [51] implemented in Madgraph. Events are then passed to the publicly available detector simulation code PGS-4 [52]. For our study we set the PGS-4 performance parameters to mimic the behavior of the ATLAS detector. An overview of the PGS-4 design philosophy and capabilities has been presented at recent workshops [53]. While the program does not include all effects present in a real detector environment, it is sufficiently accurate for use in phenomenological studies. The current code is built upon earlier work designed to model the CDF and D0 detectors, and which has been shown to achieve good agreement with experimental results [54].

The signal event samples, for gluino pair production and decay, were produced using Pythia 6.4 and have been passed through the same PGS-4 detector simulation. Appropriate k-factors [55] were applied to the LO signal cross-section calculated by Pythia to obtain the NLO cross-section.

Basic muon isolation was applied to all samples: If the summed P_T in a $\Delta R = 0.4$ cone around the muon is greater than 5 GeV, or the ratio of the E_T in a 3×3 cell region of the calorimeter to the muon P_T is greater than 0.1125, the muon is merged with the nearest jet in ΔR.

We have also imposed on both the signal and the background the following selection cuts

1. $\not{E}_T \geq 100$ GeV

2. $p_T \geq 20$ GeV and pseudorapidity $|\eta| < 2.5$ for all objects

Standard Model Background					
	0b	*1b*	*2b*	*3b*	$\geq$*4b*
0L	1717.46	3069.29	2091.27	320.54	36.51
1L	783.34	1489.85	998.8	118.42	8.49
OS	41.89	61.82	34.06	4.46	0.01
SS	0.41	0.97	0.44	0.04	-
3L	0.1	0.54	0.24	0.06	-
$\geq$*4L*	-	-	-	-	-

Table 2.3: Number of Standard Model events with n ($n = 0..4$) b-tagged jets and m ($m = 0, 1, OS, SS, 3, 4$) leptons for the combined SM background considered. The following cuts were applied: MET $\geq$ 100 GeV, at least 4 jets with $p_T \geq 50$ GeV, all jet and lepton $p_T \geq 20$ GeV. The results are normalized to 500 pb^{-1}.

3. At least 4 jets with $p_T \geq 50$ GeV

Table 2.3 shows the expected number of events from the SM background. We have classified them according to the number of b-tagged jets and isolated leptons in the event. Same sign (SS) and opposite sign (OS) di-leptons are separated as they have very different origins and sizes. We will use the possible excess in these channels to assess the discovery potential. The results are normalized to 500 pb^{-1} of integrated luminosity. Crossed out entries indicate no background events passing the signature and selection cuts.

Model A				**Model C**				**Model D**			
	2b	*3b*	$\geq$*4b*		*2b*	*3b*	$\geq$*4b*		*2b*	*3b*	$\geq$*4b*
1L		166.2	70.9	*1L*		106.5	44.2	*1L*		98.	37.8
OS	27.6	19.3	7.3	*OS*	13.3	10.	3.9	*OS*	5.6	3.8	1.5
SS	12.7	9.4	3.1	*SS*	4.1	2.8	1.	*SS*	2.9	2.2	0.8
3L	3.1	2.2	0.8	*3L*	1.1	0.6	0.2	*3L*	0.2	0.1	0.1

Table 2.4: Number of signal events passing the selection cuts and containing n b-tagged jets and m leptons. The selection cuts applied were: MET $\geq$ 100 GeV, at least 4 jets with $p_T \geq 50$ GeV, all jet and lepton $p_T \geq 20$ GeV. The results are normalized to 500 pb^{-1}.

Table 2.4 shows the expected number of signal events with n b-tagged jets and m isolated leptons (leptons = $e^{\pm}, \mu^{\pm}$). Model A, which is predominantly a four top signal, has significantly more muti-lepton and b-jet events passing selection cuts than Model C and Model D, which have fewer four top events. Model C exhibits a stronger

	Model A				**Model C**				**Model D**		
	2b	*3b*	$\geq$*4b*		*2b*	*3b*	$\geq$*4b*		*2b*	*3b*	$\geq$*4b*
1L		15.3	24.3	*1L*		9.79	15.2	*1L*		9.00	13.0
OS	4.73	9.12	87.0	*OS*	2.28	4.73	47.0	*OS*	0.957	1.79	18.3
SS	19.2	49.4	-	*SS*	6.10	14.5	-	*SS*	4.31	11.3	-
3L	6.44	9.26	-	*3L*	2.35	2.63	-	*3L*	0.418	0.318	-

Table 2.5: Signal significance $S/\sqrt{B}$, computed for the results in Tables 2.4 and 2.3. The crossed out entries indicate no background events passing the signature and selection cuts.

signal than Model D, which has very few four top events.

In Table 2.5, we show the signal significance achievable with 500 pb^{-1} integrated luminosity. By requesting $\geq$ 3 b-tagged jets it is possible to observe signal significance $S/\sqrt{B}$ $\geq$3 for events with multiple leptons, an excess consistent with multi-top production. In the single lepton channels, a more detailed study of the background would be required to properly calculate the expected significance, since there are likely to be significant background contributions from QCD processes that can fake lepton production. The same-sign dilepton channel is probably the best channel for discovery, a finding that is consistent with results in [56]. It can also be observed that already with 100 pb^{-1} integrated luminosity a 4 top signal (Model A) may be established in the same sign dilepton, 3 b-jet channel.

During the early period of LHC data taking, missing energy may not be well understood since it requires a 'global' understanding of the ATLAS/CMS detectors. Therefore missing energy should not necessarily be taken as a reliable tool to discover new physics at low luminosities. If we do not include the missing energy cut in our analysis, then QCD backgrounds, particularly $b\bar{b}$ production, becomes a significant background to the multi-top signal. Requiring four hard jets, as we have done here, does reduce the QCD backgrounds since hard jets are less likely to produce isolated leptons [57]. However, even though the 2-lepton background from QCD might still be significant, it is unlikely that the 3-lepton QCD background will be more significant

	Model A				**Model C**				**Model D**		
	2b	*3b*	*≥4b*		*2b*	*3b*	*≥4b*		*2b*	*3b*	*≥4b*
1L		4.89	8.45	*1L*		3.22	5.27	*1L*		3.10	4.62
OS	1.08	3.32	7.55	*OS*	0.565	1.79	4.12	*OS*	0.249	0.742	1.56
SS	8.09	17.9	31.0	*SS*	2.57	5.87	9.99	*SS*	2.21	4.98	8.78
3L	3.16	7.37	-	*3L*	1.07	2.14	-	*3L*	0.270	0.318	-

Table 2.6: Signal significance $S/\sqrt{B}$, computed for the results in Tables 2.4 and 2.3 assuming no MET cut. Significance values ≥ 3 for are still achievable in the ≥ 3 b-jet + same-sign dilepton channel. The crossed out entries indicate no background events passing the signature and selection cuts.

than the 4-top signal [57, 58]. Thus, it seems reasonable that discovery could still be possible without missing energy at integrated luminosities greater than or equal to 500 pb^{-1}. Table 2.6 shows the signal significance for 500 pb^{-1} of data, computed assuming no missing energy cut. Significance values ≥ 3 are still clearly achievable in the ≥ 3 b-jet + same-sign dilepton channel.

2.3 Direct Reconstruction

Once evidence is obtained for an excess beyond the Standard Model in events with multiple b-jets and leptons, it is natural to assume that the signal involves production of multiple top quarks. In order to provide concrete evidence for this, W bosons and top quarks in the signal should be reconstructed.

In the model under consideration, where each signal event has four top quarks, the main sources of difficulty in reconstruction are low statistics, large combinatorial background, and poor object reconstruction due to the extremely complex event topology. Every $tttt$ event has four W bosons, each of which gives two jets if it decays hadronically. Furthermore, every top decay itself gives a b-jet. Therefore the expected number of hard jets arising in a decay with k W bosons decaying hadronically is $4 + 2k$. On top of this there are also jets arising from initial/final state radiation (ISR/FSR). For comparison, $t\bar{t}$ all hadronic decays are expected to

have 6 hard jets on average before ISR/FSR effects are included.

We expect that due to the large number of particles in the final state, the chance of reconstructible objects (such as jets) overlapping is large, so that the detector will frequently be unable to accurately reconstruct isolated objects. If two partons are very close in ΔR (roughly less than twice the diameter of the cone used in the jet algorithm), the jets coming from the partons are likely to be recombined into a single jet. Similarly, if a lepton is very close to a jet, it will likely not pass the isolation requirement. We utilize the standard cone jet reconstruction algorithm implemented in the PGS simulator, however we reduce the ΔR cone size to 0.4 in line with the expected performance of the ATLAS detector.

Figure 2.1 shows the distributions of the lowest, 2nd lowest, 3rd lowest, and 4th lowest ΔR values between reconstructible partons in four top events from benchmark model A. For comparison, the same information is also shown for Standard Model $t\bar{t}$ events. Here we define a reconstructible parton as any first/second generation quark or b-quark. It may be seen in figure 2.1 (a) that in four top events there is a large likelihood of three to four pairs of overlapping objects, rendering reliable final state reconstruction difficult.

Direct reconstruction of top quarks in somewhat different decay chains has been studied in Ref. [42, 43]. We expect a similar study in our case will also yield at least some evidence that there are indeed top quarks in the event. Rather then presenting a detailed analysis here, we focus on a somewhat different question. Clearly, in order to completely measure the branching ratios into different final states involving different numbers of top and bottom, it is not enough to just reconstruct a certain top quark. We need to be able to reconstruct *all* of the top quarks in the event with reasonable efficiency. However, our study already shows that there is a significant

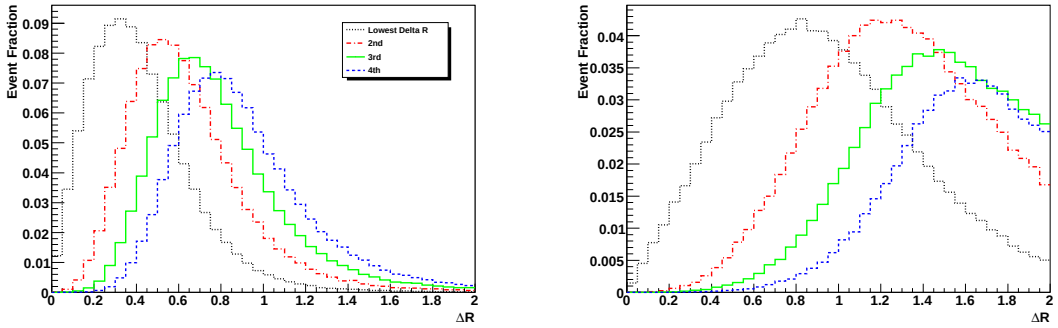

(a) (b)

Figure 2.1: Distributions of the lowest four values of separations, ΔR, between reconstructible partons (which here we take as any first/second generation quark or b-quark) obtained using the Pythia parton-level (truth) information for benchmark model A. For each event in the simulation, ΔR was computed for all pairs of reconstructible objects, ranked, and the lowest four values binned into histograms. The resulting distributions showing the lowest, 2nd, 3rd, and 4th lowest ΔR values encountered are given for (a) four-top events of model A, and also (b) hadronic $t\bar{t}$ decays. All distributions are normalized to unity. The partons present in four-top events are significantly closer to one another relative to those in SM $t\bar{t}$ events, increasing the liklihood of overlap, as well as a lower reconstruction efficiency.

overlap between different object in this type of signal events. Including additional combinatorics, we expect a very low efficiency for reconstructing multiple tops.

To gain some estimate of such efficiencies, we study how many tops we can possibly reconstruct in an event. To proceed, we define a 'top candidate' to be the combination of two light-jets (ie non-b-tagged) and one b-tagged jet, where the non-b-tagged dijet invariant mass satisfies $65 < m_{jj} < 95$ GeV, the invariant mass of the b-jet with any lepton must satisfy $m_{bl} > 155$ GeV, while the invariant mass with either of the two non-b-tagged jets must satisfy $m_{bj} < 160$ GeV. Finally, the invariant mass of the final three-jet combination must satisfy $125 < m_{jjb} < 225$ GeV.

Figure 2.2 shows two distributions for the number of top candidates observed in our benchmark model A. The first figure, 2.2 (a), includes all possible three-quark combinations that satisfy the requirements above. The inherent combinatorical background due to the intense hadronic activity in four-top events is clearly visible. We

see that the same b-quark can be combined with other partons to form several "top candidates". There can be no more than 4 top quarks present in the event, and the vast majority of 'candiate' combinations are incorretly chosen. Figure 2.2 (b) shows the same information except that here we isolate only the distinct jet combinations of each event. Degeneracies that arise are removed by keeping track of the mass difference $m_{jjb} - m_t$ for each jet triplet, and choosing the set of triplets with the lowest average difference. From the figure, it is clear that this approach gives a significantly more reasonable result. However, notice that the number of reconstructed candidates drops dramatically as the top multiplicity increases, rendering statistical analysis essentially impossible without a large integrated luminosity. For comparison, in figure 2.2 (c) we show the result obtained for a sample of Standard Model $t\bar{t}$ events. Compared to figure 2.2 (b), the $t\bar{t}$ sample yields no 3-top or 4-top event candidates, and exhibits an overall distribution that is distincly different from the result of model A. This suggests that a similar approach may potentially be used to obtain additional evidence for multi-top production, despite an inability to perform full statistical reconstruction due to insufficient luminosity. We do not examine the efficacy of such an approach here, and instead defer such a study to future work.

The study we perform here is not an actual reconstruction of the top quark. A true reconstruction involves positive identification of the top quark through statistical determination of the top invariant mass. Instead, this study is an estimate of how many objects obtained from recombining final states can be consistent with a top quark. We expect this study, though not completely precise, does capture the main effect of combinatorics and object merging. We observe that the efficiency for detecting one top quark as defined is approximately 48.5%, for two quarks $\sim 16.7\%$, three quarks $\sim 1.5\%$, and for four quarks $\sim 0.02\%$.

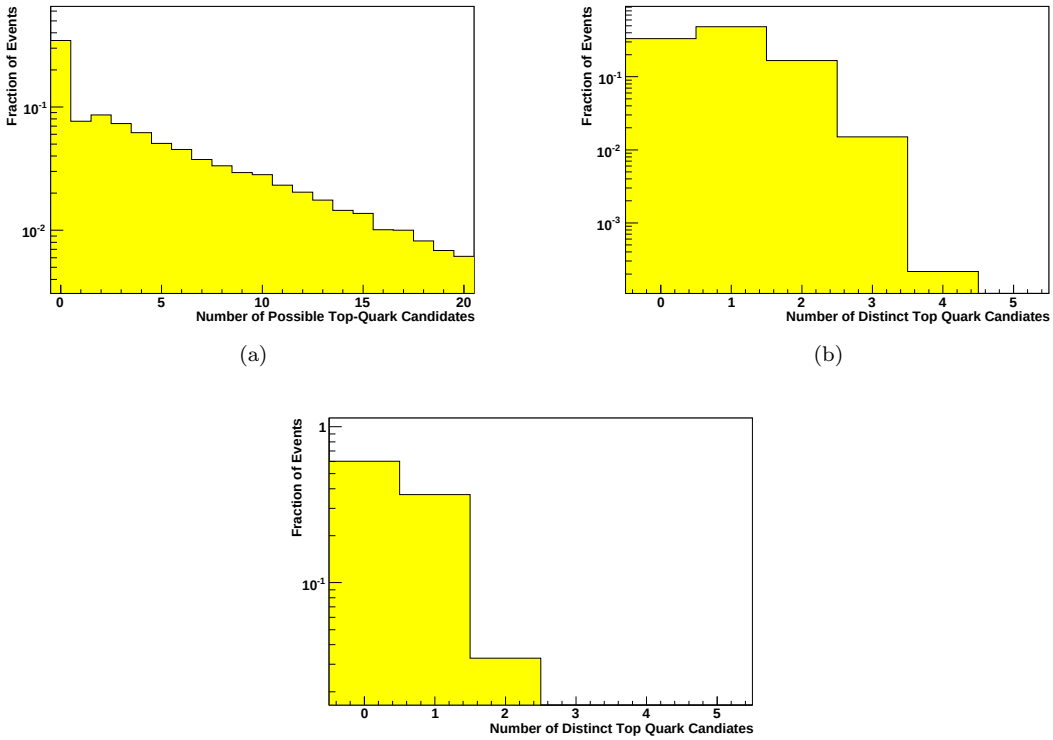

Figure 2.2: As a demonstration of the combinatoric background, in figure (a) we show the observed number of possible top 'candidates' obtained for our benchmark model A. We consider combinations with one b-jet and two light jets, where the invariant mass falls within the top mass window, and where the combination satisfies a minimal set of selection criteria (see text). Due to the combinatorics, the same b-quark can be combined with other partons to form multiple "top candidates". In (b) we show the resulting number of top candidates after attempts are made to remove combinatorics by isolating distinct 3-jet combinations. For this basic study we only require that events have at least 4 b-tagged jets. In (c) we show the result obtained for Standard Model $t\bar{t}$ events. Comparison with frame (b) reveals a distinct difference from events with multi-top production in excess of expected Standard Model processes. In particular no 3-top or 4-top events were observed for the $t\bar{t}$ sample.

Further perfections of reconstruction techniques are certainly going to improve these results and should be pursued. However, it is likely that to extract statistically significant information based on a full reconstruction will still require large integrated luminosity.

2.4 Understanding multi-top final states

As we have demonstrated in the previous sections, new physics signals containing multiple tops can be discovered at the LHC. By direct reconstruction, we expect to gather evidence that there are indeed top quarks in the signal. However, there are many possible event topologies which can contribute to our signal. In general, the gluino can decay into third generation quarks through $\tilde{g} \to t\bar{t} + \tilde{\chi}_i^0$, $\tilde{g} \to b\bar{b} + \tilde{\chi}_i^0$, and $\tilde{g} \to t\bar{b} + \tilde{\chi}_i^{\pm}$. Therefore, final states coming from gluino pair production can involve from zero to four top quarks, with relative amounts determined by gluino branching ratios. As we have argued in the introduction, measuring such branching ratios plays a central role in understanding the properties of superpartners involved. For example, the relative ratio of $\tilde{g} \to tt$ and $\tilde{g} \to bb$ could give us important information about the spectrum of the third generation squarks. At the same time, significant decay branching ratio of $\tilde{g} \to tb$ strongly suggests that either Higgsino or Wino (or both) is lighter than the gluino.

As demonstrated in the previous section, measuring the branching ratios by directly reconstructing top quarks suffers from low efficiencies. In this section, we will instead tackle this question from a different approach. We assume that the new physics signal has already been discovered in a set of channels, particularly those with multiple leptons and multiple bottom quarks (Table 2.4). In addition, we assume there are a set of statistically significant experimental observables defined on

the set of signal events. This general approach can in principle be applied in practice with an arbitrary set of experimental observables based on availability. Here, we will only use a limited set of experimental variables:

- 2 b-jets and either OS di-leptons, SS di-leptons, 3 leptons, 4 or more leptons
- 3 b-jets and either 1 lepton, OS di-leptons, SS di-leptons, 3 leptons, 4 or more leptons
- 4 or more b-jets and either 1 lepton, OS di-leptons, SS di-leptons, 3 leptons, 4 or more leptons

We will consider a general set of decay channels of the gluino which can in principle contribute to the new physics signal. We will consider as free parameters the relative branching ratios of those channels whose values are determined by a fit to the above set of experimental observables. This approach can be viewed as a natural application of the method proposed in Ref. [61]. The set of possible decay channels are chosen as follows

$$\begin{array}{llll} \tilde{g}\tilde{g} \to t\bar{t}\chi t\bar{t} & \tilde{g}\tilde{g} \to t\bar{t}\chi t\bar{b} + c.c & \tilde{g}\tilde{g} \to t\bar{t}\chi b\bar{b} & \\ \tilde{g}\tilde{g} \to t\bar{b}\chi b\bar{b} + c.c. & \tilde{g}\tilde{g} \to b\bar{b}\chi b\bar{b} & \tilde{g}\tilde{g} \to t\bar{b}\chi\bar{t}b + c.c. & \tilde{g}\tilde{g} \to t\bar{b}\chi t\bar{b} + c.c. \end{array} \tag{2.1}$$

where χ represents either the lightest neutralino $\tilde{\chi}_1^0$ in the case of benchmark models A,B, and C, or the lightest chargino $\tilde{\chi}_1^\pm$ in the case of benchmark model D. Recall that in this case the chargino and neutralino LSP are nearly degenerate, so that transitions between them will not yield observable decay products. The $+c.c.$ indicates the charge conjugated process.

The number of events in the possible $\tilde{g}\tilde{g}$ decay channels are given by

$$\begin{aligned} n_{t\bar{t}t\bar{t}} &= \sigma_{\tilde{g}\tilde{g}}\mathcal{L}Br(\tilde{g}\to t\bar{t})Br(\tilde{g}\to t\bar{t}) \\ n_{t\bar{t}t\bar{b}} &= \sigma_{\tilde{g}\tilde{g}}\mathcal{L}Br(\tilde{g}\to t\bar{t})Br(\tilde{g}\to t\bar{b}) \\ &\vdots \quad \vdots \quad \vdots \\ n_{qqqq} &= \sigma_{\tilde{g}\tilde{g}}\mathcal{L}Br(\tilde{g}\to qq)Br(\tilde{g}\to qq). \end{aligned} \tag{2.2}$$

These number can then be used to estimate the number of observed events with a particular signature, $N^{\rm sig}_{\rm obs}$, which can receive contributions from several channels listed above with a particular fraction, $\epsilon^{\rm sig}_{\rm channel}$, depending on event topology and experimental efficiencies. We have

$$\begin{aligned} N^{0b0l}_{\rm obs} &= n_{t\bar{t}t\bar{t}}\epsilon^{0b0l}_{t\bar{t}t\bar{t}} + n_{t\bar{t}t\bar{b}}\epsilon^{0b0l}_{t\bar{t}t\bar{b}} + \ldots + n_{qqqq}\epsilon^{0b0l}_{qqqq} \\ N^{1b0l}_{\rm obs} &= n_{t\bar{t}t\bar{t}}\epsilon^{1b0l}_{t\bar{t}t\bar{t}} + n_{t\bar{t}t\bar{b}}\epsilon^{1b0l}_{t\bar{t}t\bar{b}} + \ldots + n_{qqqq}\epsilon^{1b0l}_{qqqq} \\ &\vdots \quad \vdots \quad \vdots \\ N^{4b4l}_{\rm obs} &= n_{t\bar{t}t\bar{t}}\epsilon^{4b4l}_{t\bar{t}t\bar{t}} + n_{t\bar{t}t\bar{b}}\epsilon^{4b4l}_{t\bar{t}t\bar{b}} + \ldots + n_{qqqq}\epsilon^{4b4l}_{qqqq}. \end{aligned} \tag{2.3}$$

Our procedure is the following: First, we obtain estimates of all signal efficiencies $\epsilon^{\rm sig}_{\rm channel}$. Next, we perform a χ^2-fit to determine a set of best fit values of $\sqrt{\sigma_{\tilde{g}\tilde{g}}\mathcal{L}}\ Br_{\rm channel}$. Note that in order to obtain the branching ratio from these counting signatures, we will need to know the product $\sigma_{\tilde{g}\tilde{g}}\mathcal{L}$. Such information could be available independently from other measurements, such as the gluino mass. We will show later in this section that our method indeed gives us an estimate of this absolute rate. At this moment, we note that we can already derive a lot of information about the underlying model if we measure the ratio of branching ratios, for which the dependence on $\sigma_{\tilde{g}\tilde{g}}\mathcal{L}$ drops out.

The key step in this method of fitting to branching ratios is, of course, to obtain

an estimate for the efficiencies, $\epsilon^{\rm sig}_{\rm channel}$. Here we estimate the efficiencies through numerical simulation with Pythia/PGS, assuming a particular model, a template, of the underlying physics. Many factors enter in such an estimate. The existence of many objects, in particular jets, in the event means that there is a significant chance for leptons from top decays to be suffiently close to a jet that they fail to pass the the isolation cut. The assumed b-tagging performance can also affect the result. Numerical simulation using an appropriate detector simulator that approximates these effects is therefore unavoidable.

In practice, certain assumptions about the underlying model must be made in choosing a template. We have already chosen the set of channels to include, based on information gained from the type of study in the previous section. In addition, we have to choose the spectrum, the gluino mass and LSP mass, to be used in the template. To begin with, we will first choose a template model using the *actual* gluino mass and LSP mass as the underlying model. We will fit the underlying branching ratios by using efficiencies obtained by simulating this template and demonstrate such a fit does give us accurate information of the underlying model. We will then simulate a set of different templates with different mass hypotheses. We will show that for the variation of mass hypotheses we have studied, the difference induced for the fit does not significantly affect our conclusion about the underlying models. Of course, such a result still leaves the question of whether the range of variation of mass parameters we have used is too optimistic. Later in this section, we will show that indeed it is reasonable to expect we can get estimates of mass scales from other experimental observables so that we can choose our mass hypothesis with an error within this range. For the continuity of our presentation, we will present our result for the fits first. Then we will come back to address the question of choosing the

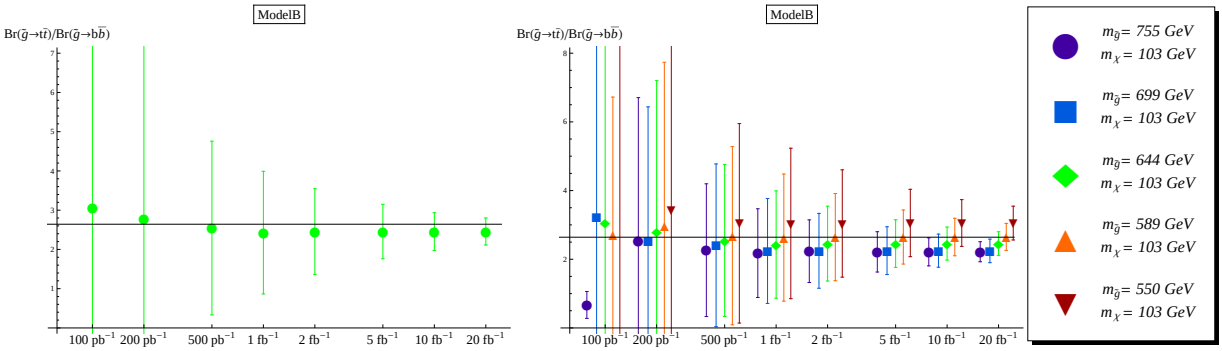

Figure 2.3: Results for fits of ratio $\mathrm{Br}(\tilde{g} \to t\bar{t})/\mathrm{Br}(\tilde{g} \to b\bar{b})$ for benchmark Model-B. The left panel shows the result with the correct mass hypothesis. In the right panel, the efficiencies are calculated for five different mass templates shown in the legend. The solid horizontal line gives the actual values of the branching ratios. Errors are 1σ and include errors for subtracting off the $t\bar{t}$ background.

mass hypothesis in detail.

Our fit to $\mathrm{Br}(\tilde{g} \to t\bar{t})/\mathrm{Br}(\tilde{g} \to b\bar{b})$ for benchmark model-B using the correct mass hypothesis is shown in the left panel of Fig. 2.3. For this and all the other fits presented in this section, we have required that for a channel to be included in our fits, there must be at least 1 signal event, and the significance over the $t\bar{t}$ background must be greater than 3.

We pause here to briefly describe how error bars are calculated in these and the other fits presented in this section. Using large statistics for the template model, the statistical errors for calculating the efficiencies and for determining the number of events for a given signature are assumed to be much smaller that the expected Gaussian errors from the LHC data. The only errors we include here are statistical errors from the minimization procedure. Therefore, the 1σ error for a given branching ratio is given by the change in the branching ratio required to shift the χ^2 one unit from its value at the minimum. For example, the 1σ error associated with $\mathrm{Br}(\tilde{g} \to tt)$

and $\mathrm{Br}(\tilde{g} \to bb)$ are given by

(2.4)

$$\delta_{Br(tt)} = \left(\frac{1}{2}\frac{\partial^2\chi^2}{\partial Br(tt)^2}\right)^{-1/2}\Bigg|_{\text{minimum}}, \quad \delta_{Br(bb)} = \left(\frac{1}{2}\frac{\partial^2\chi^2}{\partial Br(bb)^2}\right)^{-1/2}\Bigg|_{\text{minimum}}, \text{ etc.}$$

From the left Fig. 2.3, we see that using the correct mass hypothesis, we will be able to measure the ratio $\mathrm{Br}(\tilde{g} \to t\bar{t})/\mathrm{Br}(\tilde{g} \to b\bar{b})$ with good accuracy for an integrated luminosity of $\sim 5-10$ fb^{-1}. In particular, we will be able to verify that in Model B, the gluino decay is dominated by $\tilde{g} \to t\bar{t}$ with a smaller but non-vanishing branching ratio for $\tilde{g} \to b\bar{b}$.

Next, we want to assess the effect of changing our assumptions of underlying spectrum. We will assume that although the mass spectrum cannot be precisely measured, some crude estimates can still be made based on kinematical variables such as M_{eff}. We will provide justifications for this assumption later in this section. Therefore, we will consider cases where the gluino mass only deviates from the underlying benchmark model by about 100 GeV. In particular, we use four additional sets of alternative templates and carry out the same fit. The result in Model B is shown in the right panel of Fig. 2.3. We see that using different mass hypotheses does make a visible difference. However, we observe that these differences are not big enough to dramatically affect the information we will extract from our measurement of $\mathrm{Br}(\tilde{g} \to t\bar{t})/\mathrm{Br}(\tilde{g} \to b\bar{b})$. In the case of 3-body gluino decay under consideration, this ratio is proportional to $(m_{\tilde{b}}/m_{\tilde{t}})^4$. Therefore, we see that using different mass hypotheses within this range will at most result in a factor two error in the measurement of the ratio of the branching ratios, will induce at most $\sim 20\%$ shift in the inferred ratio $m_{\tilde{b}}/m_{\tilde{t}}$.

Notice that incorrect assumptions about the underlying spectrum do not lead to significant effects in the fit result when considering at least 1 fb^{-1} integrated

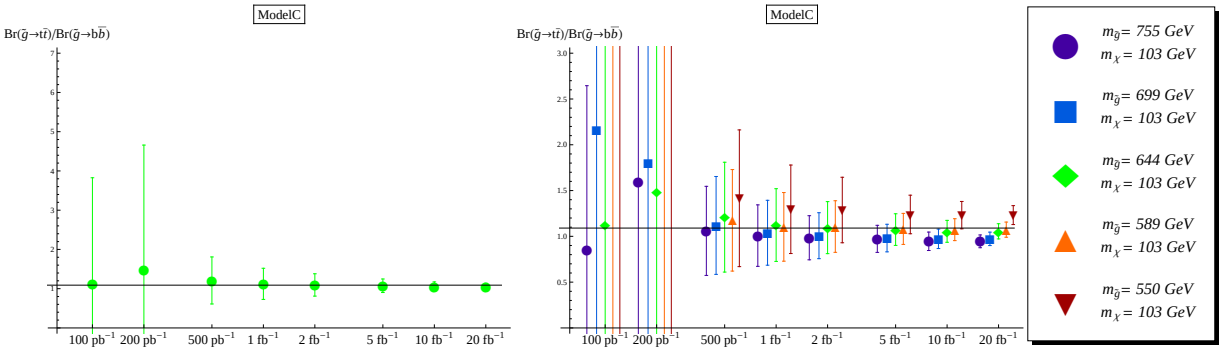

Figure 2.4: Results for fits of ratio $\mathrm{Br}(\tilde{g} \to t\bar{t})/\mathrm{Br}(\tilde{g} \to b\bar{b})$ for benchmark Model-C. The left panel shows the result with the correct mass hypothesis. In the right panel, the efficiencies are calculated for five different mass templates shown in the legend. The solid horizontal line gives the actual values of the branching ratios. Errors are 1σ and include errors for subtracting off the $t\bar{t}$ background.

luminosity of data. In all cases we can still extract a good estimate of the squark hierarchy, as well as the nature of the LSP.

Similar studies are performed for benchmark Model C. The result for Model C is shown in Fig. 2.4. Accuracies similiar to those obtained for Model B are observed here for the same integrated luminosity. In particular, we observe that we should be able to distinguish Model B and C from these results alone with about 5 fb^{-1} of integrated luminosity.

As a final note, we add that the ratio $Br(\tilde{g} \to t\bar{t})/Br(\tilde{g} \to b\bar{b})$ is slightly underestimated in all cases, even for the correct mass template. This is because the data actually contains a small percentage of events in which the gluino decayed to first and second generation quarks. As those decays looks most similar the decay into two b-jets, the fit tends to slightly overestimate $Br(\tilde{g} \to b\bar{b})$, and therefore underestimates $Br(\tilde{g} \to t\bar{t})/Br(\tilde{g} \to b\bar{b})$. In principle it should be possible to calibrate this procedure and thus eliminate such shifts in the final result. However, this is not necessary since such deviations do not mask the dominant behavior (that decays to top quarks dominate decays to bottom quarks, for example). It is expected that such

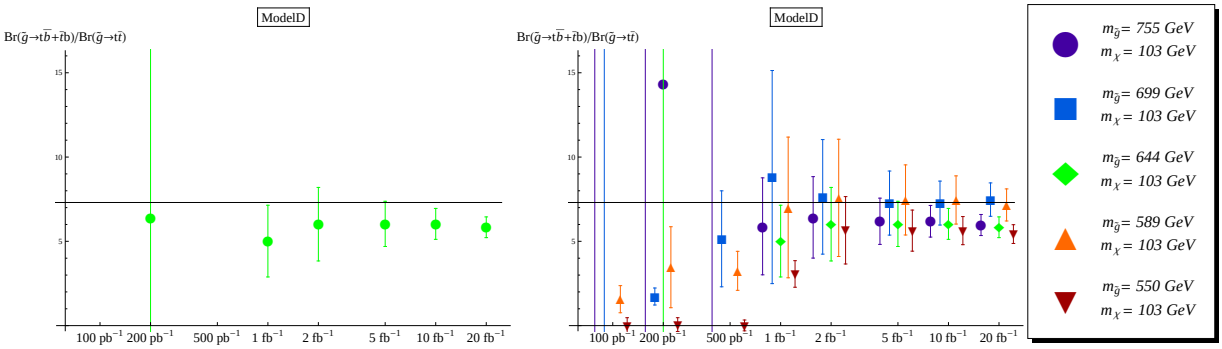

Figure 2.5: Results for fits of ratio $\mathrm{Br}(\tilde{g} \to t\bar{b} + \bar{t}b)/\mathrm{Br}(\tilde{g} \to t\bar{t})$ for benchmark Model-D. The left panel shows the result with correct mass hypothesis. In the right panel, the efficiencies are calculated for five different mass templates show in the legend. The solid horizontal line gives the actual values of the branching ratios. Errors are 1σ and include errors for subtracting off the $t\bar{t}$ background.

effects will become non-negligible for scenarios where the 1st- and 2nd-generation squarks are less massive, and perhaps very close to the gluino. A detailed study of this more complicated possibility is beyond the scope of this work.

The study of gluino decay for benchmark model D is presented in Fig. 2.5. In this case, we are interested in ratio $\mathrm{Br}(\tilde{g} \to t\bar{b} + \bar{t}b)/\mathrm{Br}(\tilde{g} \to t\bar{t})$. For a wino-LSP model like Model D, we expect this ratio to be large, which can indeed be experimentally verified with moderate luminosity, as shown in the figure.

We finally consider how well we can chose our mass hypotheses based on available experimental data. This is certainly an important issue since significantly inaccurate mass hypotheses lead to misleading results. To begin with, we study the dependence of our result on the mass hypothesis in more detail.

As the mass gap between the gluino and LSP is tightened, the events will have a harder time satisfying the missing energy cut we imposed. This more significantly affects events of the form $\tilde{g} \to tt + \not{E}_T$ than $\tilde{g} \to bb + \not{E}_T$, since the tops will use more of the gluinos' energy than the bottoms. Thus a tighter mass gap used in our template results in an underestimation the ratio of efficiencies $\epsilon_{t\bar{t}t\bar{t}}/\epsilon_{t\bar{t}b\bar{b}}$ (see Figure

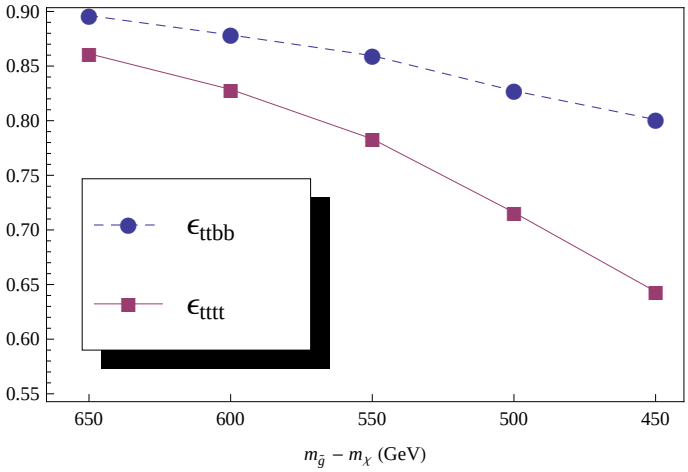

Figure 2.6: Dependence of efficiencies on the mass gap $M_{\tilde{g}} - M_{\rm LSP}$ to pass the missing energy cut, MET $\geq$ 100 GeV. This dependance is the dominant effect for the variation of fits on the mass hypothesis.

2.6). The fitter then adjusts for this low efficiency by fitting more *tttt* events relative to *ttbb* events to the signature counts

$$\frac{Br(\tilde{g}\tilde{g} \to t\bar{t}t\bar{t})}{Br(\tilde{g}\tilde{g} \to t\bar{t}b\bar{b})} \approx \frac{Br(\tilde{g} \to t\bar{t})^2}{2Br(\tilde{g} \to t\bar{t})Br(\tilde{g} \to b\bar{b})} \approx \frac{\epsilon_{t\bar{t}b\bar{b}}}{\epsilon_{t\bar{t}t\bar{t}}}. \tag{2.5}$$

Thus, in Models B and C as we increase(decrease) the gluino mass in our templates we tend to underestimate(overestimate) the branching ratio $Br(\tilde{g} \to t\bar{t})/Br(\tilde{g} \to b\bar{b})$.

We see that the change in the mass gap between gluino and the LSP can account for most of the variation in the fit result. For example, extrapolation from our study suggests that if our assumption of gluino mass is off by more than 200 GeV, the result for benchmark Model B will indeed look similar to that of Model C. However, since we expect to have significant excess in multiple channels, we observe that we should also have a significant amount of information about the mass scales, and in particular the mass gap $M_{\tilde{g}} - M_{\rm LSP}$ of the new physics particles already at early stages of LHC running. For example, we would expect simple transverse variables in channels with multiple leptons (and hence lower Standard Model background)

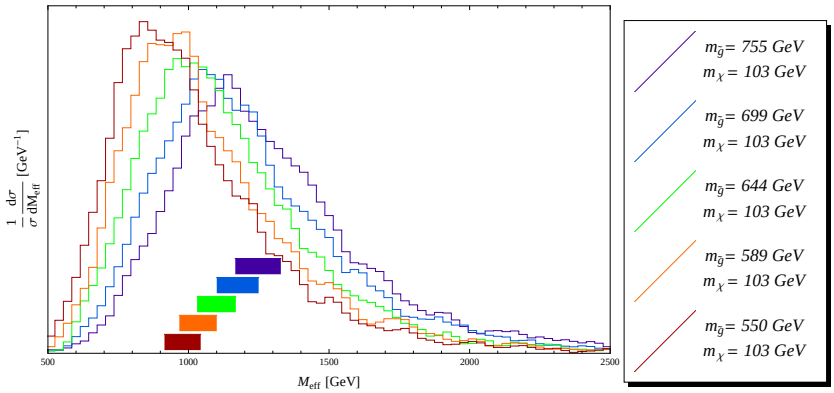

Figure 2.7: Effective mass distribution, of $\tilde{g}\tilde{g} \to \bar{t}t\bar{t}$ events for the 5 gluino masses used in fits. The bars at the bottom show the location of the inner 20% quantile; the highest one is for the largest gluino mass, the second highest for second largest gluino mass, etc. The histograms are normalized so that the total area is unity.

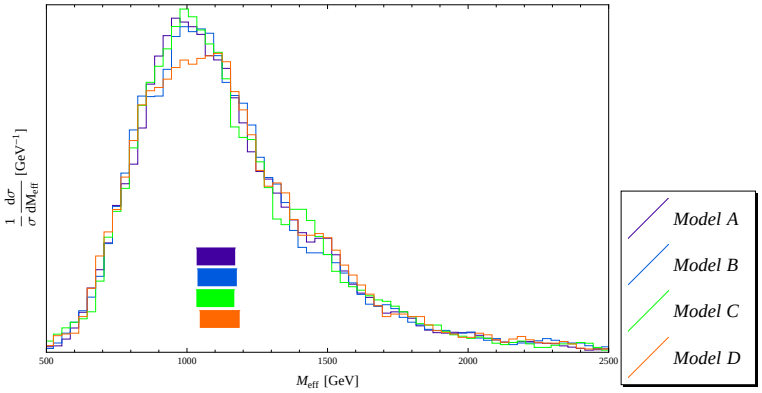

Figure 2.8: Effective mass distribution, of Models-(A,B,C,D). The bars at the bottom show the location of the inner 20% quantile. The histograms are normalized so that the total area is unity.

should already provide some indication of the mass scales involved.

Indeed, visible differences can be seen between different gluino masses when we histogram the effective mass, M_{eff}, defined as the scalar sum of the transverse momentum for all objects in the an event

$$M_{eff} = \sum_i p_{T,i} + \not{E}_T. \tag{2.6}$$

To demonstrate this, we plotted the effective mass for $\tilde{g}\tilde{g} \to t\bar{t}t\bar{t}$ for the 5 gluino masses used in fits above, in Figure 2.7. The histogram curves move to lower energies

(right to left) as the gluino mass is lowered. There is also a noticeable change in the effective mass spread, which we quantify as the location of middle 20% quantile. The bars at the bottom show the location of the inner 20% quantile; the highest one is for the largest gluino mass, the second highest for second largest gluino mass, etc. The fact that the bars move right to left as the gluino mass is lowered indicates that the median effective mass is decreasing, while the fact that the bars are shrinking indicate the effective mass has less variation as the gluino mass decreases.

This analysis was only carried out for $\tilde{g}\tilde{g} \to t\bar{t}t\bar{t}$, so we still need to demonstrate that the effective mass is also independent of the gluino decay. To do this we plotted the effective mass for the four models considered in this study, in Figure 2.8. The bars at the bottom show the spread, from top to bottom, for Model-A, Model-B, Model-C, and Model-D. As can be seen, the four histogram curves are remarkably similar, and have no noticeable differences in the median or spread.

Notice that since our fit yields a set of values for $\sqrt{\sigma_{\tilde{g}\tilde{g}}\mathcal{L}}\ Br_{\text{channel}}$ with any given mass hypothesis, it can by itself provide a consistency check on the hypothesis. In particular, we can get a lower limit on the gluino pair production cross section, by summing and squaring the fit values $\sqrt{\sigma_{\tilde{g}\tilde{g}}\mathcal{L}}\ Br_{\text{channel}}$

$$\sigma_{\tilde{g}\tilde{g}} \geq \mathcal{L}^{-1} \sum (\sqrt{\sigma_{\tilde{g}\tilde{g}}\mathcal{L}} Br_{tt} + \sqrt{\sigma_{\tilde{g}\tilde{g}}\mathcal{L}} Br_{bb} + \sqrt{\sigma_{\tilde{g}\tilde{g}}\mathcal{L}} Br_{tb})^2 \tag{2.7}$$

We can obtain cross sections for gluino pair production in the case of decoupled scalars, and rule out some incorrect gluino masses used in the templates. For example, in Model C (see Figure 2.9), we can rule out the $m_{\tilde{g}} = 755$ GeV mass template at 200 pb^{-1} of data at 1σ certainty, and begin to rule out the $m_{\tilde{g}} = 700$ GeV mass template at approximately 1 fb^{-1} of data at 1σ certainty. If the actual gluino is much lower than 600 GeV then there must be a significant branching fraction of the gluino

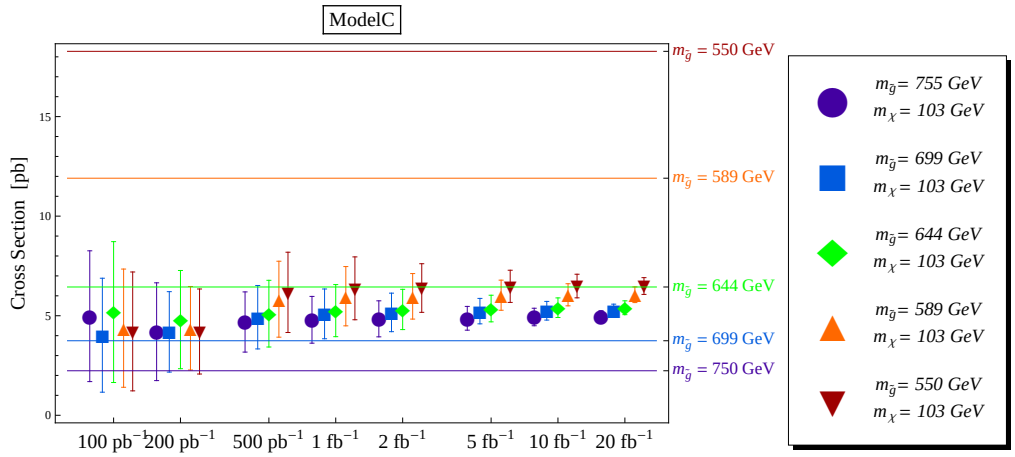

Figure 2.9: Gluino production cross section obtained by summing the individual branching ratios. We also show the theoretical cross sections at NNLO for gluino pair production for masses used in the templates. Notice that at high integrated luminosity we can begin to rule out heavier mass hypothesis

that is not contributing the channels we used in our fits, such as gluino decays into first and second generation quarks.

2.5 Summary

We have studied the LHC signals of pair produced light gluinos which decay dominantly through $\tilde{g} \to tt + \tilde{\chi}_1^0$, $\tilde{g} \to bb + \tilde{\chi}_1^0$, and $\tilde{g} \to tb + \tilde{\chi}_1^{\pm}$. We conclude that an early discovery of new physics in this scenario is possible due to significant excesses expected in multi-lepton multi-bottom channels. Measuring relative branching ratios of gluino decay into tt, bb and tb channels is essential to extract information about the underlying model. The crucial step in such a measurement is identify top multiplicity in the signal events. We show that direct reconstruction, while useful in gathering evidence for the existence top quark in decay products, is not sufficient to measure the number of top quarks in the event effectively. We proposed and studied a method based on fitting a set of branching ratios to a collection of experimental observables, most of them inclusive counts. Efficiencies for identifying a particular

final state resulting from certain underlying decay topology are estimated by simulating corresponding templates. We conclude that this method will allow us to learn about gluino decay branching ratios with roughly 10 fb^{-1} of integrated luminosity. We verified that, in combination with earlier information on the mass spectrum of gluino and the LSP, we can obtain a reliable measurement by choosing appropriate mass hypotheses. We emphasize that the main advantage of our method is that it allows us to use a large number of channels, many of them with multiple leptons and bottoms, in which we expect to see excesses during the early stage of LHC in models of this sort.

We showed that we can expect to gain enough information about the mass spectrum, in particular the mass gap $M_{\tilde{g}} - M_{\text{LSP}}$, from simple observables like effective mass and demonstrated that, with our fitting method, it is also possible to obtain an estimate of the gluino production cross section which in turn gives us very valuable information of the gluino mass, which also gives a consistency check of the assumption we made in our measurement of the branching ratio.

In this work we have considered only benchmark models with only a set of simple decay chains. More complicated models will certainly contain channels which requires further study [42, 43]. For example, a decay chain that contains $\tilde{t} \to b\tilde{\chi}_i^{\pm}$ followed by $\tilde{\chi}^{\pm} \to W\tilde{\chi}_i^0$ has the same set of final state particles as top decay. On the other hand, we have also only used counting signatures in our fit. Inclusion of more kinematical variables may improve our ability of discerning other decay topologies. For example, in the decay of stop mentioned above, the kinematics of b and W will be in general different from the case of top decay.

One key factor entering our lepton efficiency is the isolation requirement. This is particularly significant in our case since we expect to have a lot of hadronic activity

in these top rich events. We have only implemented a simple and commonly used isolation criterion based on hadronic activity within a narrow cone around the lepton. However, one can in principle improve and optimize the isolation cuts by including additional alternative isolation criteria, such as by requiring the invariant mass of lepton and the hadronic activity $m_{\ell,had} > m_{\rm cut}$, where $m_{\rm cut}$ is some chosen cut-off value. This cut is effective since a lepton from heavy flavor decay is typically soft and therefore gives a small $m_{\ell,had}$, while it is expected to be larger for accidental overlap between lepton and jet.

CHAPTER III

Studying Gaugino Mass Unification at the LHC

If supersymmetry is relevant at the electroweak scale there are many reasons to expect that its presence will be established early on in the LHC program [63]. Indeed, even some properties of the spectrum, such as the masses and spins of low-lying new states, may be crudely known even after relatively little integrated luminosity [64, 65, 66]. In Chapter II, we addressed several aspects of identifying scenarios such as SUSY at the LHC. In this chapter we begin to address the next question: How can we connect the multiple LHC observations to organizing principles in some (high-energy) effective Lagrangian of underlying physics?

This secondary problem can be further divided into two sub-problems. The first has come to be called the Inverse Problem, as discussed in Chapter I. Briefly stated, the Inverse Problem is the recognition that even in very restrictive model frameworks it is quite likely that more than one set of model parameters will give predictions for LHC observations that are in good agreement with the experimental data [12]. Much recent work has focused on how to address this issue [67, 68, 69, 70, 71], and we will borrow much of the philosophy and many of the useful techniques from this recent literature. But our focus here is on what we might call the second sub-problem: how to turn the ensemble of distinct LHC signatures into a determination of certain

broad properties of the underlying Lagrangian at low energies. Clearly the most direct attack on this second sub-problem is to perform a global fit to the parameters of a particular model [72, 73], modulo the degeneracy issue just described above. Not surprisingly, therefore, the work we will describe here will make significant use of likelihood fits. But our ultimate goal is to fit to certain broad properties of the *underlying physics itself* – and not simply to a particular model of that physics.

We will refine this rather vague-sounding goal in a moment. But it is helpful to first consider an example of what we mean by the phrase "broad properties of the underlying physics." Consider a high energy theorist interested in connecting the (supersymmetric) physics at the LHC to physics at an even higher energy scale, such as some underlying string theory. What sort of information would be of most use to him or her in this pursuit? Would it be a precise measurement of the gluino mass, or of the mass splitting in the top squark sector, or some other such measurement? Obtaining such information is (at least in principle) possible at the LHC, but far more valuable would be knowledge of the size of the supersymmetric μ-parameter or whether $\tan\beta$ is very small. Such information is far more difficult to obtain at the LHC [74] but is more correlated with moduli stabilization and/or how the μ-parameter is generated in string models [75]. For example, this knowledge may tell us whether the μ-parameter is fundamental in the superpotential or generated via the Kähler potential as in the Giudice-Masiero mechanism [76]. This, in turn, is far more powerful in discriminating between potential string constructions than the gluino mass itself – no matter how accurately it is determined. We might refer to the genesis of the μ-parameter as a "broad property of the underlying physics."

If all such key broad properties of the underlying physics were enumerated, it is our view that one of the most important such properties would be the question of

gaugino mass universality. That is, the notion that at the energy scale at which supersymmetry breaking is transmitted to the observable sector, the gauginos of the minimal supersymmetric Standard Model (MSSM) all acquired soft masses of the same magnitude. This issue is intimately related to another, perhaps equally important issue: the wave-function of the lightest supersymmetric particle, typically the lightest neutral gaugino. Few properties of the superpartner spectrum have more far-reaching implications for low-energy phenomenology, the nature of supersymmetry breaking, and the structure of the underlying physics Lagrangian [77]. If the theorist could be told only one "result" from the LHC data the answer to the simple question "Is there evidence for gaugino mass universality?" might well be it. But these soft parameters are not themselves directly measurable at the LHC [78].[1] One might consider performing a fit to some particular theory, such as minimal supergravity (mSUGRA), in which universal gaugino masses are assumed [81] – or perhaps to certain models with fixed, non-universal gaugino mass ratios [82, 83]. But we are not so much interested in whether mSUGRA – or any other particular theory for which gaugino mass universality is a feature – is a good fit to the data. Rather, we wish to know whether gaugino mass universality is a property of the underlying physics *independent of all other properties of the model.* From this example both the ambitiousness and the difficulty inherent in our task is clear.

We have therefore decided to begin our attack by considering a concrete parametrization of non-universalities in soft gaugino masses. Many such frameworks present themselves, but we will choose a parametrization that has the virtue of also having a strong theoretical motivation from string theory. In recent work by Choi and Nilles [84] soft supersymmetry-breaking gaugino mass patterns were explored in a

[1] Even a measurement of the physical gluino mass is not a direct measurement of the associated $SU(3)$ soft mass M_3. Quantum corrections to the gluino bare mass can be sizable and their theoretical computation involves a large set of other MSSM soft parameters [79, 80] – which are also not directly measurable!

variety of string-motivated contexts. In particular, the so-called "mirage pattern" of gaugino masses provides an interesting case study in gaugino mass non-universality. Yet as mentioned above, these soft supersymmetry breaking parameters are not themselves directly measurable. Linking the soft parameters to the underlying Lagrangian is important, but without the crucial step of linking the parameters to the data itself it will be impossible to reconstruct the underlying physics from the LHC observations.

The mirage paradigm gets its name from the fact that should the mirage pattern of gaugino masses be used as the low-energy boundary condition of the (one-loop) renormalization group equations then there will exist some high energy scale at which all three gaugino masses are identical. This unification has nothing to do with grand unification of gauge groups, however, and the gauge couplings will in general *not* unify at this particular energy scale – hence the name "mirage." The set of all such low-energy boundary conditions that satisfy the mirage condition defines a one-parameter family of models. This parameter can be taken to be the mirage unification scale itself, or some other parameter, such as the ratio between various contributions to the gaugino soft masses. We note that the minimal supergravity paradigm of soft supersymmetry breaking is itself a member of this family of models since it is *defined* by the property that gaugino masses are universal at the scale $M_{\rm GUT} \simeq 2 \times 10^{16}$ GeV. Indeed, in the parametrization we adopt from [84], the gaugino mass ratios at the electroweak scale take the form

$$M_1 \,:\, M_2 \,:\, M_3 \,\simeq\, (1 + 0.66\alpha) \,:\, (2 + 0.2\alpha) \,:\, (6 - 1.8\alpha)\,, \tag{3.1}$$

where the case $\alpha = 0$ is precisely the unified mSUGRA limit. Note that when we speak of testing gaugino mass universality, therefore, we do not imagine a common gaugino soft mass at the low-energy scale. Instead, the "universality" paradigm

implies the ratios

$$M_1 \,:\, M_2 \,:\, M_3 \simeq 1 \,:\, 2 \,:\, 6\,. \tag{3.2}$$

The goal of this work is to ask whether it is possible to determine that the α parameter of (3.1) is different from zero – and if so, how.

The theoretical details behind the ratios of (3.1) will be the topic of Section 3.1 in this chapter. These details are largely irrelevant for the analysis that follows in Sections 3.2 and 3.4, but may nevertheless be of interest to many readers. For those who are only interested in the methodology we will pursue and the results, this section can be omitted. At the end of Section 3.1 we will present two benchmark scenarios that arise from concrete realizations of the mirage pattern of gaugino masses in certain classes of string models. In Section 3.2 we discuss how we will go about attempting to measure the value of the parameter α in (3.1). In Section 3.3 we describe the process that led us to an ensemble of specific LHC observables targeted for precisely this purpose. In Section 3.4 this list of signatures is tested on a large collection of MSSM models, as well as on our two special benchmarks from Section 3.1. We will see that the signature lists constructed using the method of Section 3.2 do an excellent job of detecting the presence of non-universality in the gaugino soft masses over a very wide array of supersymmetric spectra hierarchies and mass ranges. Non-universality on the order of 30-50% should become apparent within the first 10 fb^{-1} of analyzed data for most supersymmetric models consistent with current experimental constraints. Detecting non-universality at the 10% level would require an increase in data by roughly a factor of two. Nevertheless, depending on the details of the superpartner spectrum, some cases will require far more data to truly measure the presence of non-universality. Of course all of these statements must here be understood in the context of the very particular assumptions of this

study. Some thoughts on how the process can be taken further in the direction of increased realism are discussed in the concluding section.

Before moving to the body of this work, however, we would like to take a moment to emphasize a few broad features of the theoretical motivation behind the parametrization in (3.1). In the limit of very large values for the parameter α the ratios among the gaugino masses approach those of the anomaly-mediated supersymmetry breaking (AMSB) paradigm [85, 86]. In fact, the mirage pattern is most naturally realized in scenarios in which a common contribution to all gaugino masses is balanced against an equally sizable contribution proportional to the beta-function coefficients of the three Standard Model gauge groups. Such an outcome arises in string-motivated contexts, such as KKLT-type moduli stabilization in D-brane models [87, 88] and Kähler stabilization in heterotic string models [89]. These string-derived manifestations can also be extended easily to include the presence of gauge mediation, in which the mirage pattern is maintained in the gaugino sector [90, 91]. Importantly, however, it can arise in *non*-stringy models, such as deflected anomaly mediation [92, 93]. We note that in none of these cases is the pure-AMSB limit likely to be obtained, so our focus here will be on small to moderate values of the parameter α in (3.1).[2] We will further refine these observations in Section 3.1 before turning our attention to the measurement of the parameter α at the LHC. This discussion is based on the results found in [14].

3.1 Theoretical Motivation and Background

In this section we wish to understand the origin of the mass ratios in (3.1) from first principles. We will treat the mirage mass pattern here in complete generality, without

[2] In any event, the phenomenology of the AMSB scenario is sufficiently distinct from the models we will consider that distinguishing between them should not be difficult [94].

any reference to its possible origin from string-theoretic considerations. This short section concludes with two specific sets of soft parameters, both of which represent models with the mirage gaugino mass pattern (though the physics behind the rest of their soft supersymmetry breaking parameters are quite different).

Let us begin by imagining a situation in which there are two contributions to the soft supersymmetry breaking gaugino masses. We assume that these contributions arise at some effective high-energy scale at which supersymmetry breaking is transmitted from some hidden sector to the observable sector. Let us refer to this scale as simply the ultraviolet scale $\Lambda_{\rm UV}$. It is traditional in phenomenological treatments to take this scale to be the GUT scale at which gauge couplings unify, but in string constructions one might choose a different (possibly higher scale) at which the supergravity approximation for the effective Lagrangian becomes valid. We will further assume that one contribution to gaugino masses is universal in nature while the other contribution is proportional to the beta-function coefficient of the Standard Model gauge group. More specifically, consider the universal piece to be given by

$$M_a^{univ}\left(\Lambda_{\rm UV}\right) = M_u\,, \tag{3.3}$$

where $a = 1, 2, 3$ labels the Standard Model gauge group factors $\mathcal{G}_a$ and M_u represents some mass scale in the theory. The second piece is the so-called anomaly mediated piece, which arises from loop diagrams involving the auxiliary scalar field of supergravity [95, 96]. It will take the form

$$M_a^{AMSB}\left(\Lambda_{\rm UV}\right) = g_a^2\left(\Lambda_{\rm UV}\right)\frac{b_a}{16\pi^2}M_g\,, \tag{3.4}$$

where the b_a are the beta-function coefficients for the Standard Model gauge groups. In our conventions these are given by

$$b_a = -(3C_a - \sum_i C_a^i), \tag{3.5}$$

where C_a, C_a^i are the quadratic Casimir operators for the gauge group $\mathcal{G}_a$, respectively, in the adjoint representation and in the representation of the matter fields Φ^i charged under that group.[3] For the Standard Model these are

$$\{b_1, b_2, b_3\} = \left\{\frac{33}{5}, 1, -3\right\} . \tag{3.6}$$

Note that if we take $\Lambda_{\rm UV} = \Lambda_{\rm GUT}$ then we have

$$g_1^2\left(\Lambda_{\rm UV}\right) = g_2^2\left(\Lambda_{\rm UV}\right) = g_3^2\left(\Lambda_{\rm UV}\right) = g_{\rm GUT}^2 \simeq \frac{1}{2} . \tag{3.7}$$

The mass scale M_g is common to all three gauge groups; the subscript is meant to indicate that the contribution in (3.4) is related to the gravitino mass. The full gaugino mass at the high energy boundary condition scale is therefore

$$M_a\left(\Lambda_{\rm UV}\right) = M_a^{univ}\left(\Lambda_{\rm UV}\right) + M_a^{AMSB}\left(\Lambda_{\rm UV}\right) = M_u + g_a^2\left(\Lambda_{\rm UV}\right)\frac{b_a}{16\pi^2}M_g . \tag{3.8}$$

Now imagine evolving the boundary conditions in (3.8) to some low-energy scale $\Lambda_{\rm EW}$ via the (one-loop) renormalization group equations (RGEs). For the anomaly-generated piece of (3.4) we need only replace the gauge coupling with the value at the appropriate scale

$$M_a^{AMSB}\left(\Lambda_{\rm EW}\right) = g_a^2\left(\Lambda_{\rm EW}\right)\frac{b_a}{16\pi^2}M_g , \tag{3.9}$$

while for the universal piece we can use the fact that M_a/g_a^2 is a constant for the one-loop RGEs. After some manipulation this yields

$$M_a^{univ}\left(\Lambda_{\rm EW}\right) = M_u\left[1 - g_a^2\left(\Lambda_{\rm EW}\right)\frac{b_a}{8\pi^2}\ln\left(\frac{\Lambda_{\rm UV}}{\Lambda_{\rm EW}}\right)\right] . \tag{3.10}$$

Combining (3.10) and (3.9) gives the low scale expression

$$M_a\left(\Lambda_{\rm EW}\right) = M_u\left\{1 - g_a^2\left(\Lambda_{\rm EW}\right)\frac{b_a}{8\pi^2}\ln\left(\frac{\Lambda_{\rm UV}}{\Lambda_{\rm EW}}\right)\left[1 - \frac{1}{2}\frac{M_g}{M_u\ln\left(\frac{\Lambda_{\rm UV}}{\Lambda_{\rm EW}}\right)}\right]\right\} . \tag{3.11}$$

[3] The convention chosen in (3.5) is opposite of the one chosen in [97].

For gaugino masses to be unified *at the low scale* $\Lambda_{\rm EW}$ then the quantity in the square brackets in (3.11) must be engineered to vanish. This can be achieved with a judicious choice of the values M_u and M_g for a particular high-energy input scale $\Lambda_{\rm UV}$. Put differently, for a given $\Lambda_{\rm UV}$ (such as the GUT scale) and a given overall scale M_u, there is a one-parameter family of models defined by the choice M_g.

It is possible, however, to find a more convenient parametrization of the family of gaugino mass patterns defined by (3.11). Consider defining the parameter α by

$$\alpha = \frac{M_g}{M_u \ln\left(\Lambda_{\rm UV}/\Lambda_{\rm EW}\right)}\,, \tag{3.12}$$

so that (3.11) becomes

$$M_a\left(\Lambda_{\rm EW}\right) = M_u\left[1 - \left(1 - \frac{\alpha}{2}\right) g_a^2\left(\Lambda_{\rm EW}\right) \frac{b_a}{8\pi^2} \ln\left(\frac{\Lambda_{\rm UV}}{\Lambda_{\rm EW}}\right)\right] \tag{3.13}$$

and the requirement of universality at the scale $\Lambda_{\rm EW}$ now implies $\alpha = 2$. Normalizing the three gaugino masses by $M_1\left(\Lambda_{\rm EW}\right)|_{\alpha=0}$ and evaluating the gauge couplings at a scale $\Lambda_{\rm EW} = 1000$ GeV we obtain the mirage ratios

$$M_1 \,:\, M_2 \,:\, M_3 \,=\, (1.0 + 0.66\alpha) \,:\, (1.93 + 0.19\alpha) \,:\, (5.87 - 1.76\alpha)\,, \tag{3.14}$$

for $\Lambda_{\rm UV} = \Lambda_{\rm GUT}$, in good agreement with the expression in (3.1).

Let us generalize the parametrization in (3.12) once more. Instead of defining the parameter in terms of the starting and stoping points in the RG evolution of the gaugino mass parameters, we will fix them in terms of mass scales in the theory itself. Thus we follow the convention of Choi et al. [98] and define

$$\alpha \equiv \frac{M_g}{M_u \ln\left(M_{\rm PL}/M_g\right)}\,, \tag{3.15}$$

where $M_{\rm PL}$ is the reduced Planck mass $M_{\rm PL} = 2.4 \times 10^{18}$ GeV. Our parametrization is now divorced from the boundary condition scales of the RG flow and can be

fixed in advance. The choice of mass parameters in the logarithm of (3.15) may seem arbitrary – and at this point it is indeed completely arbitrary – but they have been chosen so as to make better contact with string constructions. Inserting (3.15) into (3.11) yields

$$\begin{aligned} M_a\left(\Lambda_{\rm EW}\right) &= M_u\left\{1-g_a^2\left(\Lambda_{\rm EW}\right)\frac{b_a}{8\pi^2}\left[\ln\left(\frac{\Lambda_{\rm UV}}{\Lambda_{\rm EW}}\right)-\frac{\alpha}{2}\ln\left(\frac{M_{\rm PL}}{M_g}\right)\right]\right\} \\ &= M_u\left\{1-g_a^2\left(\Lambda_{\rm EW}\right)\frac{b_a}{8\pi^2}\left[\ln\left(\frac{\Lambda_{\rm UV}\left(M_g/M_{\rm PL}\right)^{\alpha/2}}{\Lambda_{\rm EW}}\right)\right]\right\}. \end{aligned} \tag{3.16}$$

Comparing this expression with (3.10) it is clear if gauge couplings unify at a scale $\Lambda_{\rm UV}=\Lambda_{\rm GUT}$, then we should expect the soft supersymmetry breaking gaugino masses to unify at an effective scale given by

$$\Lambda_{\rm mir}=\Lambda_{\rm GUT}\left(\frac{M_g}{M_{\rm PL}}\right)^{\alpha/2}. \tag{3.17}$$

We see that our parametrization in terms of α is indeed equivalent to a parametrization in terms of the effective unification scale, as suggested in the introduction.

The value of α as defined in (3.12) or (3.15) can be crudely thought of as the ratio of the anomaly contribution to the universal contribution to gaugino masses. Indeed, the limit $\alpha\to 0$ is the limit of the minimal supergravity paradigm, while $\alpha\to\infty$ is the AMSB limit. But as (3.8) makes clear, these two contributions will be of comparable size only if M_g is at least an order of magnitude larger than M_u. We could therefore have chosen a parametrization based on the ratio $r=M_g/M_u$, with interesting values being in the range $r\simeq\mathcal{O}(10-100)$. But such a parametrization spoils the simple relation with the mirage unification scale (3.17). Furthermore, the introduction of the factor $\ln(M_{\rm PL}/M_g)$ in (3.15) provides the needed large factor, taking a value of $\ln(M_{\rm PL}/M_g)\simeq 35$ for $M_g\simeq 1$ TeV. To obtain the mirage pattern it is therefore necessary for the underlying theory to generate some large number $c\simeq\ln(M_{\rm PL}/M_g)\simeq 30$.

Parameter	Point A	Point B		Parameter	Point A	Point B
α	0.3	1.0		$m^2_{Q_3}$	$(1507)^2$	$(430.9)^2$
M_g	1.5 TeV	16.3 TeV		$m^2_{U_3}$	$(1504)^2$	$(610.3)^2$
M_1	198.7	851.6		$m^2_{D_3}$	$(1505)^2$	$(352.2)^2$
M_2	172.1	553.3		$m_{\tilde{c}_R}$, $m^2_{L_3}$	$(1503)^2$	$(381.6)^2$
M_3	154.6	339.1		$m^2_{E_3}$	$(1502)^2$	$(407.9)^2$
A_t	193.0	1309		$m^2_{Q_{1,2}}$	$(1508)^2$	$(208.4)^2$
A_b	205.3	1084		$m^2_{U_{1,2}}$	$(1506)^2$	$(302.7)^2$
A_τ	188.4	1248		$m^2_{D_{1,2}}$	$(1505)^2$	$(347.0)^2$
$m^2_{H_u}$	$(1500)^2$	$(752.0)^2$		$m^2_{L_{1,2}}$	$(1503)^2$	$(379.8)^2$
$m^2_{H_d}$	$(1503)^2$	$(388.7)^2$		$m^2_{E_{1,2}}$	$(1502)^2$	$(404.5)^2$

Table 3.1: Soft Term Inputs. Initial values of supersymmetry breaking soft terms in GeV at the initial scale given by $\Lambda_{\rm UV} = 2 \times 10^{16}$ GeV. Both points are taken to have $\mu > 0$ and $\tan\beta = 10$. The actual value of $\tan\beta$ is fixed in the electroweak symmetry-breaking conditions.

In Table 3.1 we have collected the necessary soft supersymmetry-breaking parameters to completely specify two benchmark points for further analysis in what follows. Here we will simply indicate that point A represents a heterotic string model with Kähler stabilization of the dilaton which was studied in detail in [97]. This particular example has a value of $\alpha = 0.3$. Point B is an example from a class of Type IIB string compactifications with fluxes which was studied in [98]. This second example has a value $\alpha = 1.0$. Both are examples of the mirage pattern of gaugino masses, having mirage unification scales of $\Lambda_{\rm mir} = 2.0 \times 10^{14}$ GeV and $\Lambda_{\rm mir} = 1.5 \times 10^9$ GeV, respectively. Note that these soft supersymmetry breaking terms are taken to be specified at the GUT energy scale of $\Lambda_{\rm GUT} = 2.0 \times 10^{16}$ GeV and must be evolved to electroweak scale energies through the renormalization group equations.

3.2 Determining α: Methodology

3.2.1 Setting Up the Problem

As mentioned in the introduction, the ultimate goal of this avenue of study is to determine whether or not soft supersymmetry breaking gaugino masses obey some sort of universality condition independent of all other facts about the supersym-

metric model. In order to approach this goal we have begun by asking a simpler question: *assuming* the world is defined by the MSSM with gaugino masses obeying the relation (3.1), how well can we determine the value of the parameter α. At the very least we would like to be able to establish that $\alpha \neq 0$ with a relatively small amount of integrated luminosity. The first step in such an incremental approach is to demonstrate that some set of "targeted observables" [72] (we will call them "signatures" in what follows) is sensitive to small changes in the value of the parameter α in a world where all other parameters which define the SUSY model are kept fixed. In subsequent work we intend to relax this strong constraint and treat the issue of gaugino mass universality more generally. Despite the lack of realism we feel this is a logical point of departure – very much in the spirit of the "slopes" of the Snowmass Points and Slopes [99] and other such benchmark studies. Thus, where the Snowmass benchmarks talk of slopes, we will here speak of "model lines" in which all parameters are kept fixed but the value of α is varied in a controlled manner.

To construct a model line we must specify the supersymmetric model in all aspects other than the gaugino sector. The MSSM is completely specified by 105 distinct parameters, but only a small subset are in any way relevant for the determination of LHC collider observables [74]. We will therefore choose a simplified set of 17 parameters as in the two benchmark models of Table 3.1

$$\left\{ \begin{array}{c} \tan\beta,\ m_{H_u}^2,\ m_{H_d}^2 \\ M_3,\ A_t,\ A_b,\ A_\tau \\ m_{Q_{1,2}},\, m_{U_{1,2}},\, m_{D_{1,2}},\, m_{L_{1,2}},\, m_{E_{1,2}} \\ m_{Q_3},\, m_{U_3},\, m_{D_3},\, m_{L_3},\, m_{E_3} \end{array} \right\} . \tag{3.18}$$

The parameters in (3.18) are understood to be taken at the electroweak scale (specifically $\Lambda_{\rm EW} = 1000$ GeV) so no renormalization group evolution is required. The gluino

soft mass M_3 will set the overall scale for the gaugino mass sector. The other two gaugino masses M_1 and M_2 are then determined relative to M_3 via (3.14). A model line will take the inputs of (3.18) and then construct a family of theories by varying the parameter α from $\alpha = 0$ (the mSUGRA limit) to some non-zero value in even increments.

For each point along the model line we pass the model parameters to `PYTHIA 6.4` [49] for spectrum calculation and event generation. Events are then sent to the `PGS4` [100] package to simulate the detector response. Additional details of the analysis will be presented in later sections. The end result of our procedure is a set of observable quantities that have been designed and (at least crudely) optimized so as to be effective at separating $\alpha = 0$ from other points along the model line in the least amount of integrated luminosity possible. In Section 3.2.2 we describe the manner in which we perform this separation between models. The signature lists, and the analysis behind their construction, is presented in Section 3.3. In Section 3.4 we will demonstrate the effectiveness of these signature lists on a large sample of randomly generated model lines and provide some deeper insight on why the whole procedure works by examining our benchmarks in greater detail.

3.2.2 Distinguishability

The technique we will employ to distinguish between candidate theories using LHC observables was suggested in [72] and subsequently refined in [12]. The basic premise is to construct a variable similar to a traditional chi-square statistic

$$(\Delta S_{AB})^2 = \frac{1}{n} \sum_i \left[\frac{S_i^A - S_i^B}{\delta S_i^{AB}} \right]^2 , \tag{3.19}$$

where S is some observable quantity (or signature). The index $i = 1, \ldots, n$ labels these signatures, with n being the total number of signatures considered. The la-

bels A and B indicate two distinct theories which give rise to the signature sets S_i^A and S_i^B, respectively. Finally, the error term δS_i^{AB} is an appropriately-constructed measure of the uncertainty of the term in the numerator, i.e. the difference between the signatures. In this work we will always define a signature S as an observation interpreted as a count (or number) and denote it with capital N. One example is the number of same-sign, same-flavor lepton pairs in a certain amount of integrated luminosity. Another example is taking the invariant mass of all such pairs and forming a histogram of the results, then integrating from some minimum value to some maximum value to obtain a number. In principle there can be an infinite number of signatures defined in this manner. In practice experimentalists will consider a finite number and many such signatures are redundant.

We can identify any signature N_i with an effective cross section $\bar{\sigma}_i$ via the relation

$$\bar{\sigma}_i = N_i/L\,, \tag{3.20}$$

where L is the integrated luminosity. We refer to this as an *effective* cross-section as it is defined by the counting signature N_i which contains in its definition such things as the geometric cuts that are performed on the data, the detector efficiencies, and so forth. Furthermore these effective cross sections, whether inferred from actual data or simulated data, are subject to statistical fluctuations. As we increase the integrated luminosity we expect that this effective cross section $\bar{\sigma}_i$ (as inferred from the data) converges to an "exact" cross section σ_i given by

$$\sigma_i = \lim_{L\to\infty} \bar{\sigma}_i\,. \tag{3.21}$$

These exact cross sections are (at least in principle) calculable predictions of a particular theory, making them the more natural quantities to use when trying to distinguish between theories. The transformation in (3.20) allows for a comparison

of two signatures with differing amounts of integrated luminosity. This will prove useful in cases where the experimental data is presented after a limited amount of integrated luminosity L_A, but the simulation being compared to the data involves a much higher integrated luminosity L_B. Using these notions we can re-express our chi-square variable $(\Delta S_{AB})^2$ in terms of the cross sections

$$(\Delta S_{AB})^2 = \frac{1}{n} \sum_i \left[\frac{\bar{\sigma}_i^A - \bar{\sigma}_i^B}{\delta \bar{\sigma}_i^{AB}} \right]^2 . \tag{3.22}$$

We will assume that the errors associated with the signatures N_i are purely statistical in nature and that the integrated luminosities L_A and L_B are precisely known, so that

$$\delta \bar{\sigma}_i^{AB} = \sqrt{(\delta \bar{\sigma}_i^A)^2 + (\delta \bar{\sigma}_i^B)^2} = \sqrt{\bar{\sigma}_i^A / L_A + \bar{\sigma}_i^B / L_B} \,, \tag{3.23}$$

and therefore $(\Delta S_{AB})^2$ is given by

$$(\Delta S_{AB})^2 = \frac{1}{n} \sum_i \left[\frac{\bar{\sigma}_i^A - \bar{\sigma}_i^B}{\sqrt{\bar{\sigma}_i^A / L_A + \bar{\sigma}_i^B / L_B}} \right]^2 , \tag{3.24}$$

where each cross section includes the (common) Standard Model background, i.e. $\bar{\sigma}_i = \bar{\sigma}_i^{\rm SUSY} + \bar{\sigma}^{\rm SM}$.

The variable $(\Delta S_{AB})^2$ forms a measure of the distance between any two theories in the space of signatures defined by the S_i. We can use this metric on signature space to answer the following question: how far apart should two sets of signatures S_i^A and S_i^B be before we conclude that theories A and B are truly distinct? The original criterion used in [12] was as follows. Imagine taking any supersymmetric theory and performing a collider simulation. Now choose a new random number seed and repeat the simulation. Due to random fluctuations we expect that even the same set of input parameters, after simulation and event reconstruction, will produce a slightly different set of signatures. That is, we expect $(\Delta S_{AA})^2 \neq 0$ since

it involves the *effective* cross-sections as extracted from the simulated data. Now repeat the simulation a large number of times, each with a different random number seed. Use (3.24) to compute the distance of each new simulation with the original simulation in signature space. The set of all $(\Delta S_{AA})^2$ values so constructed will form a distribution. Find the value of $(\Delta S_{AA})^2\big|_{95}$ in this distribution which represents the 95th percentile of the distribution. This might be taken as a measure of the uncertainty in "distance" measurements associated with statistical fluctuations.

This procedure for defining distinguishability is unwieldy in a number of respects. Determining the threshold for separating models by $(\Delta S_{AB})^2 > (\Delta S_{AA})^2\big|_{95}$ is computationally intensive as it requires many repeated simulations of the same model (as well as the Standard Model background). More importantly, the "brute force" determination of $(\Delta S_{AA})^2\big|_{95}$ is particular to model A as well as the list of signatures used in (3.24). Each change in either the model parameters or the signature mix demands a new determination of the threshold for distinguishability. We will therefore propose a new criterion that has the benefit of being analytically calculable with a form that is universal to any pair of models and any set of signatures.

To do that let us reconsider the quantum fluctuations. At a finite integrated luminosity L we can describe the outcome of a counting experiment as a Poisson distribution approximated by a normal distribution (this is a good approximation for approximately 10 counts or more), which can be expressed as

$$N_i = L\sigma_i + \sqrt{L\sigma_i}\, Z\,. \tag{3.25}$$

Here Z is a standard random variable, *i.e.* a random variable having a normal distribution centered at 0 with a standard deviation of 1. Note that by introducing statistical fluctuations via the variable Z we can replace $\bar{\sigma}_i$ in (3.25) with the exact cross section. Equation (3.25) then merely states the well known fact that the dis-

tribution in measured values N_i should form a normal distribution about the value $L\sigma_i$. To combine two such distributions N_1 and N_2 we may write

$$\begin{aligned} N_{\rm tot} &= \left(L\sigma_1 + \sqrt{L\sigma_1}Z_1\right) + \left(L\sigma_2 + \sqrt{L\sigma_2}Z_2\right) \\ &\equiv L\sigma^T + \sqrt{L\sigma^T}Z, \end{aligned} \tag{3.26}$$

where Z is a new standard random variable and $\sigma^T = \sigma_1 + \sigma_2$ is the total cross-section. This relation follows from the property that for two normally distributed random variables x and y, with means μ_x and μ_y and standard deviations σ_x and σ_y, respectively, the combination $x + y$ is also a normally distributed random variable with new mean $\mu = \mu_x + \mu_y$ and standard deviation $\sigma = \sqrt{\sigma_x^2 + \sigma_y^2}$. In practice, σ_1 might be the contribution to a particular final state arising from Standard Model processes while σ_2 might be the contribution arising from production of supersymmetric particles.

With the above in mind we can re-visit the definition (3.24) and obtain an analytic approximation for the distribution in $(\Delta S_{AB})^2$ values by using random variables to represent the signatures. The measured cross sections can be related to the exact cross sections via

$$\bar{\sigma}_i^A = N_i^A/L_A = \sigma_i^A + \sqrt{\sigma_i^A/L_A}\, Z_A\,, \tag{3.27}$$

with a similar expression for the model B. Substituting (3.27) into (3.24) gives

$$\begin{aligned} (\Delta S_{AB})^2 &= \frac{1}{n}\sum_i \frac{\left[\sigma_i^A - \sigma_i^B + \sqrt{\frac{\sigma_i^A}{L_A} + \frac{\sigma_i^B}{L_B}}Z\right]^2}{\frac{\sigma_i^A}{L_A} + \frac{\sigma_i^B}{L_B} + \sqrt{\frac{1}{L_A^2}\frac{\sigma_i^A}{L^A} + \frac{1}{L_B^2}\frac{\sigma_i^B}{L^B}}Z'} \\ &\approx \frac{1}{n}\sum_i \left[\frac{\sigma_i^A - \sigma_i^B}{\sqrt{\frac{\sigma_i^A}{L_A} + \frac{\sigma_i^B}{L_B}}} + Z\right]^2, \end{aligned} \tag{3.28}$$

where we have combined Z_A and Z_B into the random variables Z and Z' and have assumed that L_A and L_B are sufficiently large to be able to neglect the term pro-

portional to Z'. In this limit we immediately see that $(\Delta S_{AB})^2$ is itself a random variable with a probability distribution for the quantity $(\Delta S_{AB})^2$ given by

$$P(\Delta S^2) = n\,\chi^2_{n,\lambda}(n\Delta S^2)\,, \tag{3.29}$$

where $\chi^2_{n,\lambda}$ is the non-central chi-squared distribution for n degrees of freedom[4], and λ is the so-called non-centrality parameter, which is given by

$$\lambda = \sum_i \frac{(\sigma_i^A - \sigma_i^B)^2}{\sigma_i^A/L_A + \sigma_i^B/L_B}\,, \tag{3.30}$$

Here the σ_i represent *exact* cross sections. Parameter λ represents the degree to which the distribution of outcomes for ΔS_{AB} for two differing models A and B is distinct from the distribution of outcomes for the null hypothesis ΔS_{AA}. We will address the significance of λ shortly. This result is actually what we expect since the original $(\Delta S_{AB})^2$ in (3.24) is essentially a chi-square like function. Note that since the σ_i in the distribution of (3.28) are exact, we have the anticipated result that fluctuations of the quantity $(\Delta S_{AA})^2$ should be given by the central chi-square distribution $\chi^2_n(0)$. We note, however, that the derivation of (3.28) implicitly assumed that the signatures S_i which we consider are uncorrelated – or more precisely that the *fluctuations* in these signatures are uncorrelated. We will have more to say about signature correlations in Section 3.3 below. We now have a measure of separation in signature space that is related to well known functions in probability theory.[5]

Armed with this technology, let us return to the issue of distinguishing a model from itself. From (3.28), (3.29) and (3.30) it is apparent that all the physics behind the distribution of possible $(\Delta S_{AB})^2$ values is contained in the values of λ and n. In particular the distribution of possible $(\Delta S_{AA})^2$ values (a central chi-square distri-

[4] If we had chosen to define the separation variable (3.19) without the factor of $1/n$ we would have found that the distribution of $(\Delta S_{AB})^2$ values was exactly given by the non-central chi-square distribution. The two are related by a simple change of variables.

[5] In fact, the non-central chi-square distribution is related to the regularized confluent geometric functions .

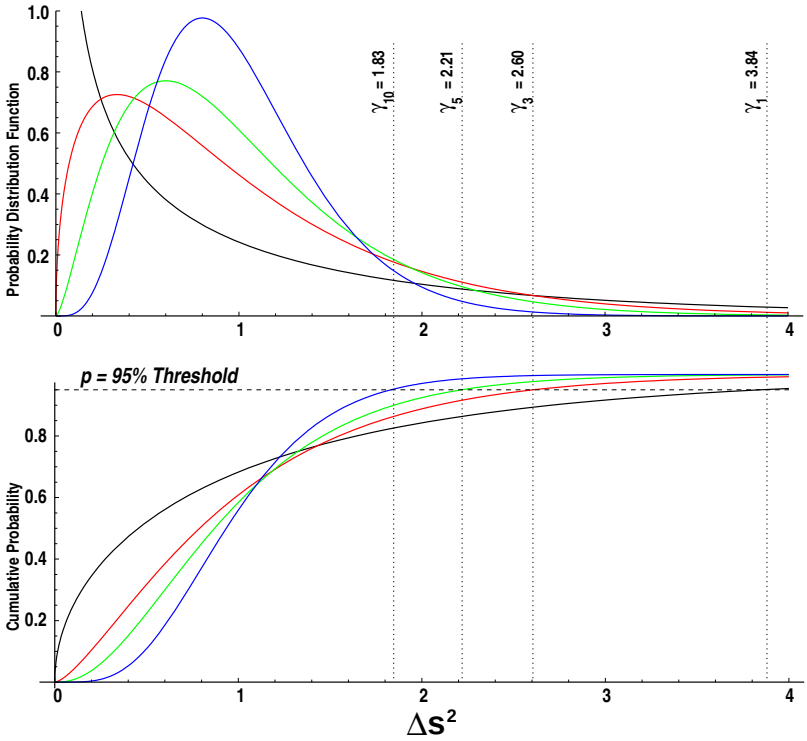

Figure 3.1: Plot of distribution in $(\Delta S_{AA})^2$ values. The top panel plots the probability distribution function (3.29) for $\lambda = 0$ and $n = 1$, 3, 5 and 10. The lower panel plots the cumulative distribution function – the absolute probability for obtaining that value of $(\Delta S)^2$. The 95% percent threshold is indicated by the horizontal lines, and the corresponding values of $(\Delta S)^2\big|_{95\text{th}}$ are indicated by the marked values of $\gamma_n(0.95)$.

bution) should depend *only* on the number n of signatures considered – not on the model point nor on the nature of those signatures. When comparing a model with itself we can therefore dispense with the subscript and write $(\Delta S_{AA})^2 = (\Delta S)^2$. We plot the probability distribution $P(\Delta S)^2$ of (3.29) for $\lambda = 0$ and various values of n in the top panel of Figure 3.1. We have also plotted the cumulative distribution function for the same n values in the lower panel of Figure 3.1. To rule out the null hypothesis (*i.e.* the hypothesis that models A and B are in fact the same model) to a level of confidence p requires demanding that $(\Delta S)^2$ is larger than the p-th percentile value for the distribution (3.29) for the appropriate n value. For example, if we use the criterion from [12] and require $(\Delta S_{AB})^2 > (\Delta S)^2\big|_{95\text{th}}$ then $p = 0.95$. We have

	Confidence Level p			
n	0.95	0.975	0.99	0.999
1	3.84	5.02	6.64	10.83
2	3.00	3.69	4.61	6.91
3	2.61	3.12	3.78	5.42
4	2.37	2.79	3.32	4.62
5	2.21	2.57	3.02	4.10
6	2.10	2.41	2.80	3.74
7	2.01	2.29	2.64	3.48
8	1.94	2.19	2.51	3.27
9	1.88	2.11	2.41	3.10
10	1.83	2.05	2.32	2.96

Table 3.2: List of $\gamma_n(p)$ values for various values of the parameters n and p. The value $\gamma_n(p)$ represents the position of the p-th percentile in the distribution of $P(\Delta S)^2$ for any list of n signatures. For example, if we consider a list of 10 signatures, then the quantity $(\Delta S_{AB})^2$ formed by these ten measurements must be larger than 1.83 to say that models A and B are distinct, with 95% confidence. If we demand 99% confidence this threshold becomes 2.32.

indicated this value for the cumulative distribution function by the horizontal dashed line in Figure 3.1. In general we will denote this particular value of $(\Delta S)^2\big|_p$ for each value of n by the symbol $\gamma_n(p)$. It can be found via the cumulative distribution function as in Figure 3.1, or by numerically solving the equation

$$\Gamma\left(\frac{n}{2},\, \frac{n}{2}\,\gamma_n(p)\right) = \Gamma\left(\frac{n}{2}\right)(1-p)\,, \tag{3.31}$$

where $\Gamma(n)$ is Euler's gamma function and $\Gamma(n,m)$ is the incomplete gamma function. A summary of these values for smaller n values is given in Table 3.2. If we measure our n signatures, extract the cross-sections, form $(\Delta S_{AB})^2$ and the number is greater than $\gamma_n(p)$ then we can say that the null hypothesis can be ruled out at a level of confidence given by $p\times 100\%$. The value of this critical $(\Delta S)^2\big|_p = \gamma_n(p)$ is a universal number determined *only* by our choice of p value and the number of signatures n that we choose to consider.

If, however, our measurement gives $(\Delta S_{AB})^2 < \gamma_n(p)$ then we cannot say the two models are distinct, at least not at the confidence level p. But they may still be separate models and we were simply unfortunate, with statistical fluctuations

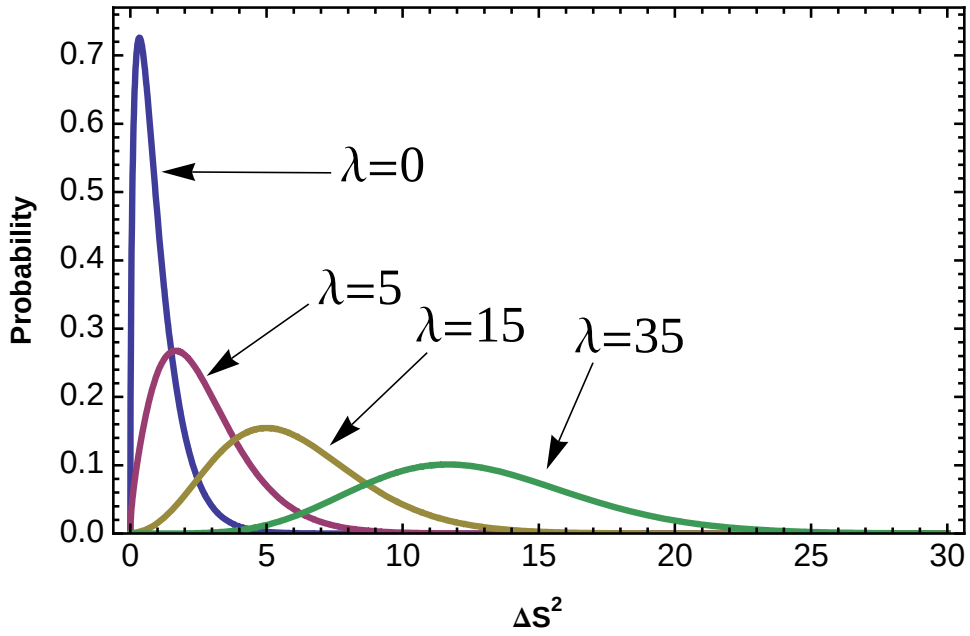

Figure 3.2: Plot of distribution in $(\Delta S_{AB})^2$ values for $n = 3$ and various λ. The probability distribution function (3.29) for $\lambda = 0$, 5, 15 and 35 is plotted for the case of $n = 3$. The curves are normalized such that the total area under each distribution remains unity. Note that the peak in the distribution moves to larger values of $(\Delta S_{AB})^2$ as the non-centrality parameter λ is increased.

producing a small value of $(\Delta S_{AB})^2$. If we accumulate more data and measure $(\Delta S_{AB})^2$ again, we may find a different result. To quantify the probability that two different models A and B will give a particular value of $(\Delta S_{AB})^2$ requires the use of the non-central chi-square distribution in (3.29). The degree of non-centrality is given by the quantity λ in (3.30). Clearly, the more distinct the predictions σ_i^A and σ_i^B are from one another, the larger this number will be. In Figure 3.2 we plot the distribution for $(\Delta S_{AB})^2$ for $n = 3$ signatures and several values of λ. As expected, the larger this parameter is, the more likely we are to find large values of $(\Delta S_{AB})^2$.

Let us assume for the moment that "model A" is the experimental data, which corresponds to an integrated luminosity of $L^{\rm exp}$. Our "model B" can then be a simulation with integrated luminosity $L^{\rm sim} = qL^{\rm exp}$. We might imagine that q can be ar-

bitrarily large, limited only by computational resources.[6] We can then rewrite (3.30) as

$$\lambda = L^{\rm exp} \sum_i \frac{(\sigma_i^A - \sigma_i^B)^2}{\sigma_i^A + \frac{1}{q}\,\sigma_i^B}\,. \tag{3.32}$$

From this expression it is clear that we can expect the value of this parameter λ to *increase* as experimental data is collected. The larger the value of $L^{\rm exp}$ the less likely it becomes to find a particularly small value of $(\Delta S_{AB})^2$. This confirms our basic intuition that given *any* observable (or set of observables) for which the two models predict different values then with sufficient integrated luminosity it should always be possible to distinguish the models to arbitrary degree of confidence.

For any given value of $\lambda \neq 0$, the probability that a measurement of $(\Delta S_{AB})^2$ will fluctuate to a value so small that it is not possible to separate two distinct models (to confidence level p) is simply the fraction of the probability distribution in (3.29) that lies to the left of the value $\gamma_n(p)$. If we wish to be at least 95% certain that our measurements will correctly recognize that two different models are indeed distinct we must require

$$P = \int_{\gamma_n(p)}^{\infty} n\,\chi^2_{n,\lambda}(n\Delta S^2_{AB})\,d(\Delta S^2_{AB}) = \int_{n\gamma_n(p)}^{\infty} \chi^2_{n,\lambda}(y)\,dy \geq 0.95\,. \tag{3.33}$$

Since the value of the integral P in (3.33) decreases monotonically as λ increases the value of this parameter which makes (3.33) an equality is the minimum non-centrality value $\lambda_{\rm min}(n,p)$ such that the two models can be distinguished.

In other words for two distinct models A and B, any combination of n experimental signatures such that $\lambda > \lambda_{\rm min}(n, p = 0.95)$ will be effective in demonstrating that the two models are indeed different 95% of the time, with a confidence level of 95%.

[6] Among other benefits of a large value for q would be the reduction in uncertainties arising from the simulation side of the comparison, *i.e.* assuming that the simulation perfectly captures both the physics and the detector response, the remaining uncertainty would be that associated with the experimental observation associated with σ_i^A.

	Confidence Level p			
n	0.95	0.975	0.99	0.999
1	12.99	17.65	24.03	40.71
2	15.44	20.55	27.41	44.99
3	17.17	22.60	29.83	48.10
4	18.57	24.27	31.79	50.66
5	19.78	25.71	33.50	52.88
6	20.86	26.99	35.02	54.88
7	21.84	28.16	36.41	56.71
8	22.74	29.25	37.69	58.40
9	23.59	30.26	38.89	59.99
10	24.39	31.21	40.02	61.48

Table 3.3: List of $\lambda_{\min}(n,p)$ values for various values of the parameters n and p. A distribution such as those in Figure 3.2 with $\lambda = \lambda_{\min}(n,p)$ will have precisely the fraction p of its total area at larger values of $(\Delta S_{AB})^2$ than the corresponding critical value $\gamma_n(p)$ from Table 3.2. A graphical example of this statement is shown in Figure 3.3.

We have successfully reduced the problem to an exercise in pure mathematics, as these $\lambda_{\min}(n,p)$ values can be calculated analytically without regard to the physics involved. A collection of values for small values of n are given in Table 3.3. Note that as we increase n the necessary value $\lambda_{\min}$ increases, reflecting the fact that as more observations are made we should expect that it will become increasingly likely that at least one will show a large deviation. Indeed, the quantity λ can be thought of as a measure of the overall distance from $(\Delta S_{AB})^2 = 0$ in the n-dimensional signature space in units of the variances. As an example, again consider the case where $n = 3$. For this value of n the corresponding $\gamma_3(0.95) = 2.61$ value can be found from Table 3.2, while we can find $\lambda_{\min}(3, 0.95) = 17.17$ from Table 3.3. We plot the distributions (3.29) for $\{n, \lambda\} = \{3, 0\}$ and $\{3, 17.17\}$ simultaneously in Figure 3.3. By construction, the area of the non-central distribution to the left of the indicated value of $((\Delta S_{AB})^2) = 2.61$ will be precisely 5% of the total area.

Having reached the end of our somewhat lengthy digression on probability theory we now return to the physics issue at hand. The requirement that $\lambda \geq \lambda_{\min}(n,p)$ can be translated into a condition on the signature set and/or luminosity via the

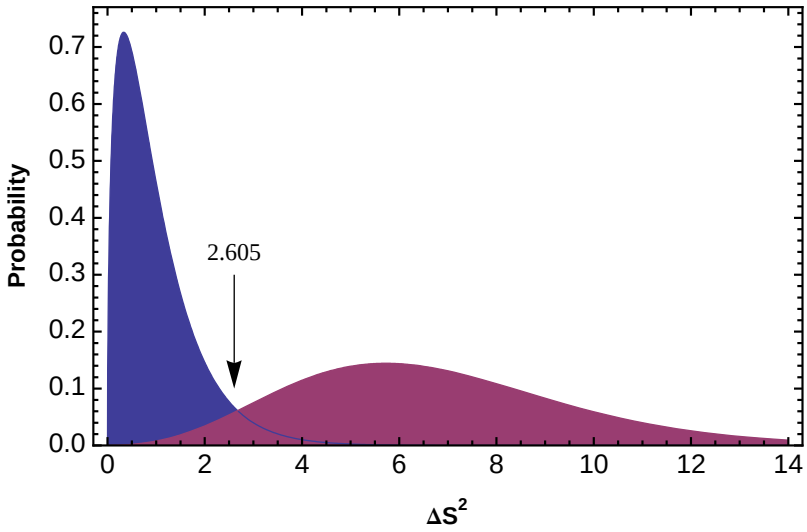

Figure 3.3: Determination of $\lambda_{\min}$ for the case $n = 3$. The plot shows an example of the distribution of $(\Delta S_{AB})^2$ for $n = 3$. The curve on the left represents $\lambda = 0$ case, i.e. values we will get when we compare a model to itself. 95% of the possible outcomes of this comparison are below 2.605 which is shown on the plot. The curve on the right has $\lambda = 17.17$ and 95% of the curve is beyond 2.605. As λ increases, this curve moves further to the right and gets flatter.

definition in (3.32). Let us make one final notational definition

$$R_{AB} = \sum_i (R_{AB})_i = \sum_i \frac{(\sigma_i^A - \sigma_i^B)^2}{\sigma_i^A + \frac{1}{q}\,\sigma_i^B} \tag{3.34}$$

where R_{AB} has the units of a cross section. Our condition for 95% certainty that we will be able to separate two truly distinct models at the 95% confidence level becomes

$$L_{\text{exp}} \geq \frac{\lambda_{\min}(n, 0.95)}{R_{AB}}\,. \tag{3.35}$$

Given two models A and B and a selection of n signatures both $\lambda_{\min}(n, 0.95)$ and R_{AB} are completely determined. Therefore the minimum amount of integrated luminosity needed to separate the models experimentally will be given by

$$L_{\min}(p) = \frac{\lambda_{\min}(n, p)}{R_{AB}}\,. \tag{3.36}$$

We will be using (3.36) repeatedly throughout the rest of this chapter. A well-chosen

set of signatures will be the set that makes the resulting value of $L_{\min}$ determined from (3.36) as small as it can possibly be.

3.3 Signature Selection

Following the discussion in Section 3.2.2 we are in a position to define the goal behind our signature selection more precisely. We wish to select a set of n signatures S_i such that the quantity $L_{\min}(p)$ as defined in (3.36), for a given value of p, is as small as it can possibly be over the widest possible array of model pairs A and B. We must also do our best to ensure that the n signatures we choose to consider are reasonably uncorrelated with one another so that the statistical treatment of the preceding section is applicable. We will address the latter issue below, but let us first turn our attention to the matter of optimizing the signature list.

3.3.1 Optimization of Signature Choice

As stated in Section 3.2, in this work we define a signature as an observable that is interpreted a count (recorded number of events), or one that simply represents an intensity (a single numerical value). An example of the first case is the number of same-sign dileptons events observed for a given integrated luminosity. Another is the number of events containing 1 lepton, and 3 b-tagged jets with transverse momentum larger than 50 GeV. Numerous variations of this class of signature are possible. The second case is obtained by integrating a statistical distribution over a defined range. For example the inclusive invariant mass distribution of a set of events may be integrated over a specific range of energy. The resulting value represents another potential signature. The same can be done for any other useful statistical observable.

We took as our starting point an extremely large initial set of possible signatures.

These included all the counting signatures and most of the kinematic distributions used in [12], all of the signatures of [101], several "classic" observables common in the literature [102] and several more which we constructed ourselves. Removing redundant instances of the same signature this yielded 46 independent counting signatures and 82 kinematic distributions represented by histograms, for 128 signatures in total. We might naively think that the best strategy is to include *all* of these signatures in the analysis (neglecting for now the issue of possible correlations among them). In fact, if the goal is statistically separating two models, the optimal strategy is generally to choose a rather small subset of the total signatures. Let us understand why that is the case. To do so we need a quantitative way of establish an absolute measure of the "power" of any given signature to separate two models A and B. This can be provided by considering the condition in (3.36). For any signature S_i we can define an individual $(L_{\min})_i$ by

$$(L_{\min})_i = \lambda_{\min}(1,p)\,\frac{\sigma_i^A + \frac{1}{q}\,\sigma_i^B}{(\sigma_i^A - \sigma_i^B)^2}\,, \tag{3.37}$$

where, for example, $\lambda_{\min}(1, 0.95) = 12.99$. This quantity is exactly the integrated luminosity required to separate models A and B, to confidence level p, by using the single observable S_i. For a list of N signatures it is possible to construct N such $(L_{\min})_i$ values and order them from smallest value (most powerful) to largest value (least powerful). If we take any subset n of these, then the requisite $L_{\min}$ that results from considering all n simultaneously is given by

$$L_{\min} = \frac{\lambda_{\min}(n,p)}{\lambda_{\min}(1,p)}\,\left\{(L_{\min})_1^{-1} + (L_{\min})_2^{-1} + \cdots + (L_{\min})_n^{-1}\right\}^{-1}\,. \tag{3.38}$$

Referring back to Table 3.3 we see that the ratio $\lambda_{\min}(n,p)/\lambda_{\min}(1,p)$ grows with n. This indicates that as we add signatures with ever diminishing $(L_{\min})_i$ values we will eventually encounter a point of negative returns, where the resulting overall $L_{\min}$

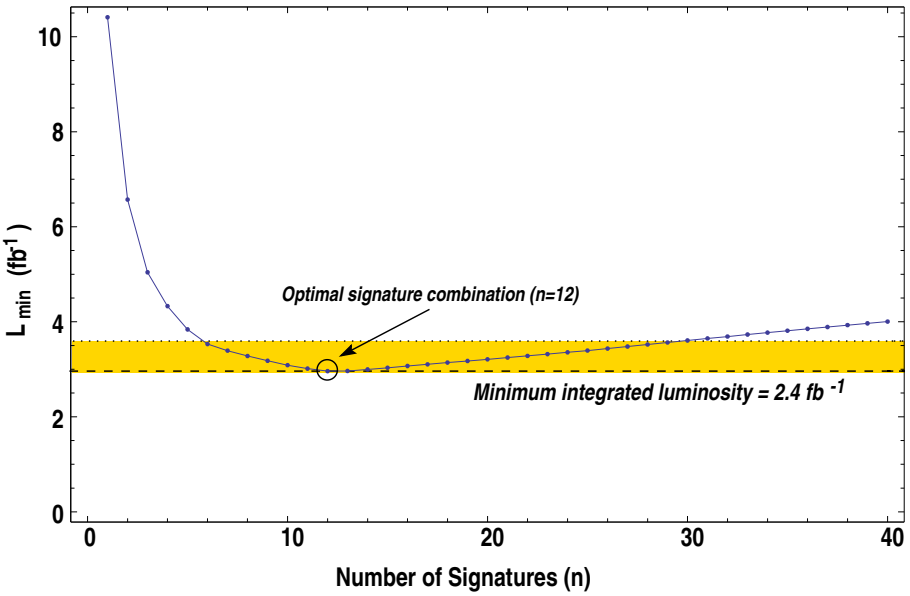

Figure 3.4: An example of finding an "optimal" signature list. By sequentially ordering the calculated $(L_{\rm min})_i$ values for any particular pair of models in ascending order, it is always possible to find the optimal set of signatures for that pair by applying (3.38). In this particular example the minimum value of $L_{\rm min}$ is found after combining just the first 12 signatures. After just the best six signatures we are already within 20% of the optimal value, as indicated by the shaded band.

starts to grow again.

As more signatures are added, the threshold for adding the next signature in the list gets steadily stronger. For a *particular pair* of models, A and B, it is always possible to find the optimal list of signatures from among a given grand set by ordering the resulting $(L_{\rm min})_i$ values and adding them sequentially until a minimum of $L_{\rm min}$ is observed. To do so, we note that kinematic distributions must be converted into counts (and all counts are then converted into effective cross sections). This conversion requires specifying an integration range for each histogram. The choice of this range can itself be optimized, by considering each integration range as a separate signature and choosing the values such that $(L_{\rm min})_i$ is minimized.

Figure 3.4, based on an actual pair of models from one of our model lines, represents the outcome of just such an optimization procedure. In this case a clearly

optimal signature set is given by the 12 signatures represented by the circled point, which yields $L_{\min} = 2.4$ fb^{-1}. The situation in Figure 3.4 is typical of the many examples we studied: the optimal signature set usually consisted of $\mathcal{O}(10)$ signatures. If we are willing to settle for a luminosity just 20% higher than this minimal value then we need only $\mathcal{O}(5)$ signatures, typically.[7] This 20% range is indicated by the shaded band in Figure 3.4. Of course this "optimal" set of signatures $\{S_i\}$ is only optimal for the specific pair of models A and B. We must repeat this optimization procedure on a large collection of model pairs and form a suitable average of the results in order to find a set of signatures $\{S_i\}$ that best approximates the truly optimal set over the widest possible set of model pairs $\{A, B\}$. The lists we will present at the end of this section represent the results of just such a procedure.

3.3.2 Correlations

We must now address the issue of correlations. To be able to use the analytic results of our statistical presentation of the problem in Section 3.2.2 we must be careful to only choose signatures from a list in which all the members are uncorrelated with one another. This immediately suggests a dilemma: once a signature is chosen, many others in the grand set will now be excluded for being correlated with the first. This complicates the process of optimization considerably – the task now becomes to perform the above optimization procedure over the largest possible list of *uncorrelated* (or at least minimally correlated) signatures. To find the correlation between any two signatures S_i and S_j it is sufficient to construct their correlation coefficient ρ_{ij}, given by

$$\rho_{ij} = \frac{\mathrm{cov}(i,j)}{\mathrm{var}(i)\mathrm{var}(j)} = \lim_{N\to\infty} \frac{\frac{1}{N}\sum_k \left[\bar{\sigma}_i^k - \sigma_i\right]\left[\bar{\sigma}_j^k - \sigma_j\right]}{\sqrt{\frac{1}{N}\sum_k \left[\bar{\sigma}_i^k - \sigma_i\right]^2}\sqrt{\frac{1}{N}\sum_k \left[\bar{\sigma}_j^k - \sigma_j\right]^2}}\,, \tag{3.39}$$

[7] It is interesting to compare this to the results of [12] in which the effective dimension of signature space was found to be also $\mathcal{O}(5)$ to $\mathcal{O}(10)$.

Object	Minimum p_T	Minimum $\|\eta\|$
Photon	20 GeV	2.0
Electron	20 GeV	2.0
Muon	20 GeV	2.0
Tau	20 GeV	2.4
Jet	50 GeV	3.0

Table 3.4: Initial cuts to keep an object in the event record. After event reconstruction using the package `PGS4` we apply additional cuts to the individual objects in the event record. Detector objects that fail to meet the above criteria are removed from the event record and do not enter our signature analysis. These cuts are applied to all analysis described in this work.

where the $\bar{\sigma}^k$ represent the individual results obtained from each of the N cross section measurements, labeled by the index k.

In our analysis we estimated the entries in the 128×128 dimensional matrix of (3.39) in the following crude manner. We began with a simple MSSM model specified by a parameter set as in (3.18), with gaugino masses having the unified ratios of (3.2). We simulated this model $N = 2000$ times, each time with a different random number seed. The simulation involved generating 5 fb^{-1} of events using `PYTHIA 6.4`, which were passed to the detector simulator `PGS4`. After simulating the detector response and object reconstruction the default level-one triggers included in the `PGS4` detector simulation were applied. Further object-level cuts were then performed, as summarized in Table 3.4. After these object-specific cuts we then applied an event-level cut on the surviving detector objects similar to those used in [12]. Specifically we required all events to have missing transverse energy $\not{E}_T > 150$ GeV, transverse sphericity $S_T > 0.1$, and $H_T > 600$ GeV (400 GeV for events with 2 or more leptons) where $H_T = \not{E}_T + \sum_{\text{Jets}} p_T^{\text{jet}}$. Once all cuts were applied the grand list of 128 signatures was then computed for each run, and from these signatures the covariance matrix in (3.39) was constructed. All histograms and counting signatures were constructed and analyzed using the `ROOT`-based analysis package `Parvicursor` [103].

Not surprisingly, many of the signatures considered in our grand list of 128 ob-

servables were highly correlated with one another. For example, the distribution of transverse momenta for the hardest jet in any event was correlated with the overall effective mass of the jets in the events (defined as the scalar sum of all jet p_T values: $M_{\text{eff}} = \sum_{\text{Jets}} p_T^{\text{jet}}$). Both were correlated with the distribution of H_T values for the events, and so forth. The consistency of our approach would then require that only a subset of these signatures can be included. One way to eliminate correlations is to partition the experimental data into mutually-exclusive subsets through some topological criteria such as the number of jets and/or leptons. For example, the distribution of H_T values in the set having any number of jets and zero leptons will be uncorrelated with the same signature in the set having any number of jets and at least one lepton. Our analysis indicated that this partitioning strategy has its limitations, however. The resolving power of any given signature tends to diminish as the set it is applied to is made ever more exclusive. This is in part due to the diminishing cross-section associated with the more exclusive final state (recall that our metric for evaluating signatures is proportional to the cross-section). It is also the case that the statistical error associated with extracting these cross-section values from the counts will grow as the number of events drops. We were thus led to consider a very simple two-fold partitioning of the data:

$$\begin{aligned} N_{\text{jets}} \leq 4 \text{ versus } N_{\text{jets}} \geq 5, \\ N_{\text{leptons}} = 0 \text{ versus } N_{\text{leptons}} \geq 1. \end{aligned} \tag{3.40}$$

This choice of data partitioning is reflected in the signature tables at the end of this section.

In practice, it will likely be necessary to accept some level of correlation among the final set of chosen signatures. We do not address the issue of what effect allowing large correlations will have on our approach. However, we expect that allowing

	Description	Min Value	Max Value
1	$M_{\text{eff}}^{\text{any}} = \not{E}_T + \sum_{\text{all}} p_T^{\text{all}}$ [All events]	1250 GeV	End

Table 3.5: Signature List A. The effective mass formed from the transverse momenta of all objects in the event (including the missing transverse energy) was the single most effective signature of the 128 signatures we investigated. Since this "list" is a single item it was not necessary to partition the data in any way. For this distribution we integrate from the minimum value of 1250 GeV to the end of the distribution.

increased correlations will lead to an underestimation of L_{min}. Consider that L_{min} is computed using only a single signature. If L_{min} is then re-computed using two signatures, where each is exactly the single signature used in the first case, we see that the two signatures are 100% correlated, and from equation (3.36) one finds an artificially lower value of L_{min} despite introducing no additional discriminatory information.

3.3.3 Final Signature Choices

By utilizing the optimization procedure discussed in the previous sections we produced several example signature sets, which we then applied to our problem of distinguishing a model with $\alpha = 0$ from one with $\alpha \neq 0$. The results of this analysis will appear in the next section. Here we discuss the signature sets themselves.

To begin, we constructed a large number of model families in the manner described in Section 3.2.1, each involving the range $-0.5 \leq \alpha \leq 1.0$ for the parameter α in steps of $\Delta\alpha = 0.05$. For each point along these model lines we generated 100,000 events using `PYTHIA 6.4` and `PGS4`. To this we added an appropriately-weighted Standard Model background sample consisting of 5 fb^{-1} each of $t/\bar{t}$ and $b/\bar{b}$ pair production, high-p_T QCD dijet production, single $W^{\pm}$ and Z-boson production, pair production of electroweak gauge bosons (W^+W^-, $W^{\pm}Z$ and ZZ), and Drell-Yan processes.

To examine which of our 128 signatures would be effective in measuring the value of the parameter α we fixed "model A" to be the point on each of the model lines

	Description	Min Value	Max Value
1	$M_{\rm eff}^{\rm jets}$ [0 leptons, ≥ 5 jets]	1100 GeV	End
2	$M_{\rm eff}^{\rm any}$ [0 leptons, ≤ 4 jets]	1450 GeV	End
3	$M_{\rm eff}^{\rm any}$ [≥ 1 leptons, ≤ 4 jets]	1550 GeV	End
4	p_T(Hardest Lepton) [≥ 1 lepton, ≥ 5 jets]	150 GeV	End
5	$M_{\rm inv}^{\rm jets}$ [0 leptons, ≤ 4 jets]	0 GeV	850 GeV

Table 3.6: Signature List B. The collection of our most effective observables, restricted to the case where the maximum correlation between any two of these signatures is 10%. Note that the jet-based effective mass variables would normally be highly-correlated if we had not partitioned the data according to (3.40). For these distributions we integrate from "Min Value" to "Max Value".

with $\alpha = 0$ and then treated each point along the line with $\alpha \neq 0$ as a candidate "model B." As discussed in Section 3.3.1, each model line we investigated – and each α value along that line – gave slightly different sets of maximally effective signatures. The lists we will present in Tables 3.5, 3.6 and 3.7 represent an ensemble average over these model lines, restricted to some maximum level of correlation ϵ. In what follows we present example signature lists assuming $\epsilon = 10\%$ and $\epsilon = 30\%$.

Let us begin with Table 3.5, which gives the single most effective signature at separating models with different values of the parameter α. It is the effective mass formed from all objects in the event

$$M_{\rm eff}^{\rm any} = \not{E}_T + \sum_{\rm all} p_T^{\rm all} \,, \tag{3.41}$$

where we form the distribution from all events which pass our initial cuts. That this one signature would be the most powerful is not a surprise given the way we have set up the problem. It is the most inclusive possible signature one can imagine (apart from the overall event rate itself) and therefore has the largest overall cross-section. Furthermore, the variable in (3.41) is sensitive to the mass differences between the gluino mass and the lighter electroweak gauginos – precisely the quantity that is governed by the parameter α. Yet as we will see in Section 3.4 this one signature can often fail to be effective at all in certain circumstances, resulting in a rather

large required $L_{\min}$ to be able to separate $\alpha = 0$ from non-vanishing cases. In addition it is built from precisely the detector objects that suffer the most from experimental uncertainty. This suggests a larger and more varied set of signatures would be preferable.

We next consider the five signatures in Table 3.6. These signatures were chosen by taking our most effective observables and restricting ourselves to that set for which $\epsilon = 10\%$. We again see the totally inclusive effective mass variable of (3.41) as well as the more traditional effective mass variable, $M_{\text{eff}}^{\text{jets}}$, defined via (3.41) but with the scalar sum of p_T values now running over the jets only. We now include the p_T of the hardest lepton in events with at least one lepton and five or more jets, as well as the invariant mass $M_{\text{inv}}^{\text{jets}}$ of the jets in events with zero leptons and 4 or less jets. The various jet-based effective mass variables would normally be highly correlated with one another if we were not forming them from disjoint partitions of the overall data set. The favoring of jet-based observables to those based on leptons is again largely due to the fact that jet-based signatures will have larger effective cross-sections for reasonable values of the SUSY parameters in (3.18) than leptonic signatures. The best signatures are those which track the narrowing gap between the gluino mass and the electroweak gauginos and the narrowing gap between the lightest chargino/second-lightest neutralino mass and the LSP mass. In this case the first leptonic signature to appear – the transverse momentum of the leading lepton in events with at least one lepton – is an example of just such a signature.

Finally, let us consider the larger ensemble of signatures in Table 3.7. In this final set we have relaxed our concern over the issue of correlated signatures, allowing as much as 30% correlation between any two signatures in the list. This allows for a larger number as well as a wider variety of observables to be included. As we will see

	Description	Min Value	Max Value
	Counting Signatures		
1	N_ℓ [≥ 1 leptons, ≤ 4 jets]		
2	$N_{\ell^+\ell^-}$ [$M_{\rm inv}^{\ell^+\ell^-} = M_Z \pm 5$ GeV]		
3	N_B [≥ 2 B-jets]		
	[0 leptons, ≤ 4 jets]		
4	$M_{\rm eff}^{\rm any}$	1000 GeV	End
5	$M_{\rm inv}^{\rm jets}$	750 GeV	End
6	$\not{E}_T$	500 GeV	End
	[0 leptons, ≥ 5 jets]		
7	$M_{\rm eff}^{\rm any}$	1250 GeV	3500 GeV
8	$r_{\rm jet}$ [3 jets > 200 GeV]	0.25	1.0
9	p_T(4th Hardest Jet)	125 GeV	End
10	$\not{E}_T/M_{\rm eff}^{\rm any}$	0.0	0.25
	[≥ 1 leptons, ≥ 5 jets]		
11	$\not{E}_T/M_{\rm eff}^{\rm any}$	0.0	0.25
12	p_T(Hardest Lepton)	150 GeV	End
13	p_T(4th Hardest Jet)	125 GeV	End
14	$\not{E}_T + M_{\rm eff}^{\rm jets}$	1250 GeV	End

Table 3.7: Signature List C. In this collection of signatures we have allowed the maximum correlation between any two signatures to be as high as 30%. Note that some of the signatures are normalized signatures, (#8, #10 and #11), while the first three are truly counting signatures. A description of each of these observables is given in the text. For all distributions we integrate from "Min Value" to "Max Value".

in Section 3.4 this can be very important in some cases in which the supersymmetric model has unusual properties, or in cases where the two α values being considered give rise to different mass orderings (or hierarchies) in the superpartner spectrum. In displaying the signatures in Table 3.7 we find it convenient to group them according to the partition of the data being considered. Note that the counting signatures are taken over the entire data set.

The first counting signature is simply the total size of the partition from (3.40) in which the events have at least one lepton and 4 or less jets. This was the only observable taken on this data set that made our list of the most effective observables. The next two signatures are related to "spoiler" modes for the trilepton signal. Note that the trilepton signal itself did *not* make the list: this is a wonderful discovery mode for supersymmetry, but the event rates between a model with $\alpha = 0$ and one with non-vanishing α were always very similar (and low). This made the trilepton count-

ing signature ineffective at distinguishing between models. By contrast, counting the number of b-jet pairs (a proxy for counting on-shell Higgs bosons) or the number of opposite-sign electron or muon pairs whose invariant mass was within 5 GeV of the Z-mass (a proxy for counting on-shell Z-bosons) *were* excellent signatures for separating models from time to time. This was especially true when the two models in question had very different values of α such that the mass differences between $\widetilde{N}_2$ and $\widetilde{N}_1$ were quite different in the two cases. We will give specific examples of such outcomes in Section 3.4.

The following three sections of Table 3.7 involve some of the same types of observables as in the previous tables, with a few notable changes and surprises. First note that several of the observables in Table 3.7 involve some sort of normalization. In particular numbers 8, 10 and 11. Our estimate of the correlations among signatures found that the fluctuations of these normalized signatures tended to be less correlated with other observables for that partition than the un-normalized quantities. However, normalizing signatures in this way also tended to reduce their ability to distinguish models. Signature #8 is defined as the following ratio

$$r_{\rm jet} \equiv \frac{p_T^{\rm jet3} + p_T^{\rm jet4}}{p_T^{\rm jet1} + p_T^{\rm jet2}} \tag{3.42}$$

where $p_T^{\rm jet\,i}$ is the transverse momentum of the i-th hardest jet in the event. For this signature we require that there be at least three jets with $p_T > 200$ GeV. This signature, like the p_T of the hardest lepton or the p_T of the 4th hardest jet, was effective at capturing the increasing softness of the products of cascade decays as the value of α was increased away from $\alpha = 0$.

Let us note that Lists A, B and C are not mutually disjoint. For example, signatures 4, 5 and 12 of Table 3.7 also appear in Table 3.6. The signature mix is determined by attempting to minimize $L_{\rm min}$ via the formula in (3.38) while attempt-

ing to keep the correlations between any pair of signatures below the targets set above in the text. As mentioned earlier, larger lists are not always better – the more signatures one adds, the larger the likelihood that some pair will be correlated with one another to an unsatisfactory amount. Furthermore, when signatures are added which are only occasionally useful, the resolving power of the ensemble can actually be degraded since the statistical threshold defined by $\lambda_{\rm min}$ in Table 3.3 grows with the number of signatures.

We will see some examples of this perverse effect in the next section in which we will examine the effectiveness of these three lists. We will do this first against our benchmark models from Section 3.1 and then against a large ensemble of random MSSM model lines. Before doing so let us note that by fixing a particular set of n signatures in every instance – and indeed, with the fixed integration ranges indicated in the Tables – we are very likely to often be far from the *optimal* signature mix and integration ranges. That is, we should not expect to achieve the absolute $L_{\rm min}$ value of Figure 3.4 for any particular pair or points along a model line. If we have chosen our signature list well, however, then we can hope that the result of adding the contributions of all n signatures using (3.38) will be close to the optimal $L_{\rm min}$ value over a large array of model pairs.

3.4 Analysis Results

In this section we will examine how well our signature lists in Tables 3.5, 3.6 and 3.7 perform in measuring the value of the parameter α which appears in (3.1). Recall that, for simplicity, our specific goal is to distinguish between a model with $\alpha = 0$ and another with *all other soft terms held equal*, but with $\alpha \neq 0$. We would like to do this with the least amount of data (or integrated luminosity) as possible for

Parameter	Point A	Point B		Parameter	Point A	Point B
$m_{\widetilde{N}_1}$	85.5	338.7		$m_{\tilde{t}_1}$	844.7	379.9
$m_{\widetilde{N}_2}$	147.9	440.2		$m_{\tilde{t}_2}$	1232	739.1
$m_{\widetilde{N}_3}$	485.3	622.8		$m_{\tilde{c}_L}$, $m_{\tilde{u}_L}$	1518	811.7
$m_{\widetilde{N}_4}$	494.0	634.3		$m_{\tilde{c}_R}$, $m_{\tilde{u}_R}$	1520	793.3
$m_{\widetilde{C}_1^\pm}$	147.7	440.1		$m_{\tilde{b}_1}$	1224	676.8
$m_{\widetilde{C}_2^\pm}$	494.9	635.0		$m_{\tilde{b}_2}$	1507	782.4
$m_{\tilde{g}}$	510.0	818.0		$m_{\tilde{s}_L}$, $m_{\tilde{d}_L}$	1520	815.4
μ	476.1	625.2		$m_{\tilde{s}_R}$, $m_{\tilde{d}_R}$	1520	793.5
m_h	115.2	119.5		$m_{\tilde{\tau}_1}$	1487	500.4
m_A	1557	807.4		$m_{\tilde{\tau}_2}$	1495	540.4
m_{H^0}	1557	806.8		$m_{\tilde{\mu}_L}$, $m_{\tilde{e}_L}$	1500	545.1
$m_{H^\pm}$	1559	811.1		$m_{\tilde{\mu}_R}$, $m_{\tilde{e}_R}$	1501	514.6

Table 3.8: Low energy physical masses for benchmark points. Low energy physical masses (in units of GeV) are given at the scale 1 TeV. All points are taken to have $\mu > 0$. The actual value of $\tan\beta$ is fixed in the electroweak symmetry-breaking conditions.

the smallest values of α possible. We will first demonstrate how the lists perform on our benchmark cases before turning to an analysis of their performance on a large ensemble of randomly-generated supersymmetric models.

3.4.1 Benchmark Models Analysis

We begin with the theory-motivated benchmark models briefly mentioned at the end of Section 3.1. The input values for the soft supersymmetry-breaking parameters are listed in Table 3.1 at the very end of Section 3.1. To remind the reader, model A is an example of a heterotic string compactification with Kähler stabilization of the dilaton while model B is an example of a Type IIB string model with flux compactification. Each of these examples predicts a particular value of α as a function of other parameters in the theory; specifically, model A predicts $\alpha \simeq 0.3$, while model B predicts $\alpha \simeq 1$.

The input values of Table 3.1 were evolved from the input scale $\Lambda_{\rm UV} = 2\times10^{16}$ GeV to the electroweak scale of 1 TeV by solving the renormalization group equations. For this we use the computer package `SuSpect` [104], utilizing two-loop running for

all parameters *except* for the gaugino masses. For these we use one-loop RGEs only in order to maintain the parametrization for the gaugino soft parameters in terms of α given by (3.1). Once run to the low scale the physical spectra and mixings of the models were computed by `SuSpect`. The result of this process for our two benchmark models is given in Table 3.8.

From here we performed a simulation using the combined package of `PYTHIA` + `PGS4` as described in Section 3.3. For each of these two models a model-line was generated by varying the parameter α from $\alpha = 0$ to $\alpha = 1$, in increments of 0.05, while keeping all other soft parameters fixed. Along these model lines the gluino soft mass M_3 was held constant to set the overall scale, and the two parameters M_1 and M_2 were varied according to the ratios in (3.1). For each point 500,000 events were generated using the L1 trigger options in `PGS4`. After applying further initial cuts as described in Section 3.3 the signatures associated with each of the three lists in Tables 3.5, 3.6 and 3.7 were constructed. We then used the criterion for distinguishability described in Section 3.2.2 to determine the minimum luminosity $L_{\min}$ needed to separate $\alpha = 0$ from all other points along the line.

The results of this analysis are presented in the top panels of Figure 3.5. The plot on the left corresponds to benchmark model A while the one on the right corresponds to benchmark model B. The vertical axis shows the minimum luminosity needed to separate a given $\alpha \neq 0$ scenario from the unified case of $\alpha = 0$. The three shaded regions represent the three model lists we used to analyze the data. At the lower edge of each region is the value of $L_{\min}$ as calculated using the relations in (3.37) and (3.38). The upper edge of each region represents an estimate of the 1 sigma upper bound on the calculated value of $L_{\min}$ caused by statistical fluctuations (*i.e.* the fact that the cross-sections extracted from the data or simulation are not the true

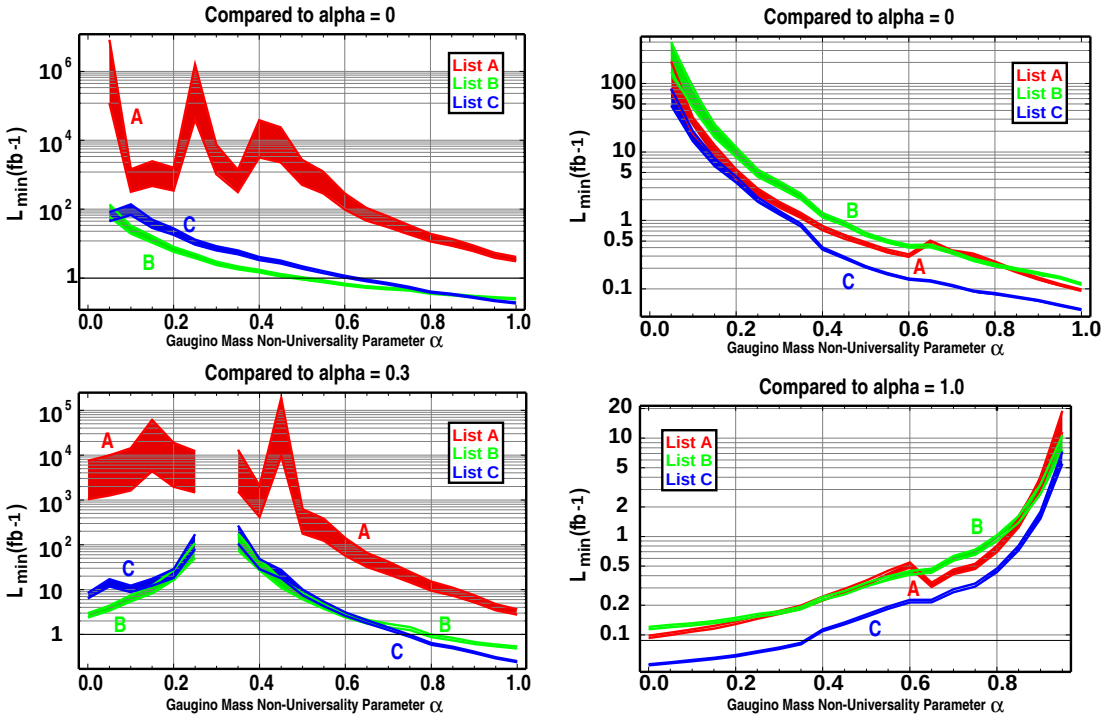

Figure 3.5: $L_{\min}$ as a function of α for the two benchmark models. The three shaded regions correspond to the three signature lists as indicated by the legend. The lower bound of each shaded region indicates the minimum integrated luminosity $L_{\min}$ needed to separate the model with the specified α from $\alpha = 0$ (top panels) or the predicted value of α (lower panels). The upper bound of the shaded region represents an estimate of the 1 sigma upper bound on the calculated value of $L_{\min}$ caused by statistical fluctuations.

cross-sections for each signature). The lower panels in Figure 3.5 represent the same analysis, but now each of the two models are compared to their predicted values: $\alpha = 0.3$ for model A and $\alpha = 1.0$ for model B. With the exception of the straw-man List A in the case of benchmark model A, all the lists do an adequate job of distinguishing points along these alpha-lines with moderate amounts of integrated luminosity. Naturally, as the two points being compared approach one another the signature difference between them become smaller and the needed $L_{\min}$ increases. It is instructive to consider the case of model A to understand why some approaches to extracting the parameter α succeed and others fail.

Model A has nearly universal scalar masses at a rather high scale of approxi-

mately 1.5 TeV, yet the light gluino makes this the model with the higher overall cross-section. All supersymmetric observables in this benchmark model are therefore dominated by gluino pair production and their eventual cascade decays through highly off-shell squarks. In the analysis the gluino mass is kept constant along an alpha-line, so the cross-section for the dominant process $gg \to \tilde{g}\tilde{g}$ is fixed at $\sigma(gg \to \tilde{g}\tilde{g}) = 13.4\,\text{pb}$ for this alpha-line. Any signatures related to this variable will depend on α only via the change in the gluino branching fractions, which are nearly constant as a function of the parameter α.[8] Blunt signatures like the total M_{eff} variable of (3.41) indicate roughly the total production cross-section and crude mass scale of the superpartner being predominantly produced. This is an example in which the most inclusive possible observable is simply too inclusive to detect the change in gaugino mass ratios. For this one must consider processes that produce electroweak gauginos, which are subdominant by as much as a factor of ten in the case of benchmark model A.

Further compounding the problems for the inclusive signature of List A is the fact that the count rate for this particular final state is varying only very slowly with α. Despite the fact that this count rate can be quite large in this model, the resulting value of L_{min} is high because the ΔS_{AB} value for this particular signature is very near zero. As a result, small statistical fluctuations in the data or the simulation result in large fluctuations in the resulting value of L_{min} needed to truly separate different values of the parameter α. This reflects itself in both the width of the shaded region in the left panels of Figure 3.5 and in the volatility of the extracted value itself. In Figure 3.6 we plot the distribution of the List A variable (3.41) in benchmark model A for the case of $\alpha = 0$ (solid line) and $\alpha = 1$ (dashed line). Above our

[8] Only the highly suppressed three-body decay $\tilde{g} \to \tilde{C}_1 q\bar{q}'$ with q and $\bar{q}'$ representing third-generation quarks shows any significant dependence on the value of the parameter α for this benchmark model.

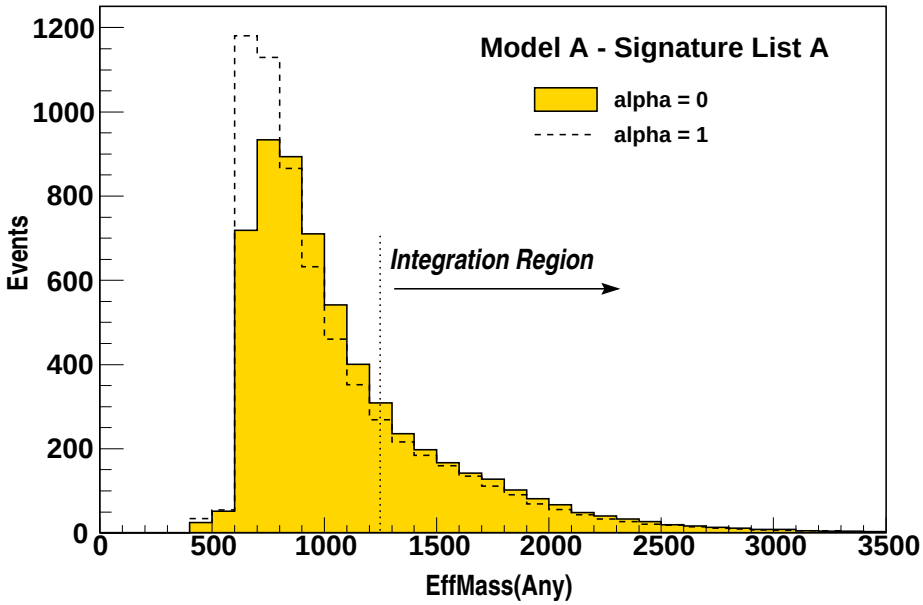

Figure 3.6: Distribution of the variable $M_{\rm eff}^{\rm any}$ from signature List A for benchmark model A. Solid filled histogram is the case for $\alpha = 0$, dotted histogram is the case for $\alpha = 1$. The lower bound for the integration region is indicated by the dotted line at 1250 GeV. The sharp lower bound in the distribution is an artefact of the event-level cuts imposed on the data as described in Section 3.3. In this case the failure of List A to separate the two cases is apparent: the difference between the two histograms is negligible above the value $M_{\rm eff}^{\rm any} = 1250$ GeV. The resolving power would improve dramatically if this lower bound was relaxed to $M_{\rm eff}^{\rm any} = 500$ GeV, as demonstrated in Figure 3.7.

integration cut of 1250 GeV there is very little difference between the distributions, even for this extreme case. However, it is clear that some discrimination power is available had we chosen a different lower bound for integration. When the lower bound on this particular variable is relaxed to 500 GeV the inclusive $M_{\rm eff}$ variable becomes competitive with the other signature lists, as shown in Figure 3.7.

Benchmark model A therefore provides us with an example where the procedure of optimizing the signature list over a wide ensemble of models has produced a prescription that is most definitely *not* optimal for this particular case. Once a particular model framework is established it will of course be possible to tailor analysis techniques to optimize the statistical power of any given signature. But for our quasi-model-independent analysis we must forgo optimization in favor of generality.

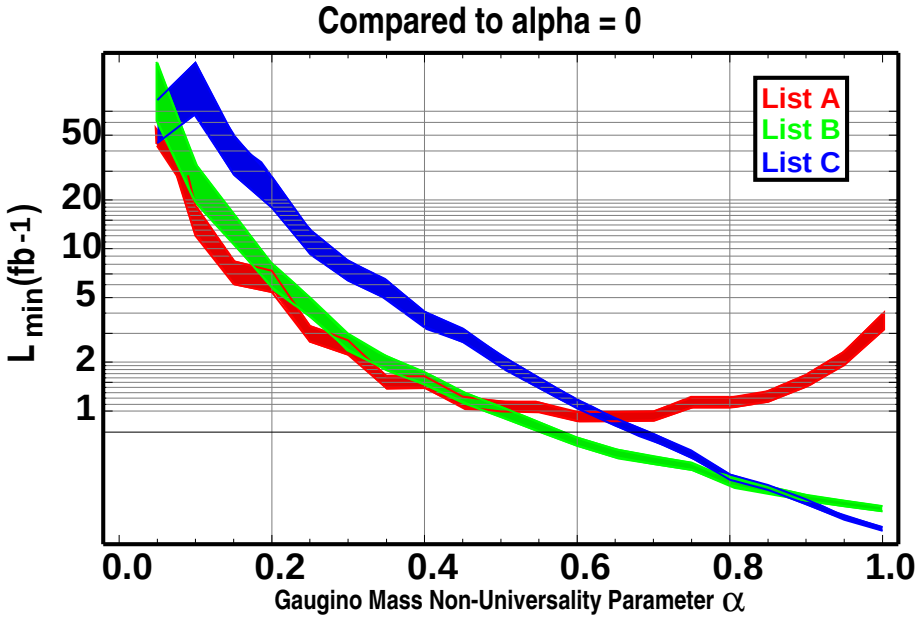

Figure 3.7: $L_{\rm min}$ as a function of α for benchmark model A with relaxed lower bound on $M_{\rm eff}^{\rm any}$. The three shaded regions correspond to the three signature lists as in the upper left panel of Figure 3.5. In this case the lower bound of the integration range for the single observable of List A has been relaxed to 500 GeV.

Nevertheless, we gain resolving power by simply expanding the list of signatures to include those which are more sensitive to the changes in the lower-mass electroweak gaugino spectrum. Returning to the left panels of Figure 3.5 it is clear that Lists B and C do far better at measuring the parameter α than the single $M_{\rm eff}$ variable alone. For example, the jet invariant mass variables in both lists, as well as the normalized $\not{E}_T$ signatures and $p_T(\text{Jet}_4)$ observable of List C are much more sensitive to changes in α for this benchmark model than the observable in (3.41).

But note the *reduction* in resolving power that occurs when we choose the largest signature list. As discussed in Section 3.3, it is clear that the largest possible signature list is not always the most effective at separating two theories. In this particular example many of the additional observables in List C are not at all helpful in separating different α values – particularly the counting variables for which the total

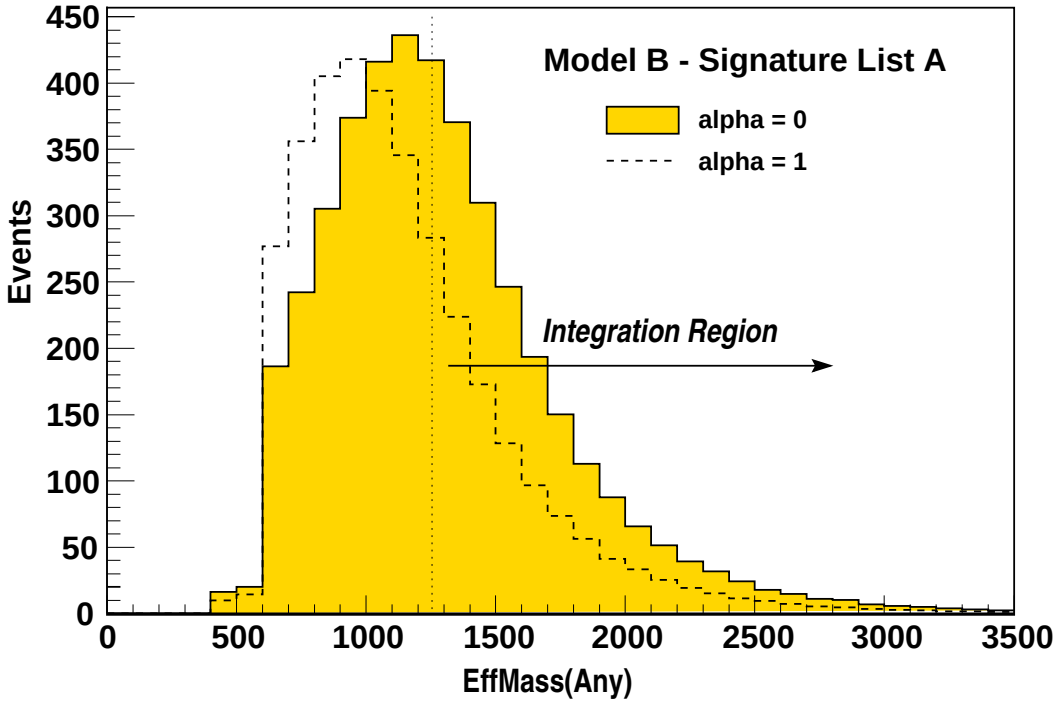

Figure 3.8: Distribution of the variable $M_{\rm eff}^{\rm any}$ from signature List A for benchmark model B. Solid filled histogram is the case for $\alpha = 0$, dotted histogram is the case for $\alpha = 1$. The lower bound for the integration region is indicated by the dotted line at 1250 GeV. The sharp lower bound in the distribution is an artefact of the event-level cuts imposed on the data as described in Section 3.3.

rates are low and the differences across the alpha-line are small. These additional variables were designed to be most effective when the mass hierarchies in the superpartner spectrum change as the value of α is modified, so that dramatic changes in production rates and/or branching ratios occur. Such threshold effects do not occur over the α range probed in benchmark model A, but do in fact occur for benchmark model B. This is clearly evident in the right panels of Figure 3.5, where additional resolving power is obtained when using the expanded signature List C.

We note that the single inclusive variable of (3.41) is much more effective in benchmark model B in part because the production cross-sections for all $SU(3)$-charged superpartners are roughly equal in magnitude. The inclusive $M_{\rm eff}$ variable no longer tracks the mass and decay products of a single heavy state so variations

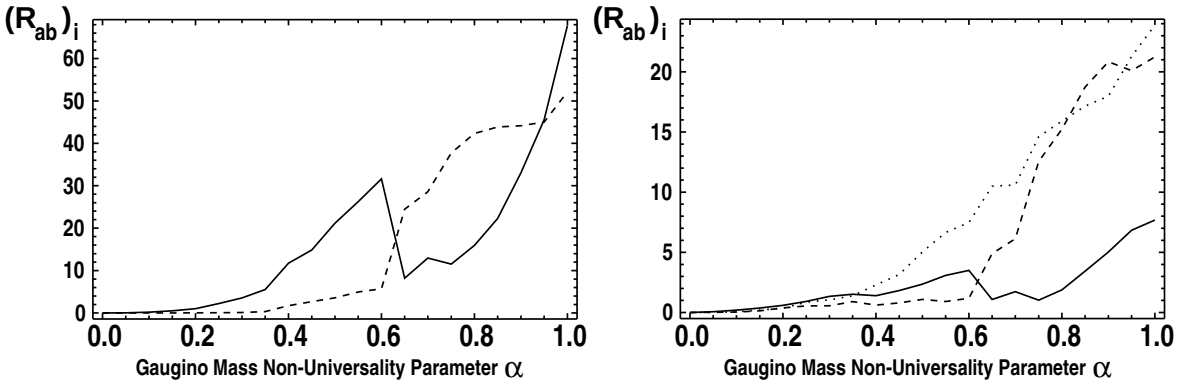

Figure 3.9: Values of $(R_{AB})_i$ for the five signatures of List B as a function of α for benchmark model B. The ability of each individual signature from List B to resolve the case $\alpha = 0$ from the indicated value of α is given by the height of the curve $(R_{AB})_i$ in the above plots. In the left panel we display signature 1 (solid curve) and signature 5 (dashed curve). In the right panel we display signature 2 (solid curve), signature 3 (dashed curve) and signature 4 (dotted curve).

with the parameter α are now more prominent. This is shown in Figure 3.8, which should be compared to the case of model A in Figure 3.6. Note that the total area under the two curves in Figure 3.8 is nearly identical, highlighting the need to choose a wise value of the lower bound on the integration region to achieve a high degree of differentiation. Model B is similar to the randomly-generated models we used to design our signature lists and thus the chosen value of 1250 GeV for this particular observable is close to what would be the optimal choice for this particular model comparison.

Despite the lower overall cross-section for the supersymmetric signal in benchmark model B, the three signature lists succeed in distinguishing the case $\alpha = 0$ from non-vanishing cases with far less integrated luminosity. In large part this is due to the richness of the particle spectrum for this model. The superpartner masses given in Table 3.8 are for the case $\alpha = 1$. As α approaches zero the masses of the lighter neutralinos and lightest chargino fall relative to that of the gluinos and squarks

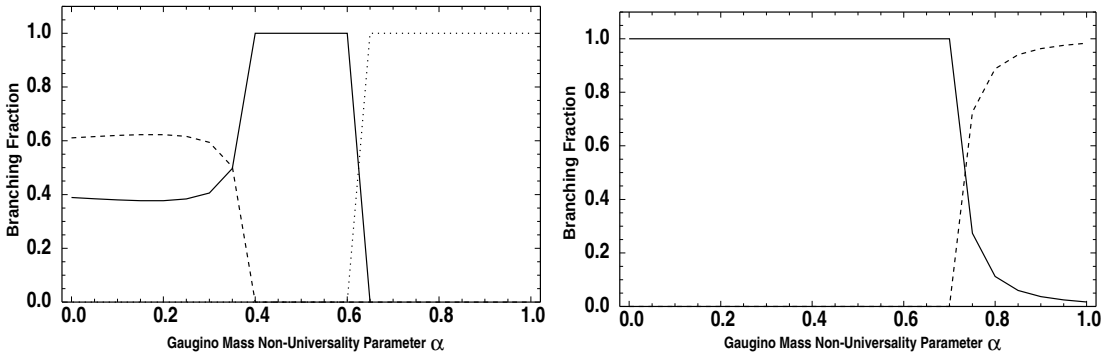

Figure 3.10: Branching fractions for principal decay modes of lightest stop (left panel) and lightest chargino (right panel) as a function of α for benchmark model B. In the left panel the decay modes are $\tilde{t}_1 \to \tilde{N}_1 t$ (dashed curve), $\tilde{t}_1 \to \tilde{C}_1^+ b$ (solid curve), and $\tilde{t}_1 \to \tilde{N}_1 c$ (dashed curve). In the right panel the decay modes are $\tilde{C}_1 \to \tilde{N}_1 W$ (solid curve) and $\tilde{C}_1 \to \tilde{t}_1 \bar{b}$ (dashed curve).

(which remain constant). Along this alpha-line several important thresholds are crossed, resulting in dramatic changes in the relevant branching fractions for the heavier states. The mix of signatures in List B and List C that contribute most strongly to the resolving power of the overall list changes as we move along the alpha-line. For example, consider the $(R_{AB})_i$ values of (3.34) for the five signatures of List B. We plot these values in Figure 3.9 for model A corresponding to $\alpha = 0$ and model B corresponding to the indicated value of $\alpha \neq 0$.

To understand these curves, we first note that the dominant SUSY production processes in benchmark model B are the pair production of stops and associated production of light squarks with a gluino. The branching fraction for three of the more important decay modes of the stop are plotted versus the parameter α in the left panel of Figure 3.10. For values of $\alpha \lesssim 0.35$, when both the chargino $\tilde{C}_1$ and the LSP $\tilde{N}_1$ are sufficiently light, the direct two-body decay into the LSP and a top quark is dominant. About 50% of the time the W-bosons from the top decays on both sides of the events will decay hadronically and the event will be captured by the first observable in List B. For the intermediate region $0.35 \lesssim \alpha \lesssim 0.6$ the

stop decays predominantly via $\tilde{t}_1 \to \tilde{C}_1 b$ and the final state topology is determined by the subsequent decay of the chargino. The branching fractions for the primary decay channels of the chargino $\tilde{C}_1$ are given in the right panel of Figure 3.10. In this intermediate α region the chargino is decaying primarily to a W-boson, populating all of the signatures in List B.

For larger values of $\alpha \gtrsim 0.6$ the chargino $\tilde{C}_1$ and the LSP $\tilde{N}_1$ are now massive enough that the only decay channel available for the stops is the process $\tilde{t}_1 \to \tilde{N}_1 c$, producing $\not{E}_T$ and two jets only. These events are captured by the second and (especially) fifth observables in List B, as evidenced by their rapid growth in significance. For $\alpha \gtrsim 0.7$ charginos that are directly produced (or produced through cascade decays of heavier squarks) will now decay *into* stops via $\tilde{C}_1 \to \tilde{t}_1 b \to \tilde{N}_1 cb$. This boosts the resolving power of the signatures with lepton vetoes relative to the other signatures in List B.

Similar arguments explain the behavior of the expanded list of observables in List C. Here we will only take a moment to mention the counting signatures which make their first appearance in our analysis. Generally speaking, counting signatures are sensitive only to the total cross-section for the final state being counted. Changes in the p_T of Standard Model particles produced in cascades are washed out, making them less useful for comparing different gaugino mass hierarchies. Counting signatures are therefore only effective when the two α values being compared correspond to different decay patterns altogether. This happens in several instances in benchmark model B, as we indicated above. The counting signatures in List C are specifically designed to consider changes in the decay table for the next-to-lightest neutralino $\tilde{N}_2$ – particularly the appearance of the so-called "spoiler" modes for the classic trilepton signal. In the left panel of Figure 3.11 the primary decay modes of

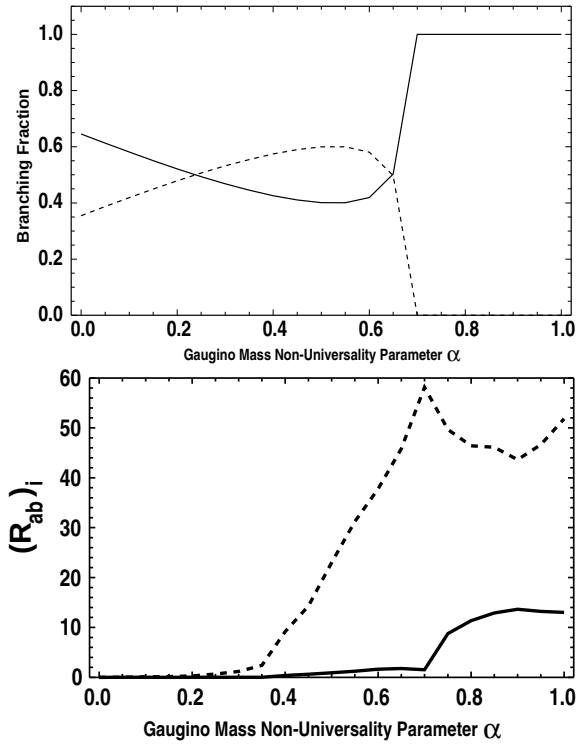

Figure 3.11: Branching fraction for next-to-lightest neutralino (left) and $(R_{AB})_i$ values for key counting signatures from List C (right). The branching fraction of the next-to-lightest neutralino $\tilde{N}_2$ for benchmark model B is plotted as a function of α in the left panel. The decay modes are $\tilde{N}_2 \to \tilde{N}_1\, h$ (dashed curve) and $\tilde{N}_2 \to \tilde{N}_1\, Z$ (solid curve). In the right panel the $(R_{AB})_i$ values for the inclusive leptonic counting signature (signature 1 – solid curve) and the inclusive B-jet counting signature (signature 3 – dashed curve) are plotted as function of α.

the next-to-lightest neutralino $\tilde{N}_2$ are given. We observe that both of the on-shell decays $\tilde{N}_2 \to \tilde{N}_1 h$ and $\tilde{N}_2 \to \tilde{N}_1 Z$ are available for this state when $\alpha \lesssim 0.7$, with the Higgs mode peaking around $\alpha \simeq 0.6$ before becoming kinematically inaccessible. This changeover is reflected in the R_i values for the leptonic counting signature and the B-jet counting signature of List C, as shown in the right panel of Figure 3.11. Note that the light stop in benchmark model B makes this a very B-jet rich point. In fact, this particular counting signature is one of the most effective observables in List C along the alpha-line for this point.

Input Parameter Range	Variation
400 GeV $\geq M_3 \geq$ 800 GeV	5 steps
400 GeV $\geq \mu \geq$ 1000 GeV	5 steps
300 GeV $\geq (m_{\tilde{e}_{L,R}}, m_{\tilde{\tau}_{L,R}}) \geq$ 700 GeV	5 steps
500 GeV $\geq (m_{\tilde{Q}_L}, m_{\tilde{q}_L}, m_{\tilde{t}_{L,R}}, m_{\tilde{b}L,R}) \geq$ 1000 GeV	5 steps
$\tan\beta = 10$	Fixed
$m_A = 1000$ GeV	Fixed
A_τ, A_t, A_b, A_e, A_u, $A_d = 0$	Fixed

Table 3.9: MSSM soft parameters ranges and variation steps used to generate controlled sample. These values are given at the electroweak scale. For each choice of MSSM input, the gaugino unification parameter α was varied in four steps, from $\alpha = 0$ to $\alpha = 1.0$

3.4.2 Analysis of a Large Set of Model Variations

We next examine the efficacy of our method by testing it on a large sample of varying model points. We will do this in two steps: first on a controlled sample of models and subsequently on a random collection of model lines. Ranges for the MSSM input parameters and variation steps used for our controlled sample are given in Table 3.9. Only M_3, $m_{\tilde{l}}$, $m_{\tilde{q}}$, and μ were allowed to vary across 5 uniform steps. All other soft parameters were held constant. The gaugino universality parameter α was also varied in 4 steps from $\alpha = 0$, to 0.33, 0.66, and 1.0. These choices discretize the range of parameter space into 2500 individual model points. Note that the parameters of Table 3.9 are given at the low-energy electroweak scale. We emphasize the fact that in this first step we have chosen to sample the parameter space on a discrete grid rather than sampling it randomly. While a truly random sampling is necessary for ultimately testing our method, we here wish to study the performance of our signature sets as key parameters are varied. Our discrete grid is designed to keep the overall supersymmetric production rate roughly fixed, allowing for a more straightforward comparison of $L_{\min}$ values. This course sampling also allows a large degree of model variation while keeping computation time to a minimum. Our analysis of a random collection of models will appear at the end of this subsection.

Largest Production Channel

Mode	$\alpha = 0$	$\alpha = 0.33$	$\alpha = 0.66$	$\alpha = 1.0$
$gg \to \tilde{g}\tilde{g}$	44.6%	45.2%	42.9%	44.8%
$fg \to \tilde{q}_R\tilde{g}$	31.1%	30.2%	33.1%	35.7%
$fg \to \tilde{q}_L\tilde{g}$	24.3%	25.5%	23.9%	19.4%

Second Largest Production Channel

Mode	$\alpha = 0$	$\alpha = 0.33$	$\alpha = 0.66$	$\alpha = 1.0$
$gg \to \tilde{g}\tilde{g}$	2.7%	2.1%	2.8%	1.4%
$fg \to \tilde{q}_R\tilde{g}$	42.0%	48.8%	47.5%	45.2%
$fg \to \tilde{q}_L\tilde{g}$	42.0%	47.1%	49.6%	53.3%
$f_i f_j \to \tilde{\chi}_2^0\tilde{\chi}_1^\pm$	13.2%	1.9%	-	-

Table 3.10: Dominant production modes across all model variations. At a given α choice, the upper table indicates the percentage of models for which these modes had the largest cross section, while the lower table indicates the percentage for which the modes had the second-largest cross-section. All models exhibit predominantly gluino pair production, or gluino-quark associated production. A small fraction of $\alpha = 0$ models exhibit neutralino-chargino pair production. This mode 'switches off' as α is increased from zero, as the gaugino masses increase.

Simulated data for the model points was generated with the following procedure. For each model, the `SuSpect` partner code `SusyHIT` [105] was used to compute the low-scale spectrum from the input MSSM soft terms. No renormalization group evolution was necessary because the input parameters were given at the electroweak scale. As before `PYTHIA` + `PGS4` was used to simulate the detector response for each point. A check was performed to ensure that each model point had a neutralino LSP, and also that each $\alpha \geq 0$ model point simulated had an associated $\alpha = 0$ counterpart, so that the minimum luminosity required to distinguish between the two models, $L_{\min}$, could be computed. Only models satisfying these requirements were retained for analysis. Exactly 1449 model pairs ($\alpha = 0$ and $\alpha \neq 0$) were retained after applying this selection procedure.

Table 3.10 gives the dominant production modes across the entire set of model variations. The upper table indicates the mode and percentage of models, for a given α choice, that occur with the largest cross-section. The lower table gives the same information for the modes that occur with the second-largest cross-section.

The majority of models exhibit squark-gluino associated production, or gluino pair production as the dominant production mechanism. Approximately 13% of $\alpha = 0$ models, and about 2% of $\alpha = 0.33$ models have neutralino-chargino production as the second most dominant mode.

The particle decay behavior varies throughout the range of model simulations. However, gluino decays are largely insensitive to changes in α. For the case $\alpha = 0$, approximately 68% of models have $\tilde{g} \rightarrow \tilde{\chi}_1^{\pm} + \bar{q}q'$ as the primary decay channel (the channel having the largest branching fraction), while 31% of models have instead $\tilde{g} \rightarrow \tilde{b}_1 + b$ as the primary channel. The $\alpha = 0.33$ and 0.66 models exhibit similar ratios. The $\alpha = 1.0$ models show a slight variation, with the distribution shifting to 70% and ∼30% respectively. For all α values, approximately 68% of model variations also exhibit $\tilde{g} \rightarrow \tilde{\chi}_1^{\pm} + \bar{q}q'$ as the dominant secondary channel (having the second-largest branching fraction), while 30% have decays to an on-shell second-generation squark + quark as the secondary channel.

The first- and second-generation squark decays are equally insensitive to variations in α. For all α, approximately 50% of models indicate $\tilde{q}_L \rightarrow \tilde{g}+q$ is the primary decay channel, while the other 50% have $\tilde{\chi}_1^{\pm} + q'$ as the primary channel. This is also the dominant secondary channel in 48% of the models. Another 40% have $\tilde{\chi}_2^0 + q$ as the secondary channel. The $\tilde{q}_R$ are slightly different, with approximately 62% of models indicating $\tilde{q}_R \rightarrow \tilde{g} + q$ as the primary channel, and another 37% $\tilde{q}_R \rightarrow \tilde{\chi}_1^0 + q$. This is also the dominant secondary channel in 63% of models, with $\tilde{\chi}_2^0 + q$ the secondary channel for another 32%, and the remaining 5% having $\rightarrow \tilde{g} + q$.

Due to dependence on the gaugino mass parameters, the chargino decays are significantly more sensitive to variations of α. For the $\alpha = 0$ case, approximately 74% of models have $\tilde{\chi}_1^{\pm} \rightarrow W^{\pm} + \tilde{\chi}_1^0$ as the primary decay channel. Another 25%

	$\alpha = 0.33$			$\alpha = 0.66$			$\alpha = 1.0$		
$L_{\min}$ value	List A	List B	List C	List A	List B	List C	List A	List B	List C
$\leq 1\,\text{fb}^{-1}$	115	206	282	271	417	474	410	475	484
$\leq 2\,\text{fb}^{-1}$	35	93	86	52	36	10	38	9	0
$\leq 4\,\text{fb}^{-1}$	49	57	42	52	35	2	24	0	0
$\leq 10\,\text{fb}^{-1}$	42	73	50	48	8	0	10	0	0
$\leq 100\,\text{fb}^{-1}$	130	40	8	72	0	0	2	0	0
$> 100\,\text{fb}^{-1}$	98	0	0	1	0	0	0	0	0

Table 3.11: Minimum integrated luminosity $L_{\min}$ to separate $\alpha = 0$ from $\alpha \neq 0$ in controlled model sample. Distribution of $L_{\min}$ values for the three signature sets of Tables 3.5, 3.6 and 3.7. In each case we are comparing the indicated value of α with the case $\alpha = 0$ for the same set of background model parameters.

have $\tilde{\chi}^{\pm} \to \tilde{\chi}_1^0 + \bar{q} + q'$ as the primary channel (here the quarks are from the first or second generation), while the remaining 1% have instead $\tilde{\chi}^{\pm} \to \tilde{\chi}_1^0 + \tau + \nu_\tau$. As α increases these three decay channels persist, however their distribution across each set of models begins to change, and additional channels begin to appear. For the $\alpha = 0.33$ case, the above channels occur in 65%, 31%, and 1% of models, respectively. However, now the remaining 3% of models have $\tilde{\chi}_1^{\pm} \to \tilde{\tau}_1^{\pm} + \nu_\tau$ as the primary channel. The $\tilde{\chi}^{\pm} \to \tilde{\chi}_1^0 + \bar{q} + q'$ channel is the dominant secondary channel for all α variations.

The $\tilde{\chi}_2^0$ decay behavior is similarly diverse. For case $\alpha = 0$, approximately 39% of models have $\tilde{\chi}_2^0 \to \tilde{\chi}_1^0 + q\bar{q}$ as the primary decay channel, while 23% have $\tilde{\chi}_2^0 \to \tilde{\chi}_1^0 + Z^0$, 28% have $\tilde{\chi}_2^0 \to \tilde{\chi}_1^0 + h^0$, and another 10% have $\tilde{\chi}_2^0 \to \tilde{\chi}_1^0 + \tau^+\tau^-$ as the primary channel. This distribution shifts slightly for $\alpha = 0.33$ to 40%, 26%, 18%, and 13%, respectively. Here, another 3% of models have $\tilde{\chi}_2^0 \to \tilde{\tau}_1^{\pm} + \tau$ as the dominant channel. For $\alpha = 0.66$ it is shifted further to 46%, 18%, 15%, 15%, where here the remaining 3.4% of models now having $\tilde{\chi}_2^0 \to \tilde{\nu}_{eL} + \nu_e$ as the primary channel. For $\alpha = 1.0$, the Z^0 and h^0 decays occur less frequently, with only 8% and 5% of models having these as the primary channel. The $\tilde{\chi}_1^0 + q\bar{q}$, $\tilde{\chi}_1^0 + \tau^+\tau^-$, and $\tilde{\tau}_1^{\pm} + \tau$ channels appear with the largest branching fraction in 56%, 19%, and 9% of models, respectively.

As with the benchmark models, we analyze the 1449 model pairs using the three

signature sets given in Tables 3.5, 3.6 and 3.7. Due to the large number of model points we present results statistically in the form of the observed distribution of $L_{\min}$. Table 3.11 shows the minimum luminosity required to distinguish between models with $\alpha = 0$ and those with $\alpha \neq 0$ when using, respectively, signature Lists A, B and C. Considering the case of $\alpha = 0.33$ first, signature List A is able to successfully resolve a large number of model pairs with fairly low luminosity. However, only 241 out of the 469 model variations analyzed for this value of α can be resolved with less than 10 fb^{-1}. Signature Lists B and C exhibit significantly stronger resolving power, with List B able to distinguish 429 variations, and List C 461 out of the 469 total model variations considered. Both Lists B and C allow the majority of model variations to be distinguished with ≤ 4 fb^{-1} integrated luminosity, however List C exhibits the best performance overall, as it is able to distinguish the models with a consistently lower luminosity requirement. For the $\alpha = 0.66$ models, all three signature sets allow the majority of model points to be distinguished from $\alpha = 0$ with less than 4 fb^{-1} integrated luminosity. Only List A was unable to resolve all model variations with less than 10 fb^{-1}, as 73 out of 496 models required higher luminosity. Signature List C exhibits the best performance, allowing nearly all model variations to be resolved with ≤ 2 fb^{-1}. The $\alpha = 1.0$ models are sufficiently different from the $\alpha = 0$ case that all three of the signature sets are able to distinguish the two cases with exceptionally low luminosity. Signature List C again exhibits the best performance, allowing all models to be distinguished with less than 1 fb^{-1} of data.

We can understand these results by examining the individual $(R_{AB})_i$ response of each signature. From equation (3.36), the minimum luminosity required to distinguish two models, A and B, is inversely proportional to R_{AB}, which is the sum of the individual $(R_{AB})_i$ values of each signature. Because $(R_{AB})_i$ reflects the sensitivity of

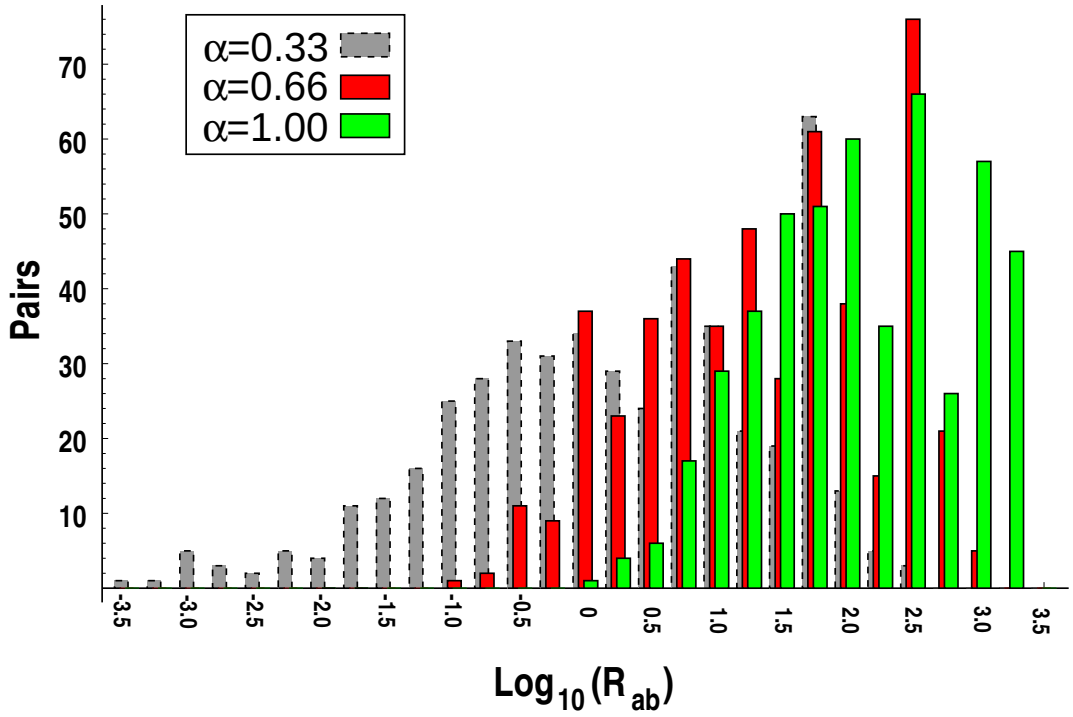

Figure 3.12: Distribution of (R_{AB}) values for signature List A. The distribution of R_{AB} values for the single signature of List A is given for the parameter sets $\alpha = 0.33$, $\alpha = 0.66$, and $\alpha = 1.0$. In each case we are comparing the indicated value of α with the case $\alpha = 0$ for the same set of background model parameters. Note that larger values of R_{AB} imply lower values of $L_{\min}$.

the i-th signature to changes between models A and B (a larger $(R_{AB})_i$ value being more sensitive), signatures that have high sensitivity to physical changes associated with α provide a greater contribution to the total R_{AB}, and thus reduce the $L_{\min}$ requirement.

The distribution of R_{AB} values for the single signature of List A is shown in Figure 3.12. For the $\alpha = 0.33$ case the distribution is localized to relatively low values of R_{AB}. For the $\alpha = 0.66$ and $\alpha = 1.0$ cases the distribution begins to spread out, with many models having significantly larger R_{AB} values. This indicates the signature is becoming increasingly more sensitive to the differences brought on by changes in α as this parameter is increased. However, with only a single signature it is not possible to guarantee that it will be as effective for other models as it is in this

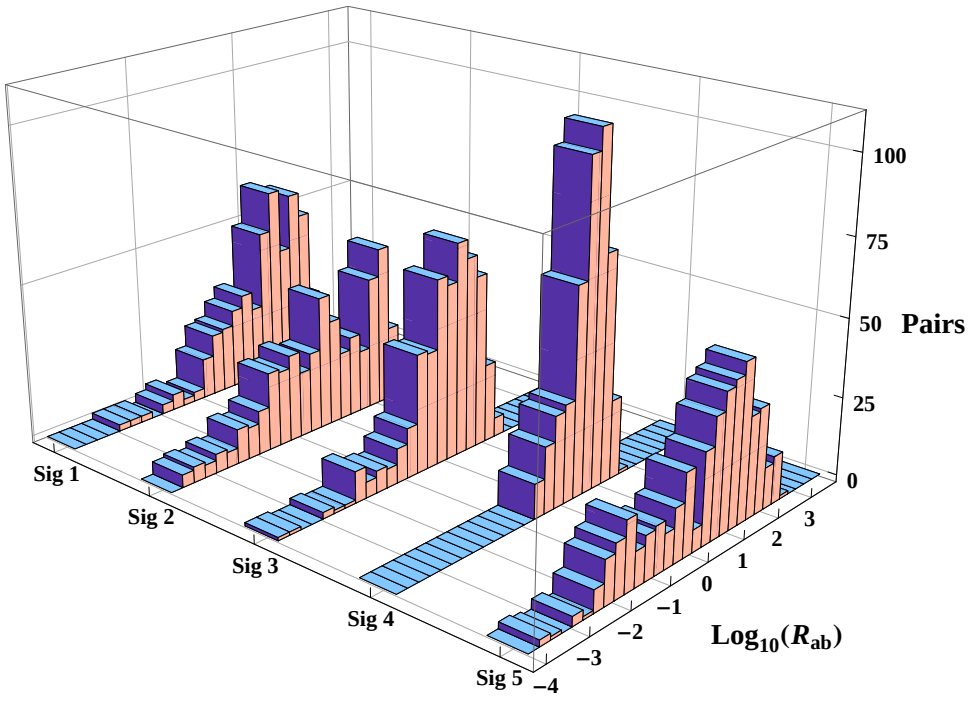

Figure 3.13: Distribution of $(R_{AB})_i$ values for signature List B [$\alpha = 0.33$ versus $\alpha = 0$]. The distribution of $(R_{AB})_i$ values for the five signatures of List B is given for the case of comparing $\alpha = 0$ with $\alpha = 0.33$. For the definition of the five signatures, see Table 3.6.

example. In order for this approach to work across a broad range of potential physics scenarios it is advantageous to adopt a combination of signatures, where each may be sensitive to one or more aspects of a particular class of models.

Figures 3.13 and 3.14 show the distributions of $(R_{AB})_i$ obtained for the five signatures of signature List B. Each figure represents five histograms where the variable being considered is $\log_{10}[(R_{ab})_i]$, with the comparison being between $\alpha = 0$ and $\alpha = 0.33$ in Figure 3.13 and between $\alpha = 0$ and $\alpha = 1$ in Figure 3.14. In a similar fashion to the single signature of List A, the distributions are in general clustered at low $(R_{AB})_i$ for $\alpha = 0.33$, and begin to spread out considerably, taking on much larger values as α increases. Comparing the individual distributions to those in the single signature of List A, the overall spread of values is not significantly different. However, recall that R_{AB} is the sum of the individual $(R_{AB})_i$ values. Therefore we

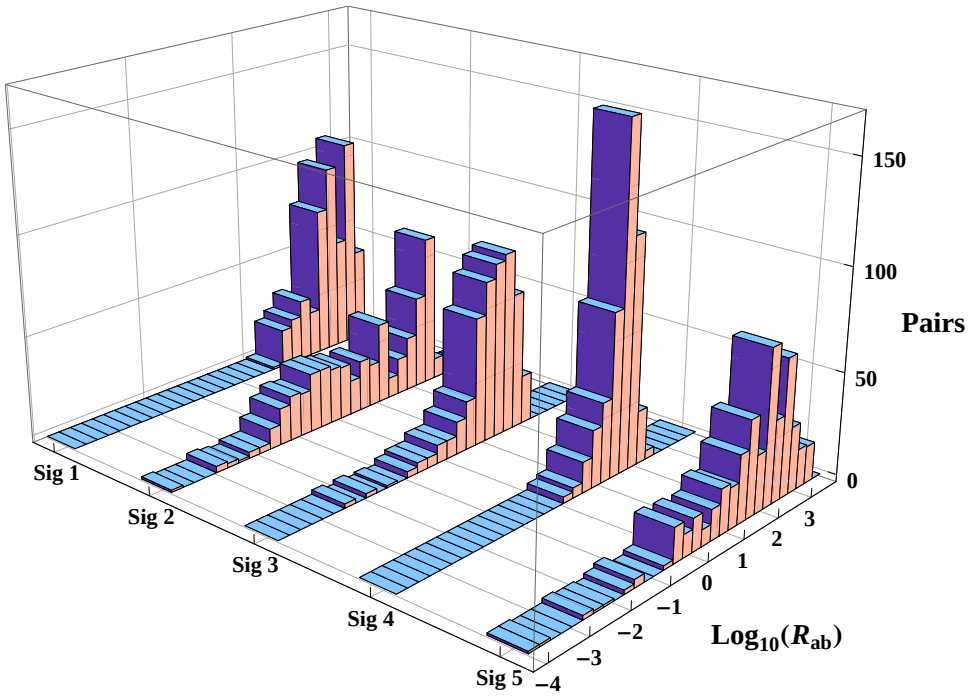

Figure 3.14: Distribution of $(R_{AB})_i$ values for signature List B [$\alpha = 1$ versus $\alpha = 0$]. The distribution of $(R_{AB})_i$ values for the five signatures of List B is given for the case of comparing $\alpha = 0$ with $\alpha = 1$. For the definition of the five signatures, see Table 3.6.

gain a significant enhancement by simply including additional signatures. A similar effect occurs with the larger set of signatures in List C. As we saw in Section 3.2, however, there is ultimately a point of negative returns and a maximum efficacy is obtained.

Thus far we have presented the results of our approach in terms of the minimum integrated luminosity required to resolve two model classes ($\alpha = 0$ and $\alpha \neq 0$) using our set of optimized signatures. To understand why this approach works, it is useful to examine the signature results themselves. Figures 3.15 and 3.16 show examples of two-dimensional slices of the signature space "footprint" for our large set of model variations. In these figures the results have been normalized to 5 fb^{-1} of data.

Figure 3.15 compares the count rates for the third and fourth signatures of List B for the case $\alpha = 0$ versus $\alpha = 0.66$ (left panel) and $\alpha = 1$ (right panel). Figure 3.16

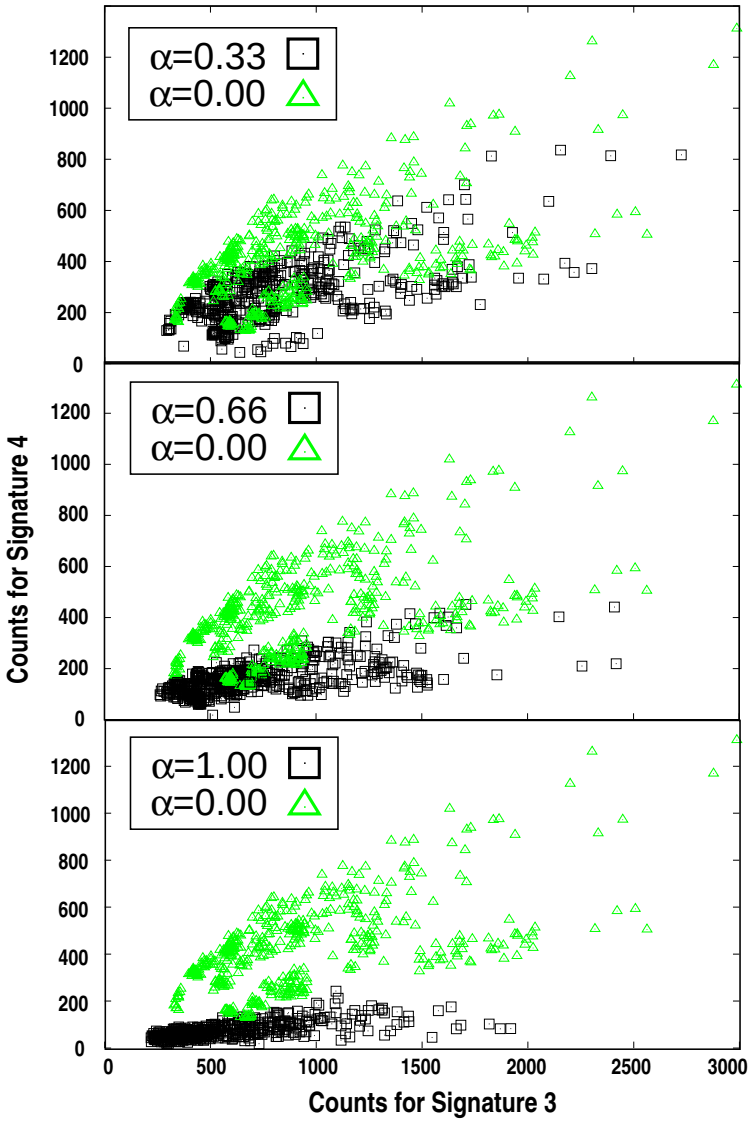

Figure 3.15: Footprint-style plot for a pair of signatures from List B. Total counts for signature #3 versus signature #4 of List B is given for the case $\alpha = 0$ (green triangles) $\alpha \neq 0$ (black squares). The cases shown are for $\alpha = 0$ versus $\alpha = 0.33$ (top panel), $\alpha = 0.66$ (middle panel) and $\alpha = 1$ (bottom panel). The axes measure the number of events for which the kinematic quantity was in the range given in Table 3.6. Larger values of the non-universality parameter α correspond to a greater degree of separation between the two model "footprints."

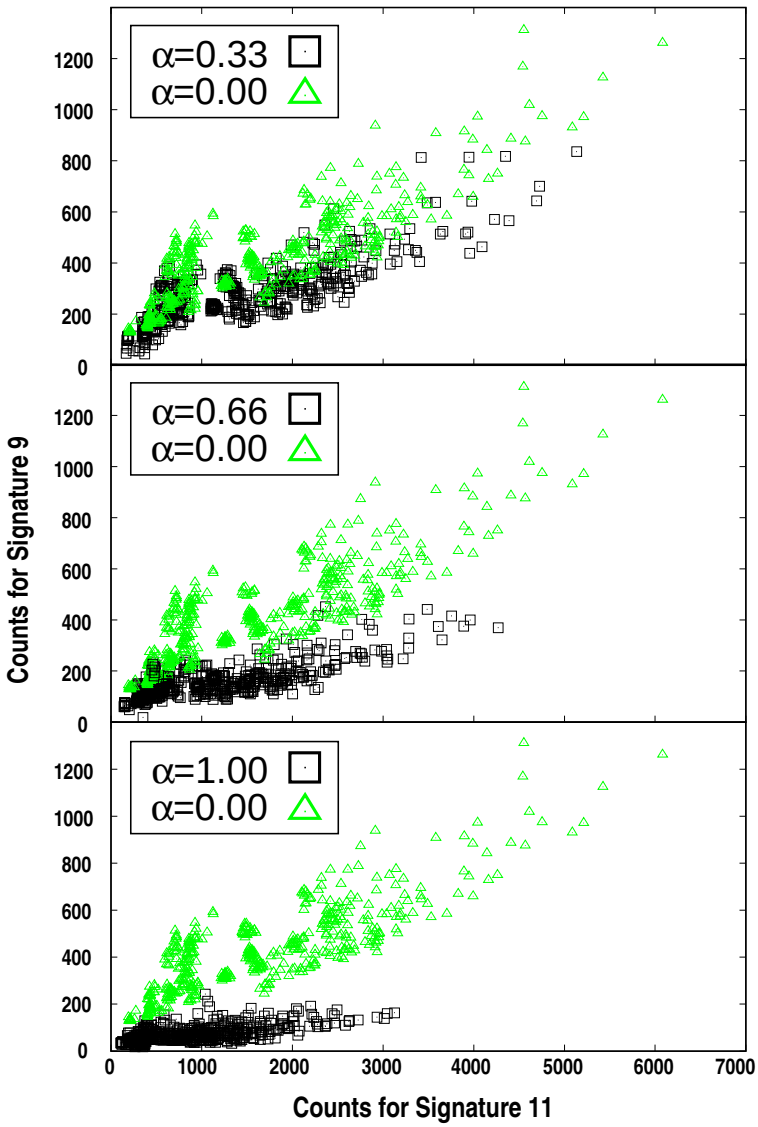

Figure 3.16: Footprint-style plot for a pair of signatures from List C. Total counts for signature #11 versus signature #13 of List C is given for the case $\alpha = 0$ (green triangles) $\alpha \neq 0$ (black squares). The cases shown are for $\alpha = 0$ versus $\alpha = 0.33$ (top panel), $\alpha = 0.66$ (middle panel) and $\alpha = 1$ (bottom panel). The axes measure the number of events for which the kinematic quantity was in the range given in Table 3.7. Larger values of the non-universality parameter α correspond to a greater degree of separation between the two model "footprints."

compares the count rates for signatures #11 and #13 of List C for the case $\alpha = 0$ versus $\alpha = 0.66$ (left panel) and $\alpha = 1$ (right panel). In this case the two signatures are both taken from the set of events containing at least one lepton and five or more jets (see Table 3.7). We have chosen this pair for the dramatic separation that can be achieved, though similar results can be obtained with other pairs of signatures.

The power of our inclusive signature list approach lies in the choice of signatures and their ability to remain highly sensitive to changes in the physical behavior of each model. This feature is reflected qualitatively in the visual clustering of the data points, which become progressively more distinct as the parameter α is increased. As the regions separate it becomes increasingly less likely that a model from one class can be confused with a model from the other class, even when considering statistical fluctuations. In our approach this manifests itself when one computes R_{AB}, which reflects the "distance" in signature space between the two models under comparison, and which becomes large when the models are sufficiently different from one another.

The idea of using repeated pairings of targeted observables in order to separate model classes was studied in previous "footprint-style" analyses [106, 107, 108]. If we consider the universal gaugino mass scenario (*i.e.* $\alpha = 0$) as a "model," and the case of non-universal gaugino masses as a separate model, then a set of signatures will be truly targeted at this particular model feature if the set of all such two-dimensional planes implies complete separation between the models. With this in mind it is interesting to examine distinguishability between the two values of α from a somewhat different perspective. Adopting the approach of [108] we can ask how many degeneracies exist between the two classes of models, where by degeneracy we mean two models that exist at different points in the microscopic parameter space, but occupy the same point in signature space (up to statistical fluctuations).

If it is possible, through application of one or more signatures, to ensure that no degeneracies exist we can claim to that it is possible to completely discriminate between the two classes.

As an example of how this idea can be applied, we can consider the analysis performed in [108]. Let one particular value of the parameter α (such as $\alpha = 0$) be "model A" and let some other value of the parameter α be "model B." Choose any pair of signatures in one of the signature lists. From our controlled sample we can choose an individual case $B_j \in B$ and compute the quantity $(\Delta S_{A_i B_j})^2$ between that particular point and all the points $A_i \in A$ for this pair of signatures. If the value for all such $(\Delta S_{A_i B_j})^2$ is always greater than the two-signature threshold given by $\gamma_2(0.95)$ in Table 3.2 we will claim the point B_j has been separated from the entire footprint of model A. We can then repeat this exercise over all cases of model B. The number of cases of model B that have *not* been separated from the entire footprint of model A we will denote as N_{BA}. This is a type of degeneracy count for model B with respect to model A. Clearly the process can be performed for model A with respect to model B, producing a degeneracy count N_{AB}. In general we expect these two numbers to be roughly equivalent in magnitude, but not necessarily precisely equal.

If either N_{AB} or N_{BA} are non-vanishing then the two footprints are not yet disjoint in the multi-dimensional signature space. We can then choose any other pair of signatures and repeat the procedure, this time restricting A_i and B_j to run only over the degenerate cases. If we have chosen a good set of signatures the quantities N_{AB} and N_{BA} should rapidly converge to zero as the algorithm is successively applied. The results of performing this exercise on the controlled model sample generated by the parameters of Table 3.9 is shown in Figure 3.17. In the left panel we show

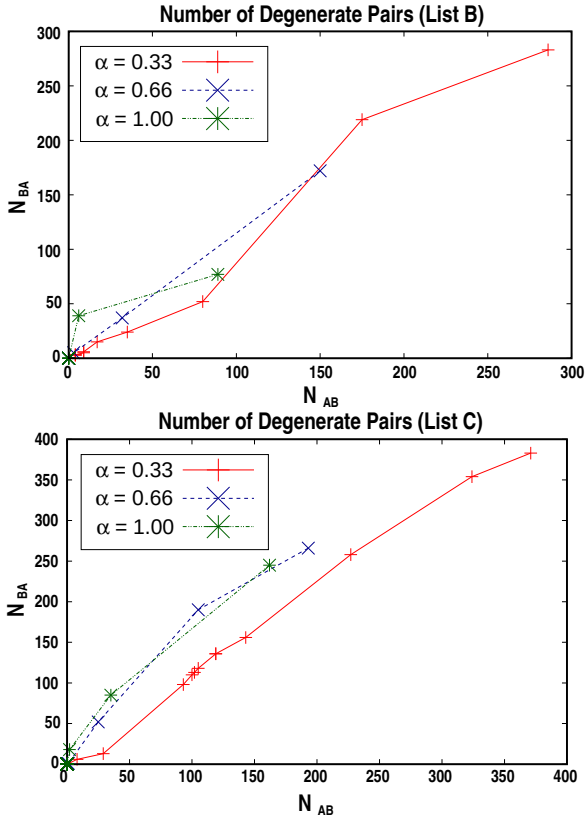

Figure 3.17: Degeneracy counts for List B (left panel) and List C (right panel). The relative degeneracy counts N_{AB} and N_{BA} that result from successive application of pairs of signatures from List B and List C are plotted for our controlled model sample. In each case model A is the case with $\alpha = 0$ while model B is the case with the indicated value of $\alpha \neq 0$. Once all model pairs have been applied the total degeneracy count vanishes for both lists and for all values of $\alpha \neq 0$.

the successive values of N_{AB} and N_{BA} as pairs of signatures from List B are used to compute the separability parameter $(\Delta S_{AB})^2$, while the right panel uses pairs of signatures from List C. In both cases "model A" represents the set of models with $\alpha = 0$, while "model B" represents the case with the indicated value of $\alpha = 0.33$, 0.66 and 1.0. For all three values of the parameter α the lists do an excellent job of converging towards $N_{AB} = N_{BA} = 0$ after only a few pairings are considered. This suggests that the signature lists of Tables 3.6 and 3.7 should be able to reveal the departure of the gaugino soft masses from the universal ratios on a truly *general* supersymmetric model with a high degree of reliability and in a small amount of

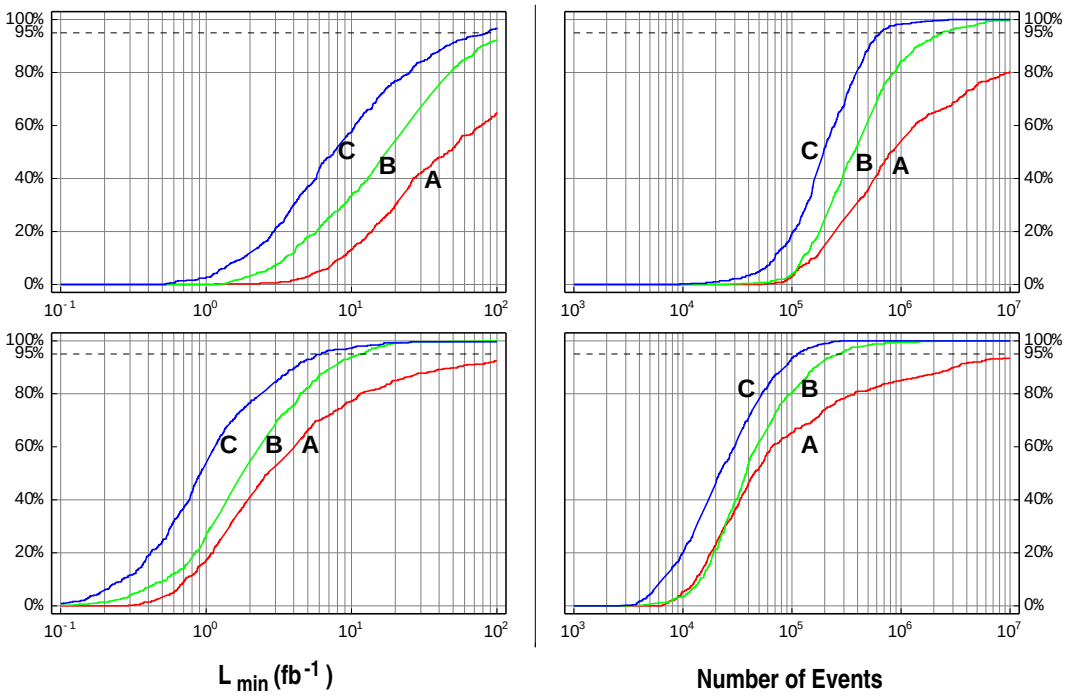

Figure 3.18: Efficiencies of the three signature lists. The ability of the three signature lists to separate the case $\alpha = 0.1$ from $\alpha = 0$ is indicated in the top pair of plots and the simpler case $\alpha = 0.3$ from $\alpha = 0$ in the bottom pair of plots. On the left, the percentage of cases that could be distinguished using each of the three signature lists of Tables 3.5, 3.6 and 3.7 is given as a function of integrated luminosity in units of fb^{-1}. On the right the same percentage is shown as a function of the number of supersymmetric events. The 95% separability threshold is indicated by the dashed horizontal line.

integrated luminosity.

To honestly confirm this hypothesis we must generate a more random set of models. After all, the signature lists of Tables 3.5, 3.6 and 3.7 were constructed precisely with the sorts of models of our controlled sample in mind. But as we saw in Section 3.4.1, models such as benchmark model A can prove more challenging for our analysis algorithm. To allow for the possibility of more perverse cases than those of our controlled sample, an additional set of 500 models were generated with six points on the α-lines ranging from 0 to 0.5. In this case a 16-dimensional parameter space defined by the quantities in (3.18) was considered. Specifically, slepton and squark masses were allowed to vary in the range 300 GeV to 1200 GeV with the masses of

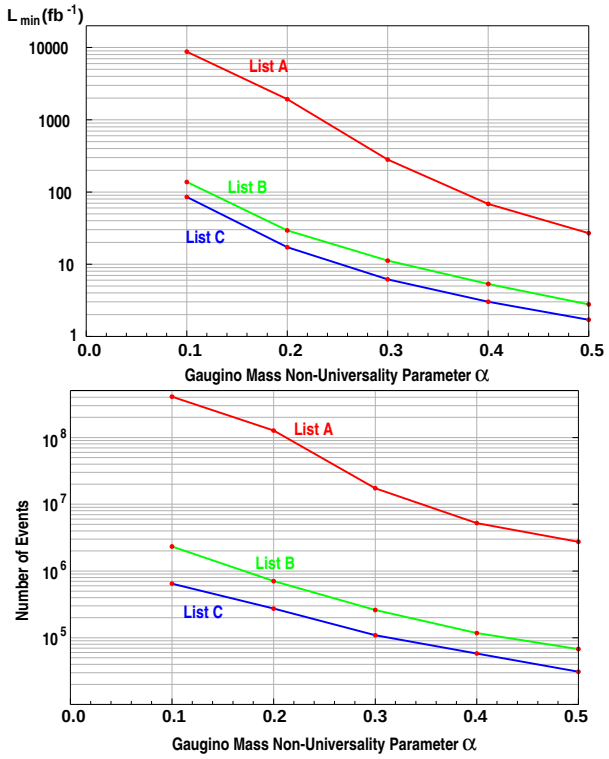

Figure 3.19: $L_{\min}$ and $N_{\min}$ required to detect $\alpha \neq 0$ for 95% of the random models.

the first and second generation scalars kept equal. The gaugino mass scale given by M_3 and the μ-parameter were also allowed to vary in this range. The pseudoscalar Higgs mass m_A was fixed to be 850 GeV and the value of $\tan\beta$ was allowed to vary from 2 to 50. If all points along the α-line satisfied all experimental constraints on the superpartner mass spectrum, then 100,000 events were generated for each of the six points along the α-line in the manner described in Section 3.2. Using this data the value of $L_{\min}$ was computing using (3.37) and (3.38) for each of our three signature sets.

The results of this analysis are given in Figures 3.18 and 3.19. Figure 3.18 considers the ability of our signature lists to separate the case $\alpha = 0.1$ from $\alpha = 0$ (top pair of plots) and the simpler case $\alpha = 0.3$ from $\alpha = 0$ (bottom pair of plots). On the left, the percentage of cases that could be distinguished using each of the three

signature lists of Tables 3.5, 3.6 and 3.7 is given as a function of integrated luminosity in units of fb^{-1}. Since the random model sample includes examples with very different superpartner mass scales, the overall supersymmetric production cross-section varies much more across this sample than in the controlled model sample described above. We therefore take this into account by plotting the same percentage in terms of the number of supersymmetric events on the right side of Figure 3.18. The 95% separability threshold is indicated by the dashed horizontal line. Even using our best set of signatures (List C) it will require nearly 100 fb^{-1} to be able to detect non-universality at the level of $\alpha \simeq 0.1$ for an arbitrary supersymmetric model. Yet for the vast majority of models the departure from universality should become apparent after just 10-20 fb^{-1}. Departures from universality at the level of $\alpha \simeq 0.3$ should be apparent using this method for most supersymmetric models after just a few fb^{-1}. In Figure 3.19 the integrated luminosity (or number of supersymmetric events) needed to detect $\alpha \neq 0$ for 95% of our random models is given as a function of the five non-vanishing α values simulated.

3.5 Summary

If supersymmetry is discovered at the LHC the high energy community will be blessed with a large number of new superpartners whose masses and interactions will need to be measured. At the same time the community will be challenged by a large model space with many Lagrangian parameters which cannot themselves be directly measured experimentally. Undoubtedly performing global fits of the many observables to the parameter space of certain privileged and well-defined benchmark models will be of great help in making sense of this embarrassment of richness. But recent work suggests that unless these models are determined by very few parameters

it is likely (if not perhaps inevitable) that multiple points in the parameter space will fit the data well. It then becomes an interesting question to ask whether it is possible to fit to certain model *characteristics* rather than to any particular model itself.

In our opinion one of the most important such characteristic is the pattern of soft supersymmetry-breaking gaugino masses. No other property of the low-energy soft Lagrangian is more easily linked to underlying high-scale physics, particularly if that high-scale physics is of a string-theoretic origin. Only the related issue of the wavefunction of the LSP is of more importance to low-energy physics and cosmology. We are thus interested in asking whether we can identify the presence of non-universalities in the gaugino sector independent of all other properties of the superpartner spectrum. The manner by which any such undertaking can be tackled is by no means clear – though neither is it clear that such an undertaking is inherently impossible. In the present work we have decided to begin this process with a simple parametrization of the gaugino masses determined by a single parameter which can be thought of as the ratio of bulk gravity and anomaly contributions to gaugino masses. We developed model "lines" in the spirit of previous benchmark studies such as the Snowmass Points & Slopes in which only the single non-universality parameter is varied. By understanding how the observable physics at the LHC is affected by this parameter – and then repeating the analysis many times with the other supersymmetric parameters varied – we can learn which LHC signatures are most directly "targeted" at this important underlying characteristic.

Our procedure depends on certain analytic results that improve on the methods first introduced concretely by Arkani-Hamed et al. These analytic results in turn depend on the assumption that the signatures considered have fluctuations which

are largely uncorrelated with one another. This severely limits the type of signature ensembles one might construct. Yet this restriction does not imply a loss of resolving power, as the "optimal" signature list is rarely the largest possible list one can imagine. Our analysis has suggested two signatures ensembles which perform remarkable well at the task of measuring the value of the non-universality parameter we introduce. Broadly speaking, we find that a non-universality at the 10% level can be measured with 10-20 fb^{-1} of integrated luminosity over approximately 80% of the supersymmetric parameter space relevant for LHC observables. If we are interested in measurements at only the 30% level these numbers change to 5-10 fb^{-1} over approximately 95% of the relevant parameter space.

This is remarkable progress, but the task we set out for ourselves is admittedly still somewhat artificial. There are two independent mass ratios that can be constructed from the three soft supersymmetry breaking gaugino masses – our parametrization is therefore not fully general. It would be of great interest to study more general departures from non-universality to see if the optimal signature lists change substantially. Of greater import is the need to perform a Monte Carlo simulation in order to compare a candidate model to the "data" at the LHC. To perform such a comparison we must assume knowledge of all input parameters *apart* from the one we are attempting to measure. While this is a common practice in benchmark studies at colliders, it is far from the reality that theorists and experimentalists will encounter in the early stages of the LHC era. Our study demonstrated the efficacy of certain targeted observables in extracting the non-universality parameter α while keeping all other parameters fixed for the two models. This is quite a strong assumption and future work should relax this constraint. In other words, one would like to distinguish between two models (with different values of α) even if the other parameters

for the two models are not the same. There are many directions by which this may be pursued. For example, in the current analysis we have not allowed ourselves any knowledge of the mass spectrum, though analysis of kinematic end-points will certainly provide some information in this regard early on in LHC data-taking. In addition, techniques such as the use of on-shell effective theories [61] might provide sufficient information about the dominant production and decay modes for new mass eigenstates to allow an approximation to our analysis to be performed before the full mass spectrum is reconstructed. We hope to pursue both avenues for introducing greater realism in future work.

CHAPTER IV

Indirect Detection of Non-Thermal Neutralino Dark Matter

While astrophysical measurements have precisely determined the amount of dark matter in our universe, we do not yet know its identity. At present one could imagine that the dark matter is a weakly interacting massive particle (WIMP), an axion, or something more exotic. This situation should change, perhaps soon. If the dark matter is indeed a WIMP, evidence for it could be found both at the Large Hadron Collider (LHC) and a host of dark matter detection experiments, both direct and indirect.

In this chapter, we depart from the LHC and explore the implications for SUSY at astrophysical experiments that may be sensitive to annihilations of dark matter in the galaxy. We will assume that the dark matter is a WIMP, in particular the lightest supersymmetric particle (LSP). The identity of the LSP depends on the details of supersymmetry breaking. Determining its identity will be a necessary step towards understanding the cosmological history of our universe, and an important clue towards the determination of the underlying theory. As discussed in Chapter I a phenomenologically attractive candidate is the lightest neutralino. We concentrate on a case that is both physically well-motivated and potentially gives large signals for dark matter indirect detection: a non-thermally produced LSP with large anni-

hilation cross section. This scenario does not require additional anomalously large astrophysical "boost factors" to produce interesting signals.

By now, a large literature on the indirect detection of dark matter exists. For reviews, see [109, 110]. We will place particular emphasis on a dark matter interpretation of positrons, for earlier work on this subject see, e.g., [111, 112, 113, 114].

For the LHC to provide complementary data on the dark matter[115, 116], it must be kinematically accessible. Often, the dark matter is most efficiently searched for in the cascade decays of colored particles. However, there can be a large gap between the dark matter mass and the lightest colored particle. In models with gaugino mass unification, there is roughly a factor of seven between the WIMP candidate mass and the gluino mass. In anomaly mediated models of supersymmetry breaking, the ratio is a factor of nine; in other models with non-universal gaugino masses, it can be a factor of a few. Thus, if the gluino is to be produced copiously (say with a mass less than 2 TeV), the dark matter should not be too heavy. In this chapter, we will focus on a light mass region where the LSP is a wino with a mass of a few hundred GeV. This discussion is based on the results found in [16].

4.1 Thermal vs. Non-Thermal Production

Often, SUSY dark matter candidates are assumed to be produced from the primordial thermal plasma in the early stages of the universe (see e.g. [109] for a review). Under this assumption, the relic density of the LSP depends inversely on the annihilation cross section. For a neutralino, χ, one finds [117, 118]:

$$\Omega_\chi h^2 \approx 0.1 \left(\frac{3 \times 10^{-26} \mathrm{cm}^3 \mathrm{s}^{-1}}{\langle \sigma_A v \rangle} \right) \tag{4.1}$$

For the case of a light neutralino LSP (a few hundred GeV or less), this typically restricts the neutralino to have a substantial bino component as pure wino and

Higgsino states (co)-annihilate very effectively to weak gauge bosons. But precisely because of the smaller annihilation cross section, the annihilation signals from bino-like dark matter can be disappointingly small unless one appeals to large "boost factors." This issue is further exacerbated by the fact that bino annihilations are p-wave suppressed in the early universe, and are thus suppressed by powers of the final state masses today. If, as is often the case, the final state is b-quarks, the annihilation rate in our galaxy can be very small.

Models with gaugino mass unification often do typically give rise to a bino LSP, with its associated small annihilation cross section. One is then challenged to reduce the relic density to the observed value. However, if one does not assume a simple unification of gaugino masses at the high scale, other possibilities arise, well-motivated by top-down models of supersymmetry breaking. One attractive possibility is a wino LSP. This naturally occurs in theories where anomaly mediation gives the dominant contribution to the gaugino masses[119]. It also occurs in string compactifications, see, e.g. [36]. This type of dark matter can also occur in the simplest models of split-supersymmetry [120, 121], where the gauginos get anomaly mediated masses (with attendant loop suppression), but scalars receive large masses, suppressed only by the Planck scale.

A light wino has a large annihilation cross section, which is good for indirect detection, but also implies a small thermal relic abundance. The solution to recovering the correct relic abundance comes from non-thermal production. Often, the very same models that predict a wino LSP also provide mechanisms by which the LSP is produced non-thermally. If particles decay into the wino below its freeze-out temperature, this can provide the correct relic abundance[122]. Excellent candidates for the decaying particle include gravitinos and weakly coupled moduli [123, 125, 124]. Non-

thermal production of dark matter leads to WIMPs with larger cross sections, since the standard thermal relic abundance calculation no longer applies. Since the flux of anti-particles coming from dark matter annihilations depends linearly on the cross section, this implies that non-thermal production of dark matter may lead to larger fluxes that may be detectable in current and future indirect detection experiments.[1]

In the remainder of the chapter, we review elements that enter any discussion of the indirect detection of dark matter. First, we briefly review basics of cosmic ray propagation, as well as the form of the source term arising from dark matter annihilation. We then discuss constraints from both anti-protons and synchrotron radiation. We then discuss prospects for observations of non-thermally produced wino dark matter in positrons and gamma rays. With both PAMELA (a Payload for Antimatter Matter Exploration and Light-nuclei Astrophysics) and FGST (Fermi Gamma-ray Space Telescope) in orbit, these two signals are particularly timely. Throughout, we attempt to point out where astrophysical assumptions enter. Finally, we comment on implications for the LHC, and briefly discuss implications for direct detection and indirect searches for dark matter via neutrinos.

4.2 Cosmic Rays

4.2.1 Production

Our emphasis will be on the identification of high energy cosmic rays from dark matter annihilation. However, disentangling this component relies on an understanding of the other components of cosmic rays. Cosmic rays can be observed directly, e.g. from supernova ejecta (primaries). Alternately, these cosmic rays can interact with the interstellar medium producing secondaries. Both components contribute

[1] While we will concentrate on wino dark matter, the results are a bit more general. In the region of interest, the winos annihilate nearly exclusively to W bosons. So, basically what we are probing is a dark matter candidate that annihilates to W's with a given cross section.

to the cosmic ray background, and typically have a flux that is a power-law as a function of their kinetic energy. This is an anticipated property of cosmic rays of astrophysical origin.

The annihilation products of a dark matter particle will be associated with a given energy scale (its mass), and thus can conceivably be distinguished from power law backgrounds. These annihilations will act as a source term:

$$Q = \frac{1}{2}\left(\frac{\rho(r)}{m_\chi}\right)^2 \langle\sigma v\rangle \frac{dN}{dp}(p), \tag{4.2}$$

where $\rho(r)$ is the dark matter profile, and $\frac{dN}{dp}(p)$ is the spectrum of stable particles resulting from the annihilation. We simulated $\frac{dN}{dp}(p)$ using PYTHIA [49] and altered the dark matter source code in GALPROP[126] to accept this as input.

When looking at most indirect signals of dark matter, the profile of the dark matter is an important ingredient. N-body simulations seem to favor cusped profiles at the center of the galaxy such as the Navarro-Frenk-White (NFW) [127] and Merritt [128] profiles, while dynamical observations of galaxies seem to favor cored profiles of the isothermal variety [129]. Current dark matter simulations do not yet include the effects of baryons. Baryons dominate the gravitational potential in the center of our galaxy, so we find it prudent to consider three dark matter profiles. The first is the Navarro-Frenk-White profile:

$$\rho(r) = \rho_\odot \left(\frac{r_\odot}{r}\right)\left(\frac{1+(r_\odot/r_s)}{1+(r/r_s)}\right)^2, \tag{4.3}$$

with $r_s = 20$ kpc, where $r_\odot = 8.5$ kpc is the galactocentric distance of the sun and $\rho_\odot = 0.3$ GeV/cm^3 is the local dark matter density. The second is the isothermal profile

$$\rho(r) = \rho_\odot \frac{1+(r_\odot/r_s)^2}{1+(r/r_s)^2}, \tag{4.4}$$

with $r_s = 3.5$ kpc, and finally the Merritt et al. profile

$$\rho(r) = \rho_\odot \exp\left[-\left(\frac{2}{\alpha}\right)\frac{r^\alpha - r_\odot^\alpha}{r_s^\alpha}\right], \tag{4.5}$$

with $\alpha = 0.17$ and $r_s = 25$ kpc.

4.2.2 Cosmic Ray Propagation

Charged particles from dark matter annihilation must traverse part of the galaxy before arriving at detectors near Earth. This propagation has a non-trivial effect on the form of the signal.

Annihilations will take place in both the galactic plane and the dark matter halo. Once these particles are produced, they will either become confined by the galactic magnetic field to an approximately cylindrical region or escape the galaxy forever. Their propagation may be described by a diffusion equation, whose details we will now review. Some of the parameters entering this equation are uncertain, and will give rise to uncertainties in the observed dark matter signals.

In modeling propagation of cosmic rays through the galaxy, we will assume cylindrical symmetry (Fig. 4.1). We will adopt a cylinder with height $2L$, and some maximum radius R. The stars and dust will be confined to the galactic plane $z = 0$. The dark matter halo has a spherical symmetry. The particles are allowed to freely escape at the boundaries, and propagation within the cylinder is described by the diffusion-loss equation [126]:

$$\begin{aligned}\frac{\partial}{\partial t}\frac{dn}{dp}(\vec{x},t,p) &= \vec{\nabla}\cdot(D_{xx}(\vec{x},E,t)\vec{\nabla}\frac{dn}{dp} - \vec{V}\frac{dn}{dp}) - \frac{\partial}{\partial p}(\dot{p}\frac{dn}{dp} - \frac{p}{3}(\vec{\nabla}\cdot\vec{V})\frac{dn}{dp}) \\ &\quad + \frac{\partial}{\partial p}(p^2 D_{pp}\frac{\partial}{\partial p}(\frac{1}{p^2}\frac{dn}{dp})) + Q(\vec{x},t,p).\end{aligned} \tag{4.6}$$

The Diffusion coefficient: Cosmic rays diffuse out of the galaxy by scattering off

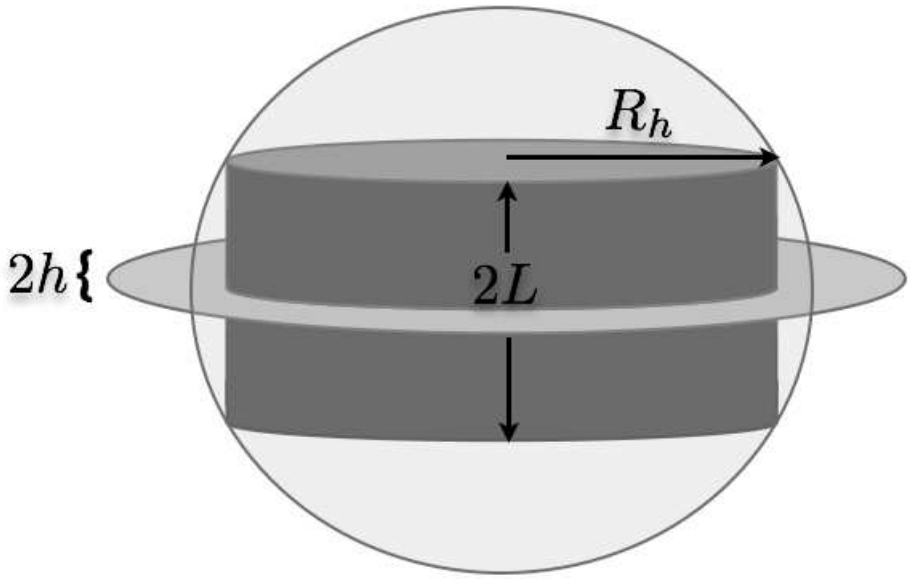

Figure 4.1: The diffusion zone (cylinder) is taken to have a height $2L$, with L in the range of 4-12 kpc [133], whereas the radial direction is taken as $R_h = 20$ kpc (see figure 1). Most of the interstellar gas is confined to the galactic plane at $z = 0$, which represents a slice through the cylinder and has a height of $2h = 100$ pc. Our solar system is then located in this plane at a distance of around $r_0 = 8.5$ kpc from the galactic center. All of this is enveloped by a spherically symmetric dark matter halo.

inhomogeneities in the magnetic field. The diffusion coefficient

$$D_{xx} = \beta K_0 \left(\frac{\mathcal{R}}{\mathcal{R}_0} \right)^{\delta}, \tag{4.7}$$

is a function of the rigidity $\mathcal{R} \equiv p/Z$ where Z is the atomic number. K_0 is a constant, $\mathcal{R}_0$ is some reference rigidity, β is velocity, and δ is the scaling with respect to the momentum. We take a default value $K_0 = 5.8 \times 10^{28}$ cm^2 s^{-1}. The scaling, δ, is set by the spectrum of magneto-hydrodynamic turbulence in the interstellar medium. It is 0.33 for a Kolmogorov type spectrum, and 0.5 for a Kraichnan type spectrum[130]. Values in this region are reasonable. The dependence on β can be understood simply: higher β increases collisions with the inhomogeneities, and hence the diffusion.

Energy Loss: The energy loss, $\dot{p}$, comes from several sources: bremsstrahlung, Coulombic interactions with ionized gasses, inverse Compton scattering with starlight and with the CMB, and synchrotron radiation. Inverse Compton scattering and synchrotron radiation are the largest contributors to energy loss for electrons and positrons and not important for anti-protons. In the case of electrons the energy loss time is sometimes parametrized by τ, with $\dot{p} \propto p^2/\tau$. A typical value is $\tau \approx 10^{16}$ sec.

Re-acceleration: Re-acceleration comes from second order Fermi processes and is described as diffusion in momentum space. It enters the diffusion equation via the term proportional to D_{pp} in Eqn. (4.6). If magnetic fields move randomly in a galaxy, cosmic rays can be speed up when reflected from a magnetic mirror coming them. Likewise, they are slowed down by reflecting from a mirror moving away. The diffusion coefficient D_{xx} and the re-acceleration coefficient D_{pp} are related via the Alfvén velocity [131]. These magnetic field waves are moving slowly with respect to higher energy cosmic rays, so re-acceleration only will affect the low energy cosmic rays.

Convection: The convection current $\vec{V}$ can be thought of as a wind streaming in

the z direction outward from the galactic plane. It is due to the outgoing plasmas from the galaxy, and in our galaxy can be thought of as coming from cosmic rays accelerating the plasma [132]. For the case of positrons, convection and annihilations in the disk can be neglected.

Source terms and radioactive decays: For astrophysical sources, the source term Q is expected to proportional to a power law $\propto p^{-\gamma}$ localized in the galactic plane. It may also contain sources and sinks due to unstable cosmic rays.

We will employ GALPROP [126] for numerical solutions to the diffusion-loss equation.

4.2.3 Some Uncertainties

Measurements of the boron to carbon ratio help to fix the ratio of primary to secondary cosmic rays. Boron is produced purely as a secondary, while carbon is mostly primary. This observation helps fix both the height of the diffusion zone and the diffusion parameters K_0 and δ. However, there can exist a large degeneracy between these parameters[134, 135]. Increasing the height of the diffusion zone traps more cosmic rays. This can be compensated by a simultaneous change in the diffusion parameter that allows cosmic rays to quickly escape the galactic plane. Since anti-protons of a non-dark matter origin are produced in the galactic plane as secondaries, just as boron is, this apparent degeneracy of parameters does not give rise to a large uncertainty in the background prediction. Once the primary flux of protons is fixed (measured), the B/C ratio gives a rather precise prediction for the (astrophysical) anti-proton flux.

Unfortunately, the dark matter does not share the same independence of the astrophysical parameters. Depending upon which set of diffusion parameters are chosen, different dark matter signals result. The reason is that dark matter annihilations

are not confined to the galactic plane. Rather, they occur throughout the halo, and increasing the diffusion zone includes more primary cosmic rays from dark matter. This change in L is not completely compensated by an increase in the diffusion out of the galactic plane as in the case of the background. Moreover, this increase in the height of the diffusion zone will affect positrons and anti-protons differently, as we will discuss in the following sections.

4.3 Experimental Constraints on Non-thermal Neutralinos

In this section we use GALPROP [126] to numerically solve the propagation equation (4.6) and find the expected flux of positrons and anti-protons, as well as the synchrotron radiation coming from the annihilation products of neutralino dark matter. When appropriate, we have checked these results explicitly using DarkSUSY [136], and found similar results for similar values of the astrophysical parameters. We discuss the possibility of neutralino dark matter annihilations to explain an excess of positrons as suggested by the HEAT [137, 138] and AMS-01[139] data, while simultaneously respecting the observed flux of anti-protons as measured by BESS [140]. At present, the anti-protons do not show any peculiar spectral features (though their flux is perhaps somewhat lower than expected). We use this data to set bounds. We also discuss bounds on the neutralino annihilation cross section from synchrotron radiation in the "WMAP haze" [141, 142, 143] obtained from the WMAP3 data [144], and discuss implications for the FGST experiment.

4.3.1 Anti-Proton Bounds

Before attempting to fit the HEAT data (or make predictions for the PAMELA experiment), we must take into account bounds from anti-protons. We will compare to the BESS 95 + 97 data [140] taken at the solar minimum, and modulate the

interstellar spectrum with a potential of 550 MV. More recent data from both the 1998 BESS data[145] and the BESS-Polar data [146] will have a different modulation potential but display the same trends. In Figure 4.2, we show the anti-proton flux for varying mass of the wino-like neutralino. As expected, increasing the mass of the wino pushes the spectrum to slightly harder energies. The dominant effect, however, is that an increase in the wino mass results in a decrease in the annihilation cross section as well as number density in the profile, which changes the overall normalization of the curve. Apparently, a wino mass of 150 GeV gives too high a flux, but 200 GeV is (marginally) consistent.

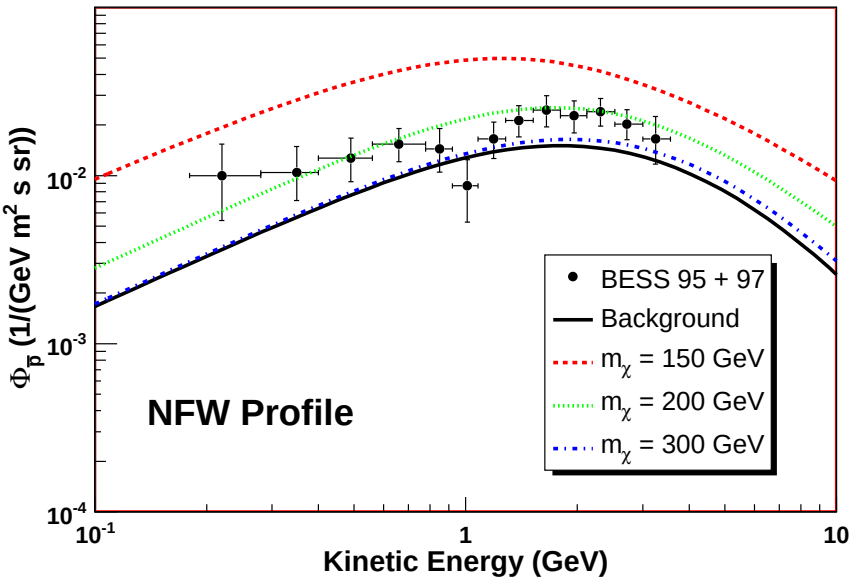

Figure 4.2: The flux in anti-protons for varying neutralino mass ($m_\chi = 150, 200, 300$ GeV). We have taken a diffusion zone height of $L = 4$ kpc.

As can be seen in Figure 4.3, these constraints are sensitive to the diffusion zone height. Here, we fix the neutralino mass at 200 GeV, and vary the diffusion height, L. Clearly the diffusion height directly affects the anti-proton flux. Again, we see that for a height of $L = 4$ kpc, $m_\chi = 200$ GeV is accommodated by the anti-proton data, but for larger diffusion cylinders, heavier winos would be required to be consistent

with the anti-proton data.

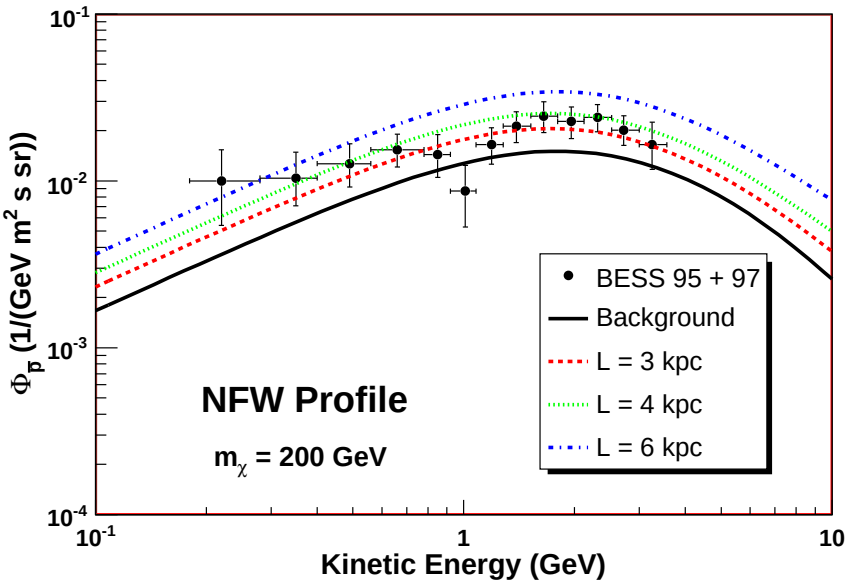

Figure 4.3: The flux in anti-protons for varying height of the diffusion zone cylinder with and NFW dark matter profile. We have taken a $m_\chi = 200$ GeV wino.

This minimum allowed wino mass is also a function of the dark matter distribution in the galaxy. Because anti-protons do not lose energy very efficiently (relative, to say, positrons), they come to us from a large region, and can potentially sample the inner portion of the galaxy, where the dark matter distribution can vary dramatically among different choices of profile. To assess the dependence of the profile on potential dark matter flux from anti-protons, we varied the profile in Fig. 4.4. Note that going from an NFW profile to another profile changes the flux of anti-protons from the dark matter particle by roughly $\pm 15\%$.

Our investigation of the anti-proton flux indicates that a pure wino of approximately 200 GeV is consistent with the data. To achieve significantly lower masses, one would have to push the astrophysical uncertainties. A 150 GeV pure Higgsino, however, is consistent with the data. At this mass, its annihilation cross section is approximately one order of magnitude below that of the wino.

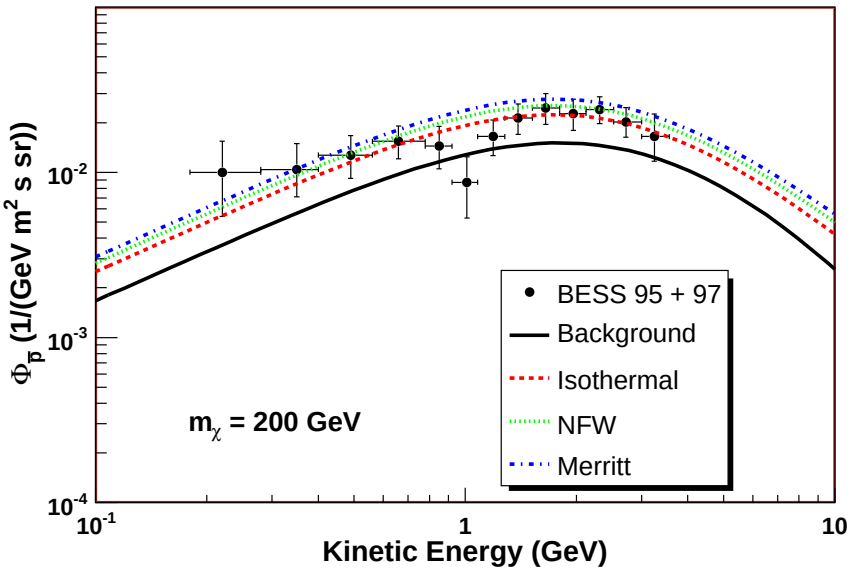

Figure 4.4: The flux of anti-protons is shown using different dark matter distributions. We have fixed $L = 4$ kpc, and the wino mass to be $m_X = 200$ GeV. Since the anti-protons may sample the inner region of the galaxy, the cuspiness of the profile does effect the anti-proton flux.

4.3.2 Synchrotron Radiation

An excess of synchrotron radiation in the WMAP three year data [144], particularly significant for angles south of the galactic plane, has been suggested by subtracting out known foregrounds[141, 142, 143]. The residual component has a harder spectrum than other known sources for microwave emission, and has been dubbed the WMAP haze. Thus it seems that there is an unknown source of relativistic electrons and positrons moving in the galactic magnetic field, contributing to synchrotron emission. These electrons and positron could potentially come from dark matter [142].

While the exact interpretation of the haze is unclear at present, at minimum one should at least check that any potential dark matter candidate does not supersaturate the amount of synchrotron radiation. This has been noted by Hooper [147],

who uses this observation to potentially place bounds on dark matter candidates. Here, we briefly revisit these bounds and semi-quantitatively discuss the astrophysical uncertainties that enter them.[2]

First, we discuss the particles that contribute to the WMAP bands. These electrons have energy greater than 5 GeV. This can be shown by analyzing the equation for synchrotron emission. We use the formula of [149],

$$\epsilon_S(\nu,\gamma) = \frac{4\pi\sqrt{3}e^2\nu_B}{c}x^2(K_{4/3}(x)K_{1/3}(x) - \frac{3}{5}x(K^2_{4/3}(x) - K^2_{1/3}(x))) \tag{4.8}$$

with

$$x = \frac{\nu}{3\gamma^2\nu_B}, \tag{4.9}$$

γ is the boost factor, and the critical frequency is $\nu_B = eB/2\pi m_e c$. Here, K_n is the modified Bessel function of order n. This formula gives the synchrotron emission of the electron into all angles, averaged over an isotropic pitch angle distribution of the electrons with the magnetic field.

Figure 4.5 shows the amount of synchrotron radiation into the 22 GHz band as a function of the electron energy for a few different values of the magnetic field. This band is observed by WMAP, and it gives the most statistically significant contribution to the haze. Error bars in other bands are larger. Emission from energies below 5 GeV is negligible. This demonstrates the link between the haze and high-energy electrons and positrons. Thus, the excess in the HEAT data and the synchrotron emission can be linked to the relativistic electrons of similar energy. Indeed, any positron excess from a future experiment will potentially contribute to the haze at some level. If both the haze and positron excess arise from dark matter, then reconciling them will probe the astrophysical parameters of our galaxy.

[2]It should be noted that very strong bounds from X-rays might result if strong B-fields exist near the black hole near the galactic center[148]. We do not pursue these bounds further here.

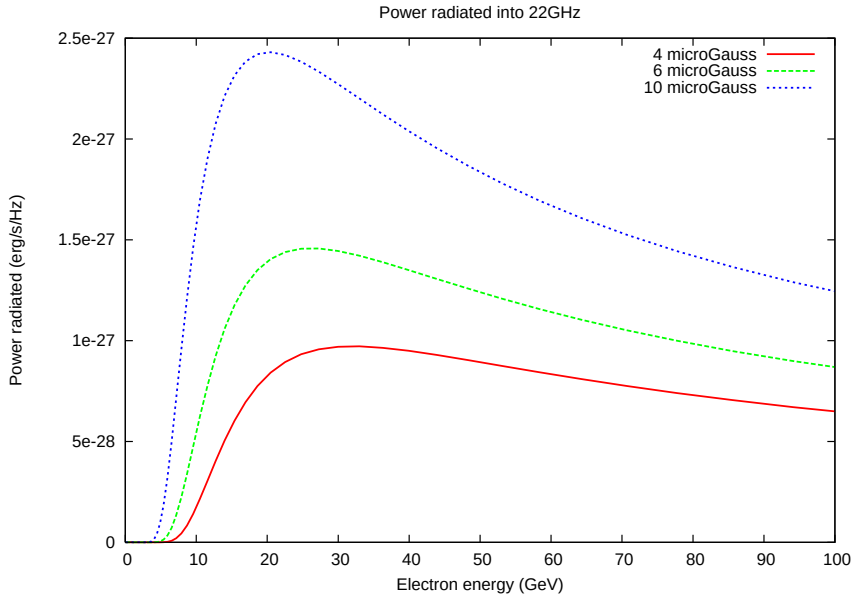

Figure 4.5: Power radiated into 22 GHz as a function of electron energy for different values of the galactic magnetic field. Notice that for energies below 5 GeV, there is negligible radiation.

As a point of reference, [147] argues that a pure wino that gives the full dark matter abundance would be excluded by the haze unless its mass exceeds 700 GeV. This is a very strong bound, and as we will see, would largely preclude any interpretation of any current or future excess in positrons as simple supersymmetric dark matter.

Central to placing this bound is an understanding of how electrons and positrons lose energy within the galaxy. This is controlled by the relative importance of the radiation field and magnetic field in the region of interest. Large magnetic fields will cause the energy loss due to synchrotron radiation to dominate (and hence yield strong bounds from the haze). Large radiation fields will cause inverse Compton scattering to dominate. Reference [147] assumes a relationship between the energy density in the magnetic field and in the radiation field as: $U_B/(U_B + U_{rad}) \sim 0.26$. With a naive equipartition relation one would find this ratio ~ 0.5. There is no tight argument for equipartition between these two contributions. However, it is not

unlikely that this relation should roughly hold at least approximately. After all, the B-field is related to cosmic rays, whose source is astrophysical objects. These, in turn, should roughly trace that radiation distribution.[3]

Having argued that the bound will sensitively depend on the choice of the magnetic and radiation field, we set about to semi-quantitatively investigate this effect by using a different initial set of assumptions. Our view is that our starting point is not obviously less motivated than that of [147]. Our results might then give some indication of the size of the astrophysical uncertainties. Alternately, if one wishes to have a light dark matter particle with large cross section, our discussion will tell you what properties the galaxy must have to accommodate such a candidate.

To find the synchrotron sky map arising from our dark matter annihilation, we use GALPROP 50.1 [126] for the propagation of our dark matter derived electrons. We use the parameters $K_0 = 5.8 \times 10^{28}$ cm^2 /s, $\delta = 0.5$ (consistent with a Kraichnan spectrum of interstellar turbulence) [130], and L = 4 kpc, but find our results are relatively insensitive to these choices. Other choices for propagation parameters yield changes of roughly 10% in the results. The energy loss term is set by the relativistic Klein-Nisha cross section of cosmic rays on the interstellar radiation field combined with the synchrotron radiation from the magnetic field. The injection spectrum of dark matter is modified to accept input from PYTHIA 6.4 [49]. Following [143], we average emission over 20 degrees in longitude. For the interstellar radiation field, we use the fields from [150, 151] that are provided with the GALPROP package. We model the magnetic field by an exponential decay

$$B(r, z) = B_0 e^{-|r|/r_0 - |z|/z_0}. \tag{4.10}$$

We chose the characteristic distance r_0 such that the local magnetic field is $3\,\mu G$,

[3] We thank Dan Hooper for discussion of this point.

and chose z_0 such that the field falls off quickly away from the galactic plane that is supposed to be responsible for creating this field. Also, we will use equation 4.8 to find the synchrotron radiation. With sky-map in hand, following the same approach as [147], we use the synchrotron data of [142] to constrain possible dark matter candidates. Again, we do not assume a thermal history, and instead impose that our dark matter candidates make up all the relic density by fiat. We find a 90% confidence level upper bound on the annihilation cross section by using a χ^2 fit, allowing the addition of a constant background synchrotron piece, independent of angle from the galactic center (relating to possible uncertainty in the subtraction procedure of Finkbeiner, et al.). [4]

It should be noted that we do not recalculate the residual haze for each choice of the magnetic field. However, since the approach of [142] was simply to derive the haze by doing a comparison of sky-maps close to and away from the core, we view this as a reasonable first approximation.

For a cuspy profile, most of the dark matter annihilations will happen in the galactic core. These then propagate outward until they are in the region we are looking at, 1 - 3 kpc from the center. They then radiate into the frequency band observed. Taking the approach outlined above, with $z_0 = 2$ kpc, we find the results in the top panel of Fig. 4.6. In particular, for a pure wino, for an NFW profile we find the bound of 300 GeV, much less stringent than the original bounds from [147]. This is dominantly due to our choice of radiation field maps [150, 151]. For these maps, $U_B/(U_B + U_{rad}) \sim 0.1$ for $B_0 = 10\ \mu G$ in the inner few kpc. A larger value for this ratio pushes us towards the limits of [147]. If an even smaller B field were present, near the galactic center, perhaps as small as 5 μG, this would further degrade the

[4] Unlike [147], we impose the fit over the entire interval from 5 to 35 degrees south of the galactic plane.

limits to the point where the bounds from anti-protons become competitive with (or exceed) these bounds.

Finally, we briefly discuss the effect of the z profile of the magnetic field. It is not clear exactly what form the z dependence of the B field should take. Taking z_0= 1 kpc again loosens the bound relative to our default choice of z_0= 2 kpc. This is shown in the lower panel of Fig. 4.6. Here, the bound on the pure wino dark matter only excludes 125 GeV wino dark matter, even for the relatively peaked NFW profile. In short, the local B-field (i.e. where synchrotron radiation is being measured) has a large effect on the size of the synchrotron radiation signal.

Figure 4.6 also shows the dependence on the galactic profile. Those that have a steeper rise towards the galactic center will give a larger contribution to synchrotron radiation. If the profile is somewhat softer than NFW then the bound is further weakened (this effect was also very clearly shown in [147] where a flat and NFW profile were shown). If the less-peaked isothermal profile is chosen, for example, all bounds due to synchrotron radiation are eliminated, even in the case where the B field falls off with z relatively slowly.

Also shown in the figure are the annihilation cross sections for pure wino and pure Higgsino at low velocity. For masses above M_W, both types of dark matter will annihilate almost exclusively to W bosons. Thus, discussions of γ-rays, synchrotron, $\bar{p}$ and positron signals will be identical for wino and Higgsino dark matter of the same mass, once this cross section difference is accounted for.

There is a very clear relationship between the halo profile and what types of experiments are best suited to look for dark matter. If the halo is quite peaked towards the center of our galaxy, then experiments that look for photons from this region, either gamma rays or synchrotron, will be best suited to find the dark matter.

If, however, the dark matter distribution rises more slowly, then it is no longer clear that the center of the galaxy is the best place to look. Indeed, one can then look for electrons and positrons directly (perhaps from annihilation to W bosons), rather than looking for indirect by-products of annihilation (synchrotron, or continuum gamma rays). We now discuss this possibility.

4.3.3 Positrons

In the case of positrons, it is useful to consider the positron fraction, which includes both the primary flux of positrons $\Phi_{e^+}^{prim}$ as well as the background $\Phi_{e^+}^{sec}$ and the analogous fluxes for electrons, i.e.

$$\Phi = \frac{\Phi_{e^+}^{prim} + \Phi_{e^+}^{sec}}{\Phi_{e^+}^{prim} + \Phi_{e^+}^{sec} + \Phi_{e^-}^{prim} + \Phi_{e^-}^{sec}}, \tag{4.11}$$

as this ratio allows for cancellation of systematic errors and the effects of solar modulation (if we assume no charge bias). Preliminary indications from PAMELA data [152] indicate, however, that this charge bias may be important for low energies. Since the dark matter signals we will consider will involve production of electron and positrons at multi-GeV energies, we believe charge bias should be safely negligible in this regime.

In Figure 4.7, we consider a purely wino-like neutralino for masses in the range $150 - 300$ GeV. We have also included in the figure the data from the 1994 and 1995 HEAT missions [137, 138], as well as the data from AMS-01 [139]. The background curve is generated using the parameters of [153], with an Alfvén velocity of 20 km/s. At present the data begins to deviate from the background curve around 10 GeV, though the error bars are still large.

One might be able to determine the mass of the WIMP from this data. We see that the spectrum peaks slightly below $m_\chi/2$. This arises from annihilation to W-

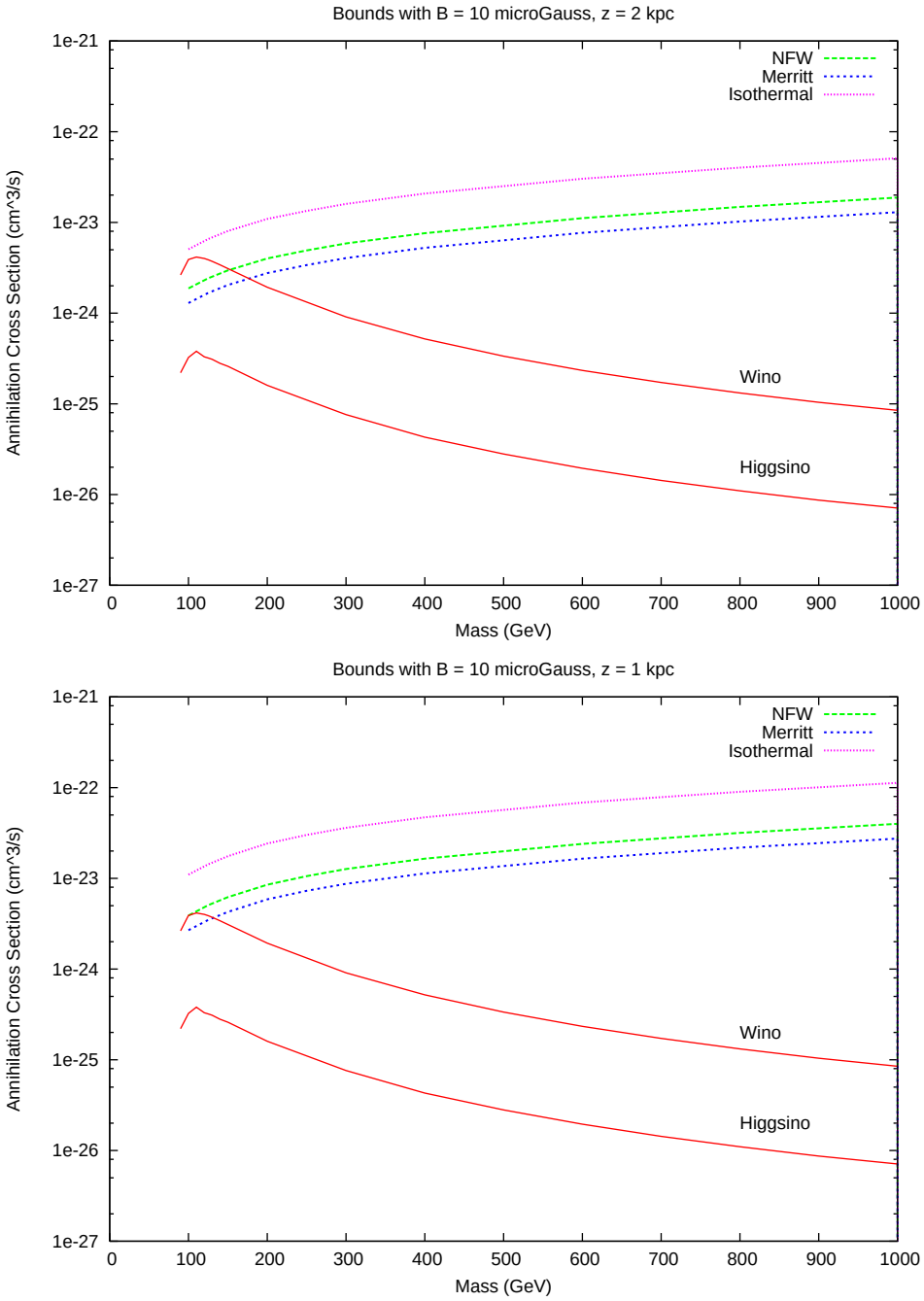

Figure 4.6: Bounds on the annihilation cross section into W^+W^- from synchrotron radiation. We have used the propagation parameters described in the text and only vary the magnetic field properties here.

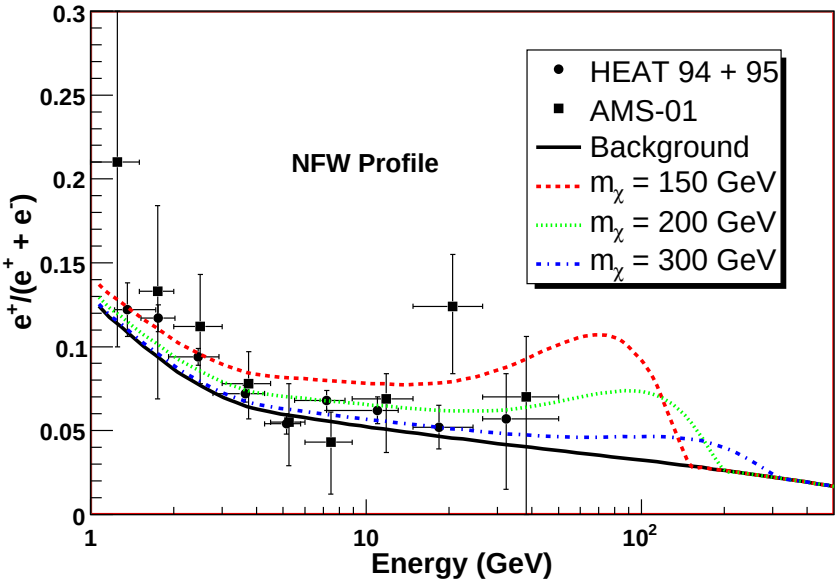

Figure 4.7: The positron flux from annihilations of non-thermally produced wino-like neutralinos for varying masses ($m_\chi = 150, 200, 300$ GeV) keeping and NFW profile. We have also included the data from the 1994-95 HEAT balloon based observations [137, 138] and measurements from AMS-01 [139].

boson pairs and then subsequent decays to e^+/e^- near threshold. At present, there is no turn-over in the data. If PAMELA sees a turn-over in the data, then this would make a indirect measurement of the WIMP mass. A pure wino of up to 400 GeV might be eventually observed by PAMELA (see [114, 154]).

We find similar results for neutralinos that contain some bino or Higgsino component in addition to the wino, however in the case of the bino-like neutralino this can not be too large, otherwise the dark matter will not make a large contribution above the background.

For the case of $\bar{p}$ and synchrotron radiation, there were important astrophysical uncertainties. In particular, the distribution of of dark matter in the halo had a strong effect on the synchrotron bounds. The size of the cylindrical region to which the dark matter annihilation products are confined by the galactic magnetic field has a large effect on the $\bar{p}$ flux.

These two systematics have a much smaller effect on the signal from positrons. The reason is that positrons come from nearby: the typical diffusion length is only a few kpc. Errors in the background are typically much larger than the differences induced in the signal by astrophysical uncertainties. In this section we adopt the NFW halo profile as our canonical choice, noting that we find no significant changes for other profiles. Changing the height of the diffusion cylinder also does not have a very large effect on the positron ratio. We investigated the same cylinder height as shown in the anti-proton section, and again found variations that were small when compared with other uncertainties in the astrophysical backgrounds.

Re-acceleration can have an effect on the positron signal, however. In Figure 4.8 that using different backgrounds compatible with B/C will vary the positron signal as well. We have used backgrounds with varying Alfvén velocities from [153]. The change in Alfvén velocity affects the low energy spectrum. Once the low energy background is normalized to data, this affects the prediction at high energies.

In all our discussions, we have not assumed any "boost factor". If there is some additional substructure in the halo within the diffusion length of the positrons, it is possible to enhance this signal somewhat. However, this substructure could also affect the signal in anti-protons, though not in a precisely identical way as they have a different diffusion length.

4.3.4 Gamma Rays

Dark matter annihilations can produce gamma rays in two ways: either via continuum production through decays of pions in hadronic decay products or directly. Typically, direct annihilations to gamma rays are loop suppressed. Here, we will concentrate on the continuum gamma ray flux, expected to be most relevant for FGST.

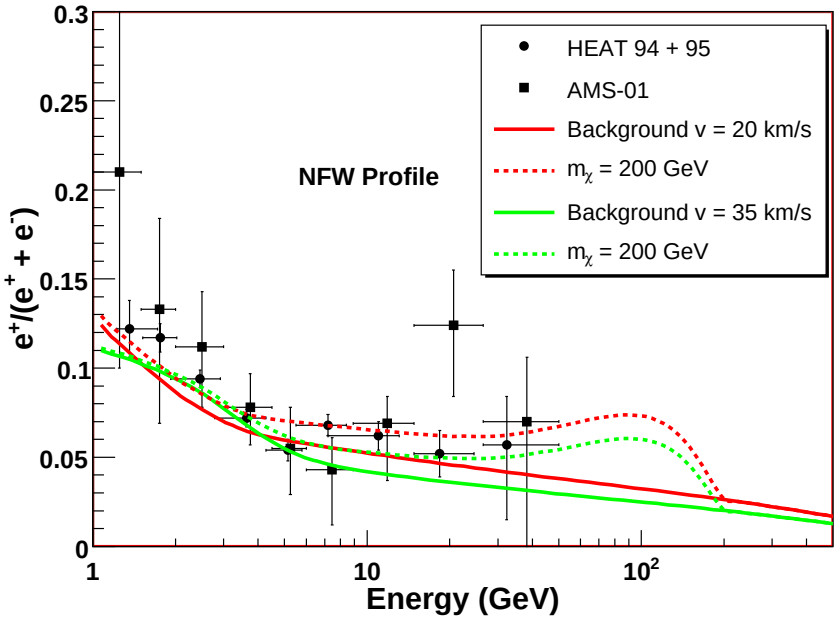

Figure 4.8: The positron ratio is shown for two different background curves, with (dashed) and without (solid) a Dark Matter contribution. The two background curves correspond to different values of the Alfvén velocity, $v = 20$ km/s (red/dark) and $v = 35$ km/s (green/light).

Since photon signals are independent of the propagation parameters for cosmic rays in the galaxy, the sky-map of gamma rays from dark matter annihilations directly trace the density profile. The flux of gamma rays is given by

$$\Phi_{DM}(E,\psi) = \frac{1}{2}\frac{\langle\sigma v\rangle}{4\pi}\int_{l.o.s.} dl(\psi)\frac{\rho(l)^2}{m_\chi^2}\sum_i \frac{dn_{\gamma i}}{dE}B_i, \tag{4.12}$$

where the sum is over the different annihilation channels. B_i is the branching fraction; $\frac{dn_{\gamma i}}{dE}$ is the gamma ray yield, and the integral is over the line of sight. In our calculation of the continuum gamma rays from pions, we take $B_i = 1$ for the W^+W^- final state and zero, otherwise.

EGRET has looked at these signals in the 30 MeV - 50 GeV range, and has found no signals (see however [155]). FGST has recently launched and will have an increased sensitivity over this range. It will also extend observations to 300 GeV. Recently, [156], updated the work of [157], and studied of the sensitivity of FGST to

different dark matter models. Here we discuss the implications of these studies for non-thermal wino dark matter.

The results of Fig. 6 of [156] can be interpreted to place bounds on light winos. In particular, in the case of an NFW profile, wino masses below ≈ 300 GeV should have already been observed by EGRET. For an isothermal profile, the bounds are much weaker, less than 150 GeV. In this case, the strongest bound at present comes from the anti-proton flux.

Given the relatively small masses found in the previous section necessary to explain the HEAT or AMS-01 data (or a future large excess at PAMELA), it is fair to say that there is already some tension between positron signals (if interpreted as dark matter) and the absence of a signal in γ rays if the profile is NFW (or cuspier). If the profile is somewhat softer than NFW, however, then it is possible to accommodate both results. A reduction in the astrophysical factor

$$J \equiv \int_{l.o.s.} dl(\psi) \frac{\rho(l)^2}{m_\chi^2}, \tag{4.13}$$

by a factor of $\approx$ six below its NFW value is necessary for EGRET to accommodate a 200 GeV wino and has no effect on positrons. The improved sensitivity of FGST suggests that an observation in gamma rays is in fact likely for such a WIMP. The study [156] suggest that a pure wino up to 500 GeV could be observed by FGST at 3σ after 5 years of running, assuming an NFW profile.

Here, we have focused exclusively on the bounds (and potentially signals) coming from our own galaxy. This approach will depend on the ability to successfully subtract away point sources and other diffuse backgrounds[158]. To avoid these sources, dwarf galaxies might be competitive places to look depending on their dark matter profiles.

4.4 Summary

A non-thermally produced wino is a well-motivated candidate for the dark matter observed in our universe. Its large annihilation cross section could potentially allow it to explain the suggestion of an excess from HEAT/AMS-01, which has recently been confirmed by PAMELA [160]. However, to avoid conflict with bounds from gamma rays (and perhaps synchrotron radiation), the dark matter distribution cannot be too highly peaked towards the center. There is already some tension in the case of an NFW profile. This fact suggests that if the PAMELA excess in positrons comes from dark matter, FGST should follow with a confirmation.

Any candidate detection by PAMELA and FGST will need to be examined in the context of direct detection experiments. We do not do that here, since the pure wino LSP suggested by the present positron excess gives signals well below the current sensitivity of the current direct detection experiments. However, adding an admixture of Higgsino to the neutralino allows an increase in the direct detection cross section (via the $\tilde{w} - \tilde{h} - h$ coupling). An increased Higgsino content also increases the capture cross section on the sun, allowing for a possible indirect detection via neutrinos. Thus, signals in these types of experiments could help to probe the Higgsino content of the LSP.

At the LHC, a pure wino of a few hundred GeV by itself may be difficult to observe via direct production. However, it may be possible to find it in decays or associated production. The sensitivity of this modes depends on the mass of the lightest colored mode. In minimal models of anomaly mediation [119], the ratio of the wino mass to the gluino mass is a factor of nine. So a 200 GeV wino implies a 1.8 TeV gluino, which might preclude an early discovery. However, if the mass difference is smaller,

as occurs in some models of non-thermal production then it might be possible to determine the wino nature of the LSP by looking for charged tracks, as recently studied in [159]. More generally, several LHC signatures will depend on the mass and type of the LSP, so we expect that careful studies will be able to test whether a candidate seen in indirect data is also present in LHC data.

CHAPTER V

The PAMELA Positron Excess and Constraints on Wino-like Dark Matter

Recently, the PAMELA collaboration (a Payload for Anti-Matter Exploration and Light-nuclei Astrophysics) released preliminary results [160] indicating an excess of cosmic ray positrons above the 10 GeV energy range. This confirms earlier results from HEAT [137, 138] and AMS-01 [139], which had already received some initial interest from theorists, e.g., [161, 162, 163].

One possible explanation for the positron excess is the annihilation of weakly interacting massive particles (WIMPS) in the galaxy. A spate of new particle physics models have been proposed, in part to fit the detailed features of the PAMELA data [164, 165]. However, it is worth exploring in detail whether a well-established candidate (such as the neutralino) could plausibly fit the data. As discussed in Chapter IV, for this explanation to be valid the neutralinos would need to have a larger cross section than dark matter of thermal origin.

In light of the preliminary findings of PAMELA, we revisit the non-thermal neutralino model considered in Chapter IV, as well as those in [166, 123, 163], to determine whether they could account for the excess[1]. We find a wino-like neutralino with mass roughly 200 GeV comes close to accounting for the excess, but only if

[1] See also a recent discussion in [167].

unconventional assumptions about the underlying distribution of the dark matter or the propagation of its annihilation products are made. Without such modifications, a light supersymmetric particle appears unable to account for the data. In part, the purpose of this paper is to point out the places where the sources of tension arise for this explanation, while simultaneously highlighting the types of astrophysical modifications that would need to be made to accomodate the data. Such a candidate is well motivated theoretically. For example, a wino LSP arises in theories where the anomaly–mediated[168] contribution to the gaugino masses dominates, including simple realizations of split supersymmetry, and the string constructions where M-theory is compactified on a G_2 manifold[169].

A pure-wino 200 GeV neutralino annihilates dominantly to W-bosons, with a cross section $\langle \sigma v \rangle = 2 \times 10^{-24}$ cm^3 s^{-1}. It is remarkable that this cross section is approximately the correct one needed to explain the size of the signal in the data. Masses somewhat below 200 GeV could conceivably explain the spectrum from the positron data, but such candidates come into sharper conflict with the existing limits from anti-protons and gamma rays. Even at 200 GeV, a wino has tension with the existing data, a fact implicit in [170, 171]. In fact, taking the data at face value, such a candidate is excluded. In the following, we will show how close the 200 GeV neutralino comes to the current data, given the present understanding of the astrophysics. Given the inherent astrophysical uncertainties, it is not unreasonable to think the 200 GeV case might ultimately be consistent with existing positron, anti-proton and γ-ray data. Neutralino masses much larger than this give a bad fit to the PAMELA results unless very large astrophysical boost factors are employed [172]. This discussion is based on the results found in [15].

5.1 Positron Excess from Neutralino Dark Matter

Dark matter annihilations produce a differential flux of cosmic rays per unit time, energy and volume as

$$Q(E,\vec{x}) = \frac{1}{2}\langle\sigma_x v\rangle \left(\frac{\rho_x(\vec{x})}{m_x}\right)^2 \sum_i B_i \frac{dN^i}{dE}, \tag{5.1}$$

where E is kinetic energy of the cosmic rays, $\langle\sigma_x v\rangle$ is the thermally averaged annihilation cross section and velocity of the non-relativistic dark matter, B_i and dN^i/dE are the branching ratios and fragmentation functions, and the sum is taken over all annihilation channels which contain positrons in the final state. The observed flux of cosmic rays is then found by propagating the source of Eq. (5.1), along with any astrophysical sources of cosmic rays (background) to the Earth. There are three sources of uncertainty for the prediction of any Dark Matter signal: the dark matter distribution, the propagation of its annihilation products, and the role of astrophysical backgrounds.

Unless otherwise stated, we restrict our attention to the commonly adopted Navarro-Frenk-White (NFW) profile [127]. This distribution is spherically symmetric and has the form:

$$\rho(r) = \rho_\odot \left(\frac{r_\odot}{r}\right)\left(\frac{1+(r_\odot/r_s)}{1+(r/r_s)}\right)^2, \tag{5.2}$$

with $r_s = 20$ kpc, where $r_\odot = 8.5$ kpc is the galactocentric distance of the sun and $\rho_\odot = 0.3$ GeV/cm^3 is the local dark matter density. Any reasonable profile will not effect the positrons appreciably, since they are mostly local. However, constraints from EGRET (and predictions for FGST) are directly effected by this choice, as well as fluxes from anti-protons. While the choice of profile does not appreciably effect the positron spectrum, the local sub-structure (clumpiness) of the dark matter, could have important effects, as we will soon discuss.

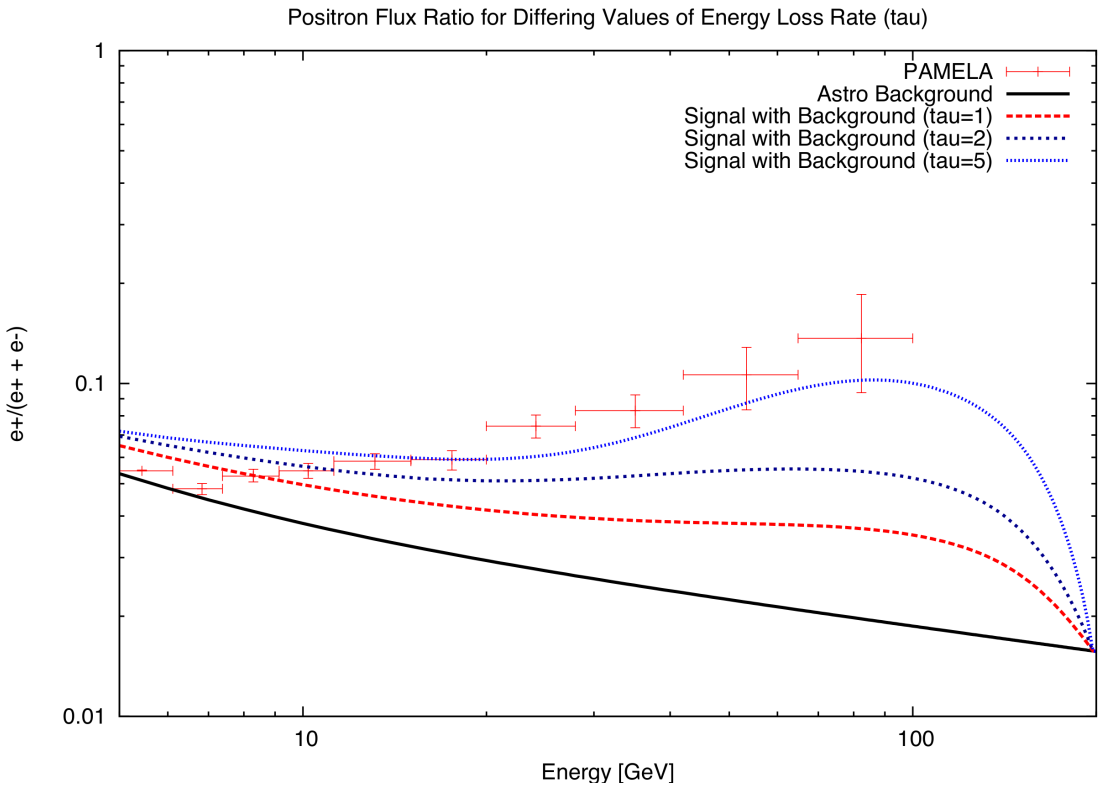

Figure 5.1: Positron flux ratio for Wino-like Neutralino with a mass of 200 GeV, normalized to the local relic density. We set the height of the propagation region at 4 kpc and consider varying values for the energy loss rate ($\tau = 1, 2, 5$) in units of 10^{16} s. The solid bottom line represents a conventional astrophysical background [174].

For propagation of the cosmic rays resulting from WIMP annihilations we use DARKSUSY [173] and GALPROP [126], to numerically solve for the fluxes. We vary the propagation parameters to examine how well a light neutralino can account for the positron excess. As standard values we take a diffusion coefficient of $K = 3 \times 10^{27} \epsilon^{0.6}$ cm^2 s^{-1}, a half height for the confinement region of $L = 4$ kpc, and an energy loss time of $\tau = 10^{16}$ s. For the astrophysical background in positrons we adopt the power-law $\Phi = (4.5\epsilon^{0.7}) \,/\, (1 + 650\epsilon^{2.3} + 1500\epsilon^{4.2})$ from [174], where ϵ is the energy in units of GeV.

For comparing theoretical predictions for positrons with the data, it is customary to consider the positron fraction, which includes both contributions from dark mat-

ter $\Phi_{e^+}^{DM}$ as well as the astrophysical background $\Phi_{e^+}^{bkg}$ and the analogous fluxes for electrons, i.e.

$$\Phi = \frac{\Phi_{e^+}^{DM} + \Phi_{e^+}^{bkg}}{\Phi_{e^+}^{DM} + \Phi_{e^+}^{bkg} + \Phi_{e^-}^{DM} + \Phi_{e^-}^{bkg}}, \tag{5.3}$$

Our results for a 200 GeV particle that annihilates to W bosons appear in Figure 5.1. We have set the annihilation cross section, by assuming that the particle is a pure wino. The preliminary data of PAMELA are also shown [160], along side the anticipated signal in the presence of a 200 GeV wino[2]. The bottom (solid) curve represents the astrophysical background. The next higher curve represents the 200 GeV wino for the NFW halo profile and default propagation parameters discussed above. The dark matter signal does not provide a convincing explanation for the excess reported by PAMELA.

However, we find that by varying the rate of energy loss of the positrons a better fit to the data is possible. Positrons lose energy via synchrotron radiaton and via inverse compoton scattering off diffuse starlight and the cosmic microwave background. These energy losses are parameterized by the energy loss time τ. At the energies of interest this is dominated by the interaction of the positrons with starlight. While have seen that the typically chosen default value of $\tau = 10^{16}$ s gives a poor fit to the data, claims in the literature [176], indicate that there are theoretical uncertainties in τ at the level of a factor of 2. So, we provide a curve for $\tau = 2 \times 10^{16}$ s, still a poor fit. A $\tau = 5 \times 10^{16}$ s gives a qualitatively good fit to the data. It is unclear that such a value is consistent with extant maps of starlight[177]. To clarify whether a neutralino could fit the data, it is important to determine this with certainty.

[2]Below 10 GeV, the effects of charge bias on the solar modulation are expected to be non-negligible. We have checked that solar modulation [175] can bring the PAMELA data into improved agreement with the theoretical estimate, but do not attempt a detailed accounting of the solar modulation which would require additional detailed data on the solar B field. As the dark matter signal is dominant at higher energies, we focus on the region above 10 GeV where these effects are not important.

The distribution of the Dark Matter could also significantly impact the fit. Depending on the distribution of the dark matter (e.g., if there are significant over densities of the Dark Matter close by) astrophysical boost factors could also contain a dependence on the energy (see e.g. [178]). This would largely mimic the effects of a change in τ, and could act to change the spectrum from the dark matter annihilation. An extreme example of this effect appeared recently in [172], where a local clump of 800 GeV wino Dark Matter was able to give the desired spectrum. We stress that the results appearing in Figure 5.1 do not include any astrophysical boost factors.

In summary, allowing for uncertainties in the energy loss rate and/or allowing for a small energy dependent boost factor may lead to an *effective* value of τ that could allow the 200 GeV candidate to account for the excess reported by PAMELA. Without invoking these uncertainties, an additional source of positrons is required.

5.2 Existing Constraints

Strong bounds are set by existing data from γ-ray and anti-proton measurements. However both suffer from a number of uncertainties.

5.2.1 Gamma Ray Constraints

We begin with a brief review of γ-ray fluxes coming from dark matter annihilations, which are sensitive to both the halo profile and the diffuse γ-ray background. We then discuss existing constraints coming from the Energetic Gamma Ray Experiment Telescope (EGRET), which observed γ-rays coming from the galactic center.

5.2.1.1 Overview of γ-rays from dark matter Annihilation

We are interested in the continuum energy spectrum of gamma-ray flux coming from neutralino annihilations. The differential flux is given by

$$\frac{d^2\Phi_\gamma}{d\Omega dE_\gamma} = \frac{\langle\sigma v\rangle}{8\pi m_\chi^2}\sum_f \frac{dN_f}{dE_\gamma}B_f \int_{l.o.s}\rho^2(l)dl(\psi), \tag{5.4}$$

which is in units of photons/cm^2/s/GeV/steradian (sr).

The first factor depends only on the particle physics. $\langle\sigma v\rangle$ is the thermally averaged product of the annihilation cross section. dN_f/dE_γ is the differential photon yield for a particular decay with branching ratio B_f, and the sum is taken over all relevant decays. The second piece contains the distribution of dark matter, where $\rho(l)$ is the dark matter halo density profile and the integral is performed along the line of sight that originates from our location in the galaxy and continues through the full extent of the halo at an angle ψ relative to the ray passing through the galactic-center.

To isolate astrophysical uncertainties it is convenient to introduce the dimensionless function $J(\psi)$

$$J(\psi) \equiv \frac{1}{r_\odot \rho_\odot^2}\int_{l.o.s}\rho^2(l)dl(\psi). \tag{5.5}$$

Ground and satellite based detectors will observe a finite patch of the sky with a given angular resolution. Therefore, when comparing theoretical predictions with what may be detected, we should average J over the minimum angular resolution of the detector,

$$\langle J\rangle = \frac{1}{\Delta\Omega}\int J(\psi)d\Omega \tag{5.6}$$

where $\Delta\Omega$ is the angular resolution (in steradians). This value is dictated by the experiment, e.g. this corresponds to $\Delta\Omega = 10^{-3}$ sr for EGRET, and $\Delta\Omega = 10^{-5}$

Profile	EGRET & Ground Based ($\Delta\Omega = 10^{-3}$ sr)	FGST ($\Delta\Omega = 10^{-5}$ sr)
Isotherm	30	30
NFW	1,214	12,644
Einasto	1,561	5,607

Table 5.1: The averaged line of site integral $\langle J \rangle$ to the galactic center for the NFW, Einasto, and Isothermal profiles with EGRET and FGST minimal resolution.

sr for FGST. Given the minimum angular resolution, the dark matter profile, and the source location we can perform the average in (5.6) using e.g. DarkSUSY. Some results for the line of sight integral to the galactic center appear in Table 1. An examination of Table 1 shows that the difference between a flat profile (Isothermal Cored) and NFW for EGRET can introduce two orders of magnitude difference in the signal. We also show the $\langle J \rangle$ for the Einasto profile, which has recently been favored by N-body simulations [179].

While isothermal cores are now disfavored by N-body simulations, it is still fair to say that the current lack of knowledge of the halo profile induces a large error in the predicted flux from the galactic center.

Using the expression for the flux (5.4) and averaging over the angular acceptance, the differential flux measured in the detector is

$$\begin{aligned} \frac{d\Phi_\gamma}{dE_\gamma} &= 9.40 \times 10^{-12} \left(\frac{\langle \sigma v \rangle}{10^{-27} cm^3 \cdot s^{-1}} \right) \\ &\times \left(\frac{100 \text{ GeV}}{m_\chi} \right)^2 \sum_f \frac{dN_f}{dE_\gamma} B_f \, \langle J \rangle \Delta\Omega, \end{aligned} \tag{5.7}$$

which is in units of photons/cm^2/s/GeV.

γ-ray signals from dark matter annihilations must compete with the diffuse γ-ray background. These include inverse Compton scattering of electrons with galactic radiation and bremsstrahlung processes from accelerated charges [180]. Thus, uncertainties in the propagation of cosmic rays and in the composition of the ISM (e.g. the

distribution and density of hydrogen) lead to uncertainties in the expected diffuse background. It is vital to understand the diffuse background in order to confirm (or deny) the existence of dark matter annihilations and to distinguish between different theoretical predictions.

At the present level of understanding, the differential flux for the diffuse γ-ray background may be fitted by a power-law of the form [181]

$$\frac{d^2\Phi_\gamma^{bg}}{d\Omega dE_\gamma} = \left(\frac{d^2\Phi_\gamma^{bg}}{d\Omega dE_\gamma}\right)_0 \left(\frac{E_\gamma}{1\text{GeV}}\right)^\alpha, \tag{5.8}$$

with $\alpha = -2.72$ and a normalization $\left(d^2\Phi_\gamma^{bg}/d\Omega dE_\gamma\right)_0 = 6 \times 10^{-5}$.

5.2.1.2 Constraints from EGRET

EGRET completed nine years of observations in June of 2000 and was sensitive to γ-rays in the energy range 30 MeV - 30 GeV. Using (5.8) for the diffuse background near the galactic center and integrating over the angular resolution of EGRET ($\Delta\Omega = 10^{-3}$) for the energy range of interest (1 GeV $\lesssim E_\gamma \lesssim$ 30 GeV) we find a background flux of $\Phi_\gamma^{bg} \simeq 10^{-8}$ photons cm^{-2} s^{-1}. For dark matter candidates that give a flux in excess of this, EGRET should have detected a signal. From (5.4), a neutralino annihilating to W-bosons with a mass of a couple hundred GeV and cross section $\langle\sigma v\rangle \approx 10^{-24}$ cm^3 s^{-1} yields a flux comparable to the background $\Phi_\gamma^{dm} \simeq 4 \times 10^{-8}$ photons cm^{-2} s^{-1}. This gives the first indication of the tension between a 200 GeV wino and the EGRET data. Of course, this result depends on the dark matter profile – assumed here to be NFW.

Extracting robust constraints on dark matter candidates from EGRET is subtle for reasons extending beyond the choice of the profile: there are uncertainties in both the diffuse background, as well as the EGRET data itself.

EGRET has detected a possible excess above 1 GeV in all sky directions. Address-

ing the discrepancy between the expected diffuse background and the EGRET data has been considered by a number of authors [182, 185, 183, 184, 180, 187, 186, 135]. These authors have argued for explanations that range from the possibility of annihilating dark matter[3] [186] to systematic errors in the EGRET experiment [187].

A key challenge for addressing the possible excess is developing an accurate model of the astrophysical background. This is particularly challenging given the inability to disentangle various components. These include the weak extragalactic contribution to the diffuse background, as well as a number of possible unresolved point sources [182, 156]. Due to the uncertainties, proposed models for the background can vary significantly. Compared to the background in Eqn. (5.8),

The 'conventional' GALPROP model [126] assumes a larger contribution from inverse Compton scattering, giving a higher contribution to the background and therefore to any signal that would be seen by EGRET. Yet other choices of background exist, including the 'Optimized' background [126], chosen to fit the EGRET excess without any additional Dark Matter component. At present, the take-home message is that there are large uncertainties in the astrophysical background.

In addition to the uncertainties associated with the diffuse background and the halo profile, there are other reasons for concern in regards to the quality of the EGRET data. Indeed, EGRET was only designed to operate for two of its nine year mission and an aging spark chamber introduced time-dependent uncertainties and systematic errors into the high end data products [188]. In [187] is was found that the most likely explanation of the EGRET excess was an error in the estimation of the EGRET sensitivity at energies above a GeV. This was argued to be convincing given that the 'excess' is seen in all sky directions, not just towards the galactic

[3]This explanation relies on a non-standard (anisotropic) choice for the halo profile, and seems to be at odds with other sources of indirect detection [135].

center.

With these caveats in mind, we use the EGRET data to constrain the 200 GeV wino. We state the constraint as a bound on the $\langle J \rangle$. Assuming EGRET correctly measured the background above a GeV and using the data from [189] to determine the diffuse background, we find that a 200 GeV wino has an annihilation cross section too large by a factor of three for an NFW profile – for a softer profile $\langle J \rangle \simeq 380$ this would not be the case. These findings agree with already existing bounds in the literature [190, 182, 156]. However, we have also found that using the lower choice for the diffuse background in Eqn. (5.8) implies that the 200 GeV wino is already marginally consistent with the EGRET data for the NFW profile[4].

For now, it seems reasonable to consider the close proximity of the 200 GeV dark matter to the current bounds set by EGRET encouraging, since we will see in Section 5.3 that the improvements of FGST should clarify the situation.

5.2.2 Anti-Proton Bounds

Measurements of cosmic ray anti-proton fluxes can also be used to put constraints on light neutralino candidates. In fact, the PAMELA experiment will measure anti-proton fluxes in the energy range 80 MeV - 190 GeV. It has already reported early data [191] which seems consistent with and extends earlier results, e.g. [145, 140, 146].

Taken at face value, the anti-proton data would appear to exclude a 200 GeV wino as an explanation of the PAMELA data, see e.g. [170]. However, anti-proton constraints suffer from theoretical uncertainties in cosmic ray propagation, as has been demonstrated in [192] (see also the discussion in [135]). One approach to bound the uncertainties and set propagation parameters for anti-protons is to parametrically fit models to well measured secondary/primary fluxes such as the Boron to Carbon

[4] See [70] for a similar approach to dealing with uncertainties in the diffuse background and bounds on neutralinos coming from EGRET and FGST.

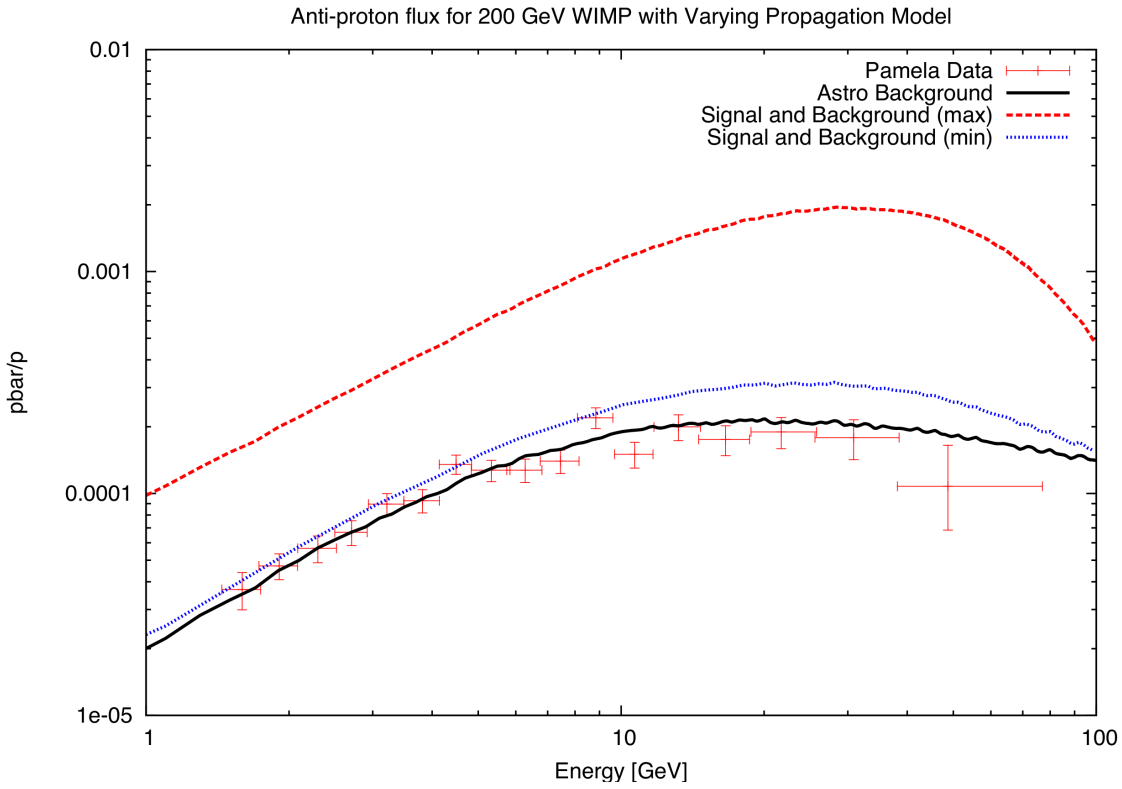

Figure 5.2: The anti-proton flux ratio for a 200 GeV wino-like neutralino as a function of kinetic energy. The lowest curve represents the conventional astrophysical background, whereas the remaining curves are the signal plus background for the 200 GeV candidate. These curves are the flux from dark matter annihilations given different choices for propagation model – all of which have been parametrically fixed by matching to the well known spectrum of secondary/primary fluxes (e.g. B/C ratio) [192].

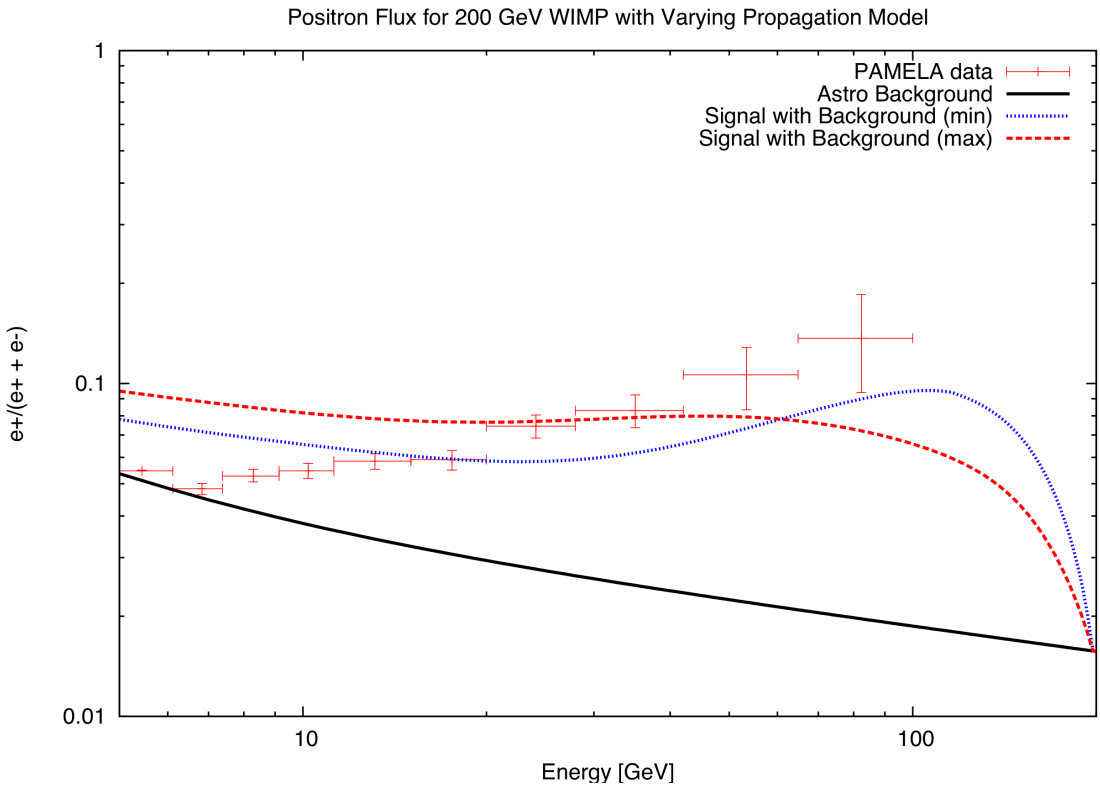

Figure 5.3: Positron flux ratio for a wino-like neutralino with a mass of 200 GeV. The lowest curve represents the astrophysical background, whereas the remaining curves are the flux ratio for (large) energy loss rate of $\tau = 5 \times 10^{16}$ s and varying propagation model (as discussed in the text).

(B/C) ratio. In [192] it was found that this technique suffers from a number of degeneracies. These degeneracies arise from the fact that the effective size of the confining region in which the cosmic rays propagate and the amount of energy lost to diffuse processes can be varied in combination, giving a good fit to the B/C ratio for a variety of values.

For the 200 GeV candidate we consider here, and assuming an NFW profile, the uncertainties in the propagation can lead to variations in the Dark Matter induced anti-proton flux by as much as an order of magnitude. This can be seen in Figure 5.2, where we present the dark matter signal for the benchmark propagation models appearing in [192] that yield the minimum and maximum anti-proton signal. Both

models are consistent with the B/C ratio. The order of magnitude variation in the theoretical prediction might cause the reader to be hesitant to conclude a 200 GeV wino is excluded from the data. At present, even for the minimal choice of propagation model, the 200 GeV candidate still gives a prediction that is about two times that expected from the recent observations of PAMELA [191]. If a 200 GeV wino is to explain the data, there must be additional problems with the models used to propagate the anti-protons.

Variation of the propagation parameters will also influence the positron spectrum. Once the anti-proton flux is minimized, what happens to the positrons? This effect is not that pronounced, primarily because the high-energy positrons relevant for PAMELA originate within a couple kpc of Earth. Propagation uncertainties are thus reduced relative to those for anti-protons. Fig. 5.3 shows the effect on positrons of using the "min" and "max" models used for Fig. 5.2.

5.3 Future Probes and Predictions for FGST

As we have mentioned, PAMELA will probe positron cosmic rays from 50 MeV up to an estimated 270 GeV. Thus, if a light wino-like neutralino is responsible for the positron excess, PAMELA must see a turn-over in the data, as can be seen from Figure 5.1.

The ATIC experiment [193] has also reported an excess of cosmic ray electrons above roughly 300 GeV. The wino candidate we describe here could not be responsible for this excess. If the 200 GeV wino indeed accounts for the PAMELA excess, another explanation would be required for the ATIC data.

We now consider the ability of FGST to detect the 200 GeV wino invoked above We focus on measurements of the galactic center, though measurements of the halo

could be useful if progress is made in understanding the backgrounds there in detail. In particular [194, 195] discuss the possibility to detect DM annihilations from galactic substructure (sub-halos dispersed throughout the primary halo), which is suggested by certain N-body simulations. FGST may be able to resolve this structure.

FGST will offer a significant improvement over EGRET, probing energies from 20 MeV to 300 GeV with an angular resolution of around 0.1 degrees ($\approx 10^{-5}$ sr). The improved angular resolution will not only allow for separation of the point sources detected by EGRET, but the increased sensitivity will allow for a better opportunity to distinguish dark matter annihilation signals from the diffuse background. For the energy range of interest (around 1 GeV $\lesssim E_\gamma \lesssim$ 300 GeV) one finds a background flux from (5.8) of around $\Phi_\gamma^{bg} \simeq 10^{-10}$ photons cm^{-2} s^{-1} at a FGST angular acceptance of 10^{-5} sr. Compared with the EGRET result of $\Phi_\gamma^{EGRET} \simeq 10^{-8}$ photons cm^{-2} s^{-1}, this allows for an improved sensitivity by two orders of magnitude in terms of resolving signal from background. As in the case of EGRET, the diffuse background and halo profile are both sources of significant uncertainty. The better resolution and ability of FGST to resolve point sources should improve our knowledge of the diffuse background.

For our predictions for FGST we consider an $0.5^\circ \times 0.5^\circ$ region about the galactic center assuming an NFW profile and averaging with a minimum resolution set by FGST (i.e. 10^{-5} sr). We have considered a number of choices for modeling the diffuse background. We find that for both a low choice of background given by the power-law with normalization in (5.8), as well as for higher backgrounds such as the 'conventional' and 'optimized' backgrounds mentioned above, that FGST will report a signal early. We find for the conventional background and a 200 GeV wino that

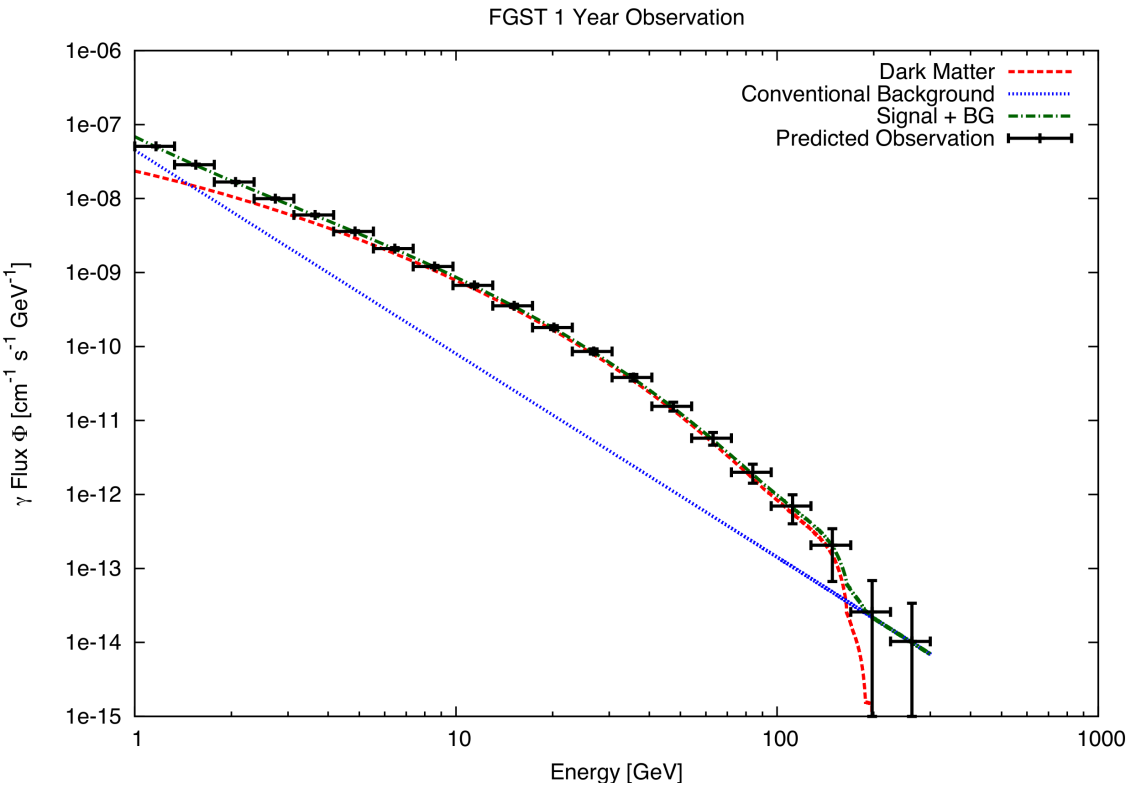

Figure 5.4: The differential flux for the 200 GeV wino-like neutralino and an NFW profile averaged over the minimum angular resolution of FGST (i.e. $\Delta\Omega = 10^{-5}$ sr) and integrated over a $0.5^\circ \times 0.5^\circ$ region around the galactic center. For the diffuse background we take the 'conventional' galprop model discussed in the text. The error bars represent the statistical uncertainty after one year of observations and do not account for systematical uncertainties.

a variation in the halo profile down to $\langle J \rangle \simeq 70$ in the region about the galactic center can still result in a detectable signal for FGST at the 5σ level within the first year of observation. In Figure 5.4 we present the prediction for the 200 GeV wino with an NFW profile, again after only one year of data. The error bars reflect statistical uncertainties. FGST should be capable of observing the products of wino annihilation after the first year.

5.4 Summary

The PAMELA group [160] has reported a robust excess in galactic positrons with energy above about 10 GeV, compared to those expected from known astrophysical sources. This is consistent with earlier reported excesses from [137, 138, 139]. The source that produces postirons will likely produce antiprotons and γ-rays. No unambiguous excess in these channels has been observed, which provides constraints on a dark matter interpretation.

Only if standard assumptions about the propagation of cosmic rays are relaxed can the excess in positrons arise from galactic annihilation of winos, the superpartners of W bosons. Although there are apparent conflicts with anti-protons and gammas, given the astrophysical uncertainties it is likely premature to assume the wino interpretation is completely excluded. Further investigation of these uncertainties is a topic for future work. Fortunately, data from FGST and further data from PAMELA will help to clarify the picture soon. Later data from AMS-02 will also help.

If the PAMELA excess is indeed due to a well-motivated wino LSP, the implications are remarkable. We would learn what the dark matter of our universe is. It would be the discovery of supersymmetry, telling us something about the resolution to the hierarchy problem. It would imply a number of superpartners will likely be seen at LHC, confirming the result. And we would be learning that the universe had a non-thermal cosmological history that we can probe.

CHAPTER VI

Conclusions

This thesis focused on studying how supersymmetry can be observed at both the LHC, as well as several astrophysical observation experiments that may be indirectly sensitive to dark matter. We presented several novel approaches to the problem of extracting meaningful information about the fundamental SUSY parameters, even when the signal is difficult to recover at the LHC. Additionally, we explored bounds on SUSY models of non-thermal dark matter from recent astrophysical observation experiments.

In Chapter II we considered a different and well-motivated example of gluino pair production at the LHC, where each gluino can have a large decay fraction to two top quarks and the neutralino LSP. This results in events with four top quarks and large missing energy in the final state. We found this scenario can be observed in excess of the SM background with only a few hundred pb^{-1} integrated luminosity, potentially allowing for rapid discovery. However, an inherently large jet multiplicity and increased combinatorical backgrounds make direct reconstruction of top quarks extremely inefficient. We demonstrated a robust approach whereby four-top events are identified by fitting counting-signature measurements to various hypotheses for the underlying physics model.

In chapter III we investigated the problem of identifying gaugino mass unification from LHC measurements. Specifically we examine the scenario known as mirage-mediation, which incorporates both gravity- and anomaly-mediation. The relative contribution of each mechanism is controlled by a single parameter α. In the limit $\alpha \to 0$ one recovers the mSUGRA relation for the low-scale gaugino mass parameters associated with universal boundary conditions, $M_1 : M_2 : M_3 = 1 : 2 : 6$. For $\alpha > 0$ one departs from universality and eventually approaches anomaly mediation. We showed that by utilizing a χ^2-like metric on the space of a specific set of LHC signatures, it is possible to detect non-universality to roughly $\alpha \simeq 0.3$ with only a few fb^{-1} for the majority of the parameter space.

In Chapter IV we argued that the positron excess reported by HEAT may be explained by a 200 GeV wino LSP. A wino LSP is well-motivated, and arises naturally in models based on anomaly mediation, as well as string-models compactified on a G_2 manifold. However, a wino WIMP annihilates far too efficiently to account for the observed relic abundance Ωh^2 assuming a thermal history. Verification of this scenario would be remarkable, as it would indicate the existence of a non-thermal source of DM. However, in Chapter V we revisited this scenario, and also argued that such a WIMP does not convincingly model the more recent PAMELA measurements if conventional astrophysical propagation parameters are assumed. Even if one is able to model the positron emission, tension appears with the anti-proton data, which appear to follow the conventional background assumption while the DM annihilation should produce a detectable excess.

6.1 Future Directions

A potential avenue for future work is to focus on using the techniques presented here to determine the nature of the LSP. The properties of a neutralino LSP are controlled by SUSY-breaking. Specifically, the soft-breaking lagrangian permits mixing between the gauginos and higgsinos, resulting in a mass-eigenstate wavefunction for the neutralino that consists of an admixture of the electroweak-inos. The composition of this admixture has significant implications for both the form of useful collider signatures at the LHC, and also the cosmological properties that a LSP WIMP may have. Therefore, determination of the LSP wavefunction is crucial to understanding our cosmological history as well as the nature of SUSY breaking. With the LHC set to begin operations later this year, and a host of other direct and indirect-detection experiments ongoing and planned, it may very soon be possible to achieve this goal.

This research program should tackle two primary objectives:

1. Find a robust technique for distinguishing the composition of a LSP WIMP using measurements at LHC.

2. Determine the role a LSP WIMP plays in explaining the apparent excesses observed in several recent indirect-detection experiments (e.g. ATIC, HEAT, and PAMELA), by performing a thorough investigation of the theoretical uncertainties and assumptions associated with these models.

A viable approach to achieving the first objective is to utilize a footprint-style analysis similar to that presented in Chapter III to distinguish various LSP compositions. Due to the nature of hadron collisions, production of colored gluinos and squarks is expected to dominate at the LHC. If supersymmetry maintains R-parity invariance, these will be produced in pairs and immediately undergo a sequence of

decays that terminates with the creation of a stable LSP. The LSP itself escapes direct detection due to its weak coupling to ordinary matter. However, the branching ratios involved in the decays - and therefore also the collider signatures - are sensitive to the low scale spectrum, as well as the LSP composition. Thus, it should be possible to identify signatures exhibiting high sensitivity to the LSP composition and utilize them to differentiate various admixtures.

While our study focused on detecting small variations from universality, the approach is clearly also sensitive to the neutralino LSP wavefunction, since its composition depends on the relative values of M_1, M_2, and also the higgsino mass parameter μ. Thus it should be possible to readily extend this analysis in a model-independent fashion and examine much wider variations in these parameters, corresponding to bino, wino, as well as higgsino LSP examples. Following success at this stage, the study can be extended further to show distinguishability between more complicated admixtures.

The second objective can be achieved by thoroughly studying the apparent excesses in the ATIC [193] and HEAT [137] /PAMELA [160] positron data and their relation to dark matter annihilation. As discussed in Chapter V numerous studies appeared [164, 165] that attempt to explain the positron excess as the result of WIMP annihilations in the galactic halo. Intrinsic to these studies, however, is significant theoretical uncertainty, both in the astrophysical assumptions regarding cosmic-ray propagation and background sources, as well as in the computation of particle fluxes from DM annihilation (for example we do not understand exactly how the DM is distributed throughout the galaxy). While future measurements will help resolve these issues, if we are to believe that DM is indeed the LSP, it is then prudent to consider that the observed excesses may be only partially due to DM annihilation,

and explore the constraints from not only indirect-detection, but also direct detection experiments (e.g. Xenon100, CDMS) as well as astrophysical explanations, such as local pulsars [196]. This objective is deeply related to the first, as it is essential to verify that DM properties obtained from measurements at different experiments are fully consistent with one another.

Successful completion of this effort will result in a greater understanding of how properties of a neutralino LSP can be probed at the LHC. Most importantly, a standard technique will be developed that will allow experimentalists to quickly determine the composition of the LSP using relatively little data. Because the principles associated with this method are not limited to the LSP, additional knowledge will be obtained regarding detection of additional superpartners. This information can then be used in conjunction with available and forthcoming astrophysical measurements to further constrain the properties of DM, and to identify the role the LSP plays in explaining its origin.

BIBLIOGRAPHY

BIBLIOGRAPHY

[1] S. Weinberg, Phys. Rev. D **13**, 974 (1976), Phys. Rev. D **19**, 1277 (1979); E. Gildener, Phys. Rev. D **14**, 1667 (1976); L. Susskind, Phys. Rev. D **20**, 2619 (1979); G. 't Hooft, in *Recent developments in gauge theories*, Proceedings of the NATO Advanced Summer Institute, Cargese 1979, (Plenum, 1980).

[2] L.E. Ibáñez and G.G. Ross, Phys. Lett. B **110**, 215 (1982).

[3] P. Langacker, "Precision Tests Of The Standard Model," in Proceedings of the PASCOS90 Symposium, (World Scientific, 1990); J. Ellis, S. Kelley, and D. Nanopoulos, Phys. Lett. B **260**, 131 (1991); U. Amaldi, W. de Boer, and H. Furstenau, Phys. Lett. B **260**, 447 (1991); P. Langacker and M. Luo, Phys. Rev. D **44**, 817 (1991); C. Giunti, C.W. Kim and U.W. Lee, Mod. Phys. Lett. A **6**, 1745 (1991);

[4] L. Alvarez-Gaume, J. Polchinski and M. B. Wise, Nucl. Phys. B **221**, 495 (1983); L. E. Ibanez, Phys. Lett. B **118**, 73 (1982); J. R. Ellis, D. V. Nanopoulos and K. Tamvakis, Phys. Lett. B **121**, 123 (1983); K. Inoue, A. Kakuto, H. Komatsu and S. Takeshita, Prog. Theor. Phys. **68**, 927 (1982) [Erratum-ibid. **70**, 330 (1983)]; A. H. Chamseddine, R. L. Arnowitt and P. Nath, Phys. Rev. Lett. **49**, 970 (1982);

[5] H. Bachacou, I. Hinchliffe and F. E. Paige, Phys. Rev. D **62**, 015009 (2000) [arXiv:hep-ph/9907518]; C. G. Lester, "Model independent sparticle mass measurements at ATLAS,"; "ATLAS detector and physics performance. Technical design report. Vol. 2,", CERN-LHCC-99-015 ATLAS-TDR-15. May 1999, Sections 20.2.3-20.2.6, 20.2.9.

[6] C. Amsler *et al.* [Particle Data Group], Phys. Lett. B **667**, 1 (2008).

[7] P. W. Higgs, Phys. Rev. **145**, 1156 (1966); F. Englert and R. Brout, Phys. Rev. Lett. **13**, 321 (1964); G. S. Guralnik, C. R. Hagen and T. W. B. Kibble, Phys. Rev. Lett. **13**, 585 (1964).

[8] T. Yanagida, *In Proceedings of the Workshop on the Baryon Number of the Universe and Unified Theories, Tsukuba, Japan, 13-14 Feb 1979*

[9] M. J. G. Veltman, Acta Phys. Polon. B **12**, 437 (1981).

[10] P. Binetruy, "Supersymmetry: Theory, experiment and cosmology," *Oxford, UK: Oxford Univ. Pr. (2006) 520 p*

[11] S. P. Martin, "A Supersymmetry Primer," arXiv:hep-ph/9709356.

[12] N. Arkani-Hamed, G. L. Kane, J. Thaler and L. T. Wang, "Supersymmetry and the LHC inverse problem," JHEP **0608**, 070 (2006) [arXiv:hep-ph/0512190].

[13] B. S. Acharya, P. Grajek, G. L. Kane, E. Kuflik, K. Suruliz and L. T. Wang, arXiv:0901.3367 [hep-ph].

[14] B. Altunkaynak, P. Grajek, M. Holmes, G. Kane and B. D. Nelson, arXiv:0901.1145 [hep-ph].

[15] P. Grajek, G. Kane, D. Phalen, A. Pierce and S. Watson, arXiv:0812.4555 [hep-ph].

[16] P. Grajek, G. Kane, D. J. Phalen, A. Pierce and S. Watson, arXiv:0807.1508 [hep-ph].

[17] T. Gherghetta and A. Pomarol, Nucl. Phys. B **586**, 141 (2000) [arXiv:hep-ph/0003129]. K. Agashe, A. Delgado, M. J. May and R. Sundrum, JHEP **0308**, 050 (2003) [arXiv:hep-ph/0308036].

[18] S. Dimopoulos and H. Georgi, Nucl. Phys. B **193**, 150 (1981).

[19] T. Appelquist, H. C. Cheng and B. A. Dobrescu, Phys. Rev. D **64**, 035002 (2001) [arXiv:hep-ph/0012100].

[20] N. Arkani-Hamed, A. G. Cohen and H. Georgi, Phys. Lett. B **513**, 232 (2001) [arXiv:hep-ph/0105239].

[21] Z. Chacko, H. S. Goh and R. Harnik, Phys. Rev. Lett. **96**, 231802 (2006) [arXiv:hep-ph/0506256].

[22] K. Agashe, A. Belyaev, T. Krupovnickas, G. Perez and J. Virzi, Phys. Rev. D **77**, 015003 (2008) [arXiv:hep-ph/0612015]. V. Barger, T. Han and D. G. E. Walker, Phys. Rev. Lett. **100**, 031801 (2008) [arXiv:hep-ph/0612016]. B. Lillie, L. Randall and L. T. Wang, JHEP **0709**, 074 (2007) [arXiv:hep-ph/0701166]. A. L. Fitzpatrick, J. Kaplan, L. Randall and L. T. Wang, JHEP **0709**, 013 (2007) [arXiv:hep-ph/0701150]. K. Agashe, H. Davoudiasl, G. Perez and A. Soni, Phys. Rev. D **76**, 036006 (2007) [arXiv:hep-ph/0701186]. U. Baur and L. H. Orr, Phys. Rev. D **76**, 094012 (2007) [arXiv:0707.2066 [hep-ph]]. R. Frederix and F. Maltoni, arXiv:0712.2355 [hep-ph]. U. Baur and L. H. Orr, arXiv:0803.1160 [hep-ph]. J. Thaler and L. T. Wang, JHEP **0807**, 092 (2008) [arXiv:0806.0023 [hep-ph]]. D. E. Kaplan, K. Rehermann, M. D. Schwartz and B. Tweedie, Phys. Rev. Lett. **101**, 142001 (2008) [arXiv:0806.0848 [hep-ph]]. L. G. Almeida, S. J. Lee, G. Perez, G. Sterman, I. Sung and J. Virzi, arXiv:0807.0234 [hep-ph]. L. G. Almeida, S. J. Lee, G. Perez, I. Sung and J. Virzi, arXiv:0810.0934 [hep-ph].

[23] G. Brooijmans, ATLAS note, ATL-PHYS-CONF-2008-008.

[24] Y. Bai and Z. Han, arXiv:0809.4487 [hep-ph].

[25] H. C. Cheng, I. Low and L. T. Wang, Phys. Rev. D **74**, 055001 (2006) [arXiv:hep-ph/0510225]. P. Meade and M. Reece, Phys. Rev. D **74**, 015010 (2006) [arXiv:hep-ph/0601124]. A. Freitas and D. Wyler, JHEP **0611**, 061 (2006) [arXiv:hep-ph/0609103]. A. Belyaev, C. R. Chen, K. Tobe and C. P. Yuan, arXiv:hep-ph/0609179. S. Matsumoto, M. M. Nojiri and D. Nomura, Phys. Rev. D **75**, 055006 (2007) [arXiv:hep-ph/0612249]; M. M. Nojiri and M. Takeuchi, arXiv:0802.4142 [hep-ph]. T. Han, R. Mahbubani, D. G. E. Walker and L. T. Wang, arXiv:0803.3820 [hep-ph].

[26] R. Contino and G. Servant, JHEP **0806**, 026 (2008) [arXiv:0801.1679 [hep-ph]].

[27] S. Kraml and A. R. Raklev,

[28] B. Lillie, J. Shu and T. M. P. Tait, JHEP **0804**, 087 (2008) [arXiv:0712.3057 [hep-ph]].

[29] For a recent review on top quark related new physics signatures, see T. Han, arXiv:0804.3178 [hep-ph].

[30] For a recent review, see D. J. H. Chung, L. L. Everett, G. L. Kane, S. F. King, J. D. Lykken and L. T. Wang, Phys. Rept. **407**, 1 (2005) [arXiv:hep-ph/0312378].

[31] M. Gerbush, T. J. Khoo, D. J. Phalen, A. Pierce and D. Tucker-Smith, Phys. Rev. D **77**, 095003 (2008) [arXiv:0710.3133 [hep-ph]].

[32] A. R. Zerwekh, C. O. Dib and R. Rosenfeld, Phys. Rev. D **77**, 097703 (2008) [arXiv:0802.4303 [hep-ph]]. P. Fileviez Perez, R. Gavin, T. McElmurry and F. Petriello, arXiv:0809.2106 [hep-ph]. T. Plehn and T. M. P. Tait, arXiv:0810.3919 [hep-ph].

[33] B. A. Dobrescu, K. Kong and R. Mahbubani, arXiv:0709.2378 [hep-ph].

[34] P. Langacker, G. Paz, L. T. Wang and I. Yavin, Phys. Rev. Lett. **100**, 041802 (2008) [arXiv:0710.1632 [hep-ph]]. H. Verlinde, L. T. Wang, M. Wijnholt and I. Yavin, JHEP **0802**, 082 (2008) [arXiv:0711.3214 [hep-th]]. P. Langacker, G. Paz, L. T. Wang and I. Yavin, Phys. Rev. D **77**, 085033 (2008) [arXiv:0801.3693 [hep-ph]].

[35] L. L. Everett, I. W. Kim, P. Ouyang and K. M. Zurek, JHEP **0808**, 102 (2008) [arXiv:0806.2330 [hep-ph]]. L. L. Everett, I. W. Kim, P. Ouyang and K. M. Zurek, Phys. Rev. Lett. **101**, 101803 (2008) [arXiv:0804.0592 [hep-ph]].

S. Nakamura, K. i. Okumura and M. Yamaguchi, Phys. Rev. D **77**, 115027 (2008) [arXiv:0803.3725 [hep-ph]].

K. Choi, K. S. Jeong, S. Nakamura, K. I. Okumura and M. Yamaguchi, arXiv:0901.0052 [hep-ph].

[36] B. S. Acharya, K. Bobkov, G. L. Kane, J. Shao and P. Kumar, arXiv:0801.0478 [hep-ph].

[37] J. J. Heckman and C. Vafa, arXiv:0809.3452 [hep-ph].

[38] A. G. Cohen, D. B. Kaplan, F. Lepeintre and A. E. Nelson, Phys. Rev. Lett. **78** (1997) 2300 [arXiv:hep-ph/9610252].

[39] J. L. Feng, K. T. Matchev and T. Moroi, Phys. Rev. D **61** (2000) 075005 [arXiv:hep-ph/9909334].

[40] N. Arkani-Hamed and S. Dimopoulos, JHEP **0506** (2005) 073 [arXiv:hep-th/0405159]. G. F. Giudice and A. Romanino, Nucl. Phys. B **699** (2004) 65 [Erratum-ibid. B **706** (2005) 65] [arXiv:hep-ph/0406088]. N. Arkani-Hamed, S. Dimopoulos, G. F. Giudice and A. Romanino, Nucl. Phys. B **709** (2005) 3 [arXiv:hep-ph/0409232].

[41] H. Baer, X. Tata and J. Woodside, "PHENOMENOLOGY OF GLUINO DECAYS VIA LOOPS AND TOP QUARK YUKAWA COUPLING," Phys. Rev. D **42**, 1568 (1990).

[42] J. Hisano, K. Kawagoe, R. Kitano and M. M. Nojiri, "Scenery from the top: Study of the third generation squarks at CERN LHC," Phys. Rev. D **66**, 115004 (2002) [arXiv:hep-ph/0204078].

[43] J. Hisano, K. Kawagoe and M. M. Nojiri, "A detailed study of the gluino decay into the third generation squarks at

[44] P. G. Mercadante, J. K. Mizukoshi and X. Tata, Braz. J. Phys. **37**, 549 (2007).

[45] H. Baer, V. Barger, G. Shaughnessy, H. Summy and L. t. Wang, Phys. Rev. D **75**, 095010 (2007) [arXiv:hep-ph/0703289].

[46] P. Gambino, G. F. Giudice and P. Slavich, "Gluino decays in split supersymmetry," Nucl. Phys. B **726**, 35 (2005) [arXiv:hep-ph/0506214].

[47] M. Toharia and J. D. Wells, "Gluino decays with heavier scalar superpartners," JHEP **0602**, 015 (2006) [arXiv:hep-ph/0503175].

[48] R. Bonciani, S. Catani, M. L. Mangano and P. Nason, "NLL resummation of the heavy-quark hadroproduction cross-section," Nucl. Phys. B **529**, 424 (1998) [arXiv:hep-ph/9801375].

[49] T. Sjostrand, S. Mrenna and P. Skands, "PYTHIA 6.4 physics and manual," JHEP **0605**, 026 (2006) [arXiv:hep-ph/0603175].

[50] J. Alwall *et al.*, "MadGraph/MadEvent v4: The New Web Generation," JHEP **0709**, 028 (2007) [arXiv:0706.2334 [hep-ph]].

[51] S. Catani, F. Krauss, R. Kuhn and B. R. Webber, JHEP **0111**, 063 (2001) [arXiv:hep-ph/0109231].

[52] John Conway, "http://www.physics.ucdavis.edu/ conway/research/software/pgs/pgs4-general.htm'

[53] J. Conway, "PGS 4 and the LHC Olympics", Presented at the 3rd LHC Olympics Workshop, KITP, Santa Barbara, Aug 24-25, 2006; "PGS 4", Presented at the MC4BSM Workshop, UC Davis, California, Apr 1-4, 2009.

[54] M. S. Carena *et al.* [Higgs Working Group Collaboration], arXiv:hep-ph/0010338.

[55] W. Beenakker, R. Hopker, M. Spira and P. M. Zerwas, Nucl. Phys. B **492**, 51 (1997) [arXiv:hep-ph/9610490].

[56] See, for example, H. Baer, C. h. Chen, F. Paige and X. Tata, Phys. Rev. D **53** (1996) 6241 [arXiv:hep-ph/9512383].

[57] H. Baer, H. Prosper and H. Summy, Phys. Rev. D **77**, 055017 (2008) [arXiv:0801.3799 [hep-ph]].

[58] Z. Sullivan and E. L. Berger, Phys. Rev. D **78**, 034030 (2008) [arXiv:0805.3720 [hep-ph]].

[59] B. S. Acharya, F. Cavallari, G. Corcella, R. Di Sipio and G. Petrucciani, "Re-discovery of the top quark at the LHC and first measurements," arXiv:0806.0484 [hep-ex].

[60] M. M. Nojiri, G. Polesello and D. R. Tovey, arXiv:hep-ph/0312318.

[61] N. Arkani-Hamed, P. Schuster, N. Toro, J. Thaler, L. T. Wang, B. Knuteson and S. Mrenna, arXiv:hep-ph/0703088.

[62] See, for example,
G. F. Giudice, "Theories for the Fermi Scale," J. Phys. Conf. Ser. **110**, 012014 (2008) [arXiv:0710.3294 [hep-ph]];
G. Brooijmans *et al.*, "New Physics at the LHC: A Les Houches Report. Physics at Tev Colliders 2007 – New Physics Working Group," arXiv:0802.3715 [hep-ph];
M. Fairbairn, A. C. Kraan, D. A. Milstead, T. Sjostrand, P. Skands and T. Sloan, "Stable massive particles at colliders," Phys. Rept. **438**, 1 (2007) [arXiv:hep-ph/0611040].

[63] G. L. Kane, J. D. Lykken, B. D. Nelson and L. T. Wang, "Re-examination of electroweak symmetry breaking in supersymmetry and implications for light superpartners," Phys. Lett. B **551**, 146 (2003) [arXiv:hep-ph/0207168].

[64] G. L. Kane, A. A. Petrov, J. Shao and L. T. Wang, "Initial determination of the spins of the gluino and squarks at LHC," arXiv:0805.1397 [hep-ph].

[65] J. Hubisz, J. Lykken, M. Pierini and M. Spiropulu, "Missing energy look-alikes with 100 pb-1 at the LHC," arXiv:0805.2398 [hep-ph].

[66] S. Yamamoto [ATLAS Collaboration], "Strategy for early SUSY searches at ATLAS," arXiv:0710.3953 [hep-ex].

[67] G. L. Kane, P. Kumar, D. E. Morrissey and M. Toharia, "Connecting (supersymmetry) LHC measurements with high scale theories," Phys. Rev. D **75**, 115018 (2007) [arXiv:hep-ph/0612287].

[68] C. F. Berger, J. S. Gainer, J. L. Hewett, T. G. Rizzo and B. Lillie, "The LHC Inverse Problem, Supersymmetry, and the ILC," arXiv:0711.1374 [hep-ph].

[69] C. F. Berger, J. S. Gainer, J. L. Hewett, B. Lillie and T. G. Rizzo, "General Features of Supersymmetric Signals at the ILC: Solving the LHC Inverse Problem," arXiv:0712.2965 [hep-ph].

[70] B. Altunkaynak, M. Holmes and B. D. Nelson, "Solving the LHC Inverse Problem with Dark Matter Observations," arXiv:0804.2899 [hep-ph].

[71] G. Kane and S. Watson, "Dark Matter and LHC: What is the Connection?," arXiv:0807.2244 [hep-ph].

[72] P. Binetruy, G. L. Kane, B. D. Nelson, L. T. Wang and T. T. Wang, "Relating incomplete data and incomplete theory," Phys. Rev. D **70**, 095006 (2004) [arXiv:hep-ph/0312248];

[73] B. C. Allanach, K. Cranmer, C. G. Lester and A. M. Weber, "Natural Priors, CMSSM Fits and LHC Weather Forecasts," JHEP **0708**, 023 (2007) [arXiv:0705.0487 [hep-ph]];
B. C. Allanach, "Naturalness priors and fits to the constrained minimal supersymmetric standard model," Phys. Lett. B **635**, 123 (2006) [arXiv:hep-ph/0601089];
B. C. Allanach and C. G. Lester, "Multi-Dimensional mSUGRA Likelihood Maps," Phys. Rev. D **73**, 015013 (2006) [arXiv:hep-ph/0507283];
J. R. Ellis, S. Heinemeyer, K. A. Olive, A. M. Weber and G. Weiglein, "The Supersymmetric Parameter Space in Light of B-physics Observables and Electroweak Precision Data," JHEP **0708**, 083 (2007) [arXiv:0706.0652 [hep-ph]];
R. R. de Austri, R. Trotta and L. Roszkowski, "A Markov chain Monte Carlo analysis of the CMSSM," JHEP **0605** (2006) 002 [arXiv:hep-ph/0602028];
L. Roszkowski, R. Ruiz de Austri and R. Trotta, "Implications for the Constrained MSSM from a new prediction for b to s gamma," JHEP **0707**, 075 (2007) [arXiv:0705.2012 [hep-ph]];
J. R. Ellis, S. Heinemeyer, K. A. Olive and G. Weiglein, "Phenomenological indications of the scale of supersymmetry," JHEP **0605**, 005 (2006) [arXiv:hep-ph/0602220].

[74] M. Brhlik and G. L. Kane, "Measuring the supersymmetry Lagrangian," Phys. Lett. B **437**, 331 (1998) [arXiv:hep-ph/9803391].

[75] P. Nath and T. R. Taylor, "Modular invariance, soft breaking, mu and tan(beta) in superstring models," Phys. Lett. B **548**, 77 (2002) [arXiv:hep-ph/0209282].

[76] G. F. Giudice and A. Masiero, "A Natural Solution to the mu Problem in Supergravity Theories," Phys. Lett. B **206**, 480 (1988).

[77] P. Binetruy, G. L. Kane, J. D. Lykken and B. D. Nelson, "Twenty-five questions for string theorists," J. Phys. G **32**, 129 (2006) [arXiv:hep-th/0509157].

[78] J. L. Kneur and G. Moultaka, "Inverting the supersymmetric standard model spectrum: From physical to Lagrangian ino parameters," Phys. Rev. D **59**, 015005 (1999) [arXiv:hep-ph/9807336].

[79] S. P. Martin and M. T. Vaughn, "Regularization dependence of running couplings in softly broken supersymmetry," Phys. Lett. B **318**, 331 (1993) [arXiv:hep-ph/9308222].

[80] N. V. Krasnikov, "The Relation between pole and running masses for gluino and squarks," Phys. Lett. B **345**, 25 (1995).

[81] R. L. Arnowitt and P. Nath, "SUSY mass spectrum in SU(5) supergravity grand unification," Phys. Rev. Lett. **69**, 725 (1992).

[82] S. Bhattacharya, A. Datta and B. Mukhopadhyaya, "Non-universal gaugino masses: a signal-based analysis for the Large Hadron Collider," JHEP **0710**, 080 (2007) [arXiv:0708.2427 [hep-ph]].

[83] S. Bhattacharya, A. Datta and B. Mukhopadhyaya, "Non-universal gaugino and scalar masses, hadronically quiet trileptons and the Large Hadron Collider," arXiv:0809.2012 [hep-ph].

[84] K. Choi and H. P. Nilles, "The gaugino code," JHEP **0704**, 006 (2007) [arXiv:hep-ph/0702146].

[85] G. F. Giudice, M. A. Luty, H. Murayama and R. Rattazzi, "Gaugino mass without singlets," JHEP **9812**, 027 (1998) [arXiv:hep-ph/9810442].

[86] L. Randall and R. Sundrum, "Out of this world supersymmetry breaking," Nucl. Phys. B **557**, 79 (1999) [arXiv:hep-th/9810155].

[87] S. Kachru, R. Kallosh, A. Linde and S. P. Trivedi, "De Sitter vacua in string theory," Phys. Rev. D **68**, 046005 (2003) [arXiv:hep-th/0301240].

[88] M. Grana, "Flux compactifications in string theory: A comprehensive review," Phys. Rept. **423**, 91 (2006) [arXiv:hep-th/0509003].

[89] M. K. Gaillard and B. D. Nelson, "Kähler stabilized, modular invariant heterotic string models," Int. J. Mod. Phys. A **22**, 1451 (2007) [arXiv:hep-th/0703227].

[90] L. L. Everett, I. W. Kim, P. Ouyang and K. M. Zurek, "Deflected Mirage Mediation: A Framework for Generalized Supersymmetry Breaking," Phys. Rev. Lett. **101**, 101803 (2008) [arXiv:0804.0592 [hep-ph]].

[91] L. L. Everett, I. W. Kim, P. Ouyang and K. M. Zurek, "Moduli Stabilization and Supersymmetry Breaking in Deflected Mirage Mediation," JHEP **0808**, 102 (2008) [arXiv:0806.2330 [hep-ph]].

[92] E. Katz, Y. Shadmi and Y. Shirman, "Heavy thresholds, slepton masses and the mu term in anomaly mediated supersymmetry breaking," JHEP **9908**, 015 (1999) [arXiv:hep-ph/9906296].

[93] R. Rattazzi, A. Strumia and J. D. Wells, "Phenomenology of deflected anomaly-mediation," Nucl. Phys. B **576**, 3 (2000) [arXiv:hep-ph/9912390].

[94] T. Gherghetta, G. F. Giudice and J. D. Wells, "Phenomenological consequences of supersymmetry with anomaly-induced masses," Nucl. Phys. B **559**, 27 (1999) [arXiv:hep-ph/9904378];
J. L. Feng, T. Moroi, L. Randall, M. Strassler and S. f. Su, "Discovering supersymmetry at the Tevatron in Wino LSP scenarios," Phys. Rev. Lett. **83** (1999) 1731 [arXiv:hep-ph/9904250];
A. J. Barr, C. G. Lester, M. A. Parker, B. C. Allanach and P. Richardson, "Discovering anomaly-mediated supersymmetry at the LHC," JHEP **0303**, 045 (2003) [arXiv:hep-ph/0208214];
M. Ibe, T. Moroi and T. T. Yanagida, "Possible signals of Wino LSP at the Large Hadron Collider," Phys. Lett. B **644**, 355 (2007) [arXiv:hep-ph/0610277];
S. Asai, T. Moroi, K. Nishihara and T. T. Yanagida, "Testing the Anomaly Mediation at the LHC," Phys. Lett. B **653**, 81 (2007) [arXiv:0705.3086 [hep-ph]];
S. Asai, T. Moroi and T. T. Yanagida, "Test of Anomaly Mediation at the LHC," Phys. Lett. B **664** (2008) 185 [arXiv:0802.3725 [hep-ph]].

[95] M. K. Gaillard, B. D. Nelson and Y. Y. Wu, "Gaugino masses in modular invariant supergravity," Phys. Lett. B **459**, 549 (1999) [arXiv:hep-th/9905122].

[96] J. A. Bagger, T. Moroi and E. Poppitz, "Anomaly mediation in supergravity theories," JHEP **0004**, 009 (2000) [arXiv:hep-th/9911029].

[97] G. L. Kane, J. D. Lykken, S. Mrenna, B. D. Nelson, L. T. Wang and T. T. Wang, "Theory-motivated benchmark models and superpartners at the Tevatron," Phys. Rev. D **67**, 045008 (2003) [arXiv:hep-ph/0209061].

[98] K. Choi, K. S. Jeong and K. i. Okumura, "Phenomenology of mixed modulus-anomaly mediation in fluxed string compactifications and brane models," JHEP **0509**, 039 (2005) [arXiv:hep-ph/0504037].

[99] B. C. Allanach *et al.*, "The Snowmass points and slopes: Benchmarks for SUSY searches," in *Proc. of the APS/DPF/DPB Summer Study on the Future of Particle Physics (Snowmass 2001)* ed. N. Graf, *In the Proceedings of APS / DPF / DPB Summer Study on the Future of Particle Physics (Snowmass 2001), Snowmass, Colorado, 30 Jun - 21 Jul 2001, pp P125* [arXiv:hep-ph/0202233].

[100] `http://www.physics.ucdavis.edu/conway/research/software/pgs/pgs4-general.htm`

[101] D. Feldman, Z. Liu and P. Nath, "Sparticles at the LHC," JHEP **0804**, 054 (2008) [arXiv:0802.4085 [hep-ph]].

[102] J. G. Branson, D. Denegri, I. Hinchliffe, F. Gianotti, F. E. Paige and P. Sphicas [ATLAS and CMS Collaborations], "High transverse momentum physics at the Large Hadron Collider: The ATLAS and CMS Collaborations," Eur. Phys. J. direct C **4** (2002) N1 [arXiv:hep-ph/0110021];
H. Baer, X. Tata and J. Woodside, "Multi - lepton signals from supersymmetry at hadron super colliders," Phys. Rev. D **45**, 142 (1992);
H. Baer, C. h. Chen, F. Paige and X. Tata, "Trileptons from chargino - neutralino production at the CERN Large Hadron Collider," Phys. Rev. D **50**, 4508 (1994) [arXiv:hep-ph/9404212];
H. Baer, C. h. Chen, F. Paige and X. Tata, "Signals for minimal supergravity at the CERN large hadron collider: Multi - jet plus missing energy channel," Phys. Rev. D **52**, 2746 (1995) [arXiv:hep-ph/9503271];
H. Baer, C. h. Chen, F. Paige and X. Tata, "Signals for Minimal Supergravity at the CERN Large Hadron Collider II: Multilepton Channels," Phys. Rev. D **53**, 6241 (1996) [arXiv:hep-ph/9512383];
I. Hinchliffe, F. E. Paige, M. D. Shapiro, J. Soderqvist and W. Yao, "Precision SUSY measurements at LHC," Phys. Rev. D **55**, 5520 (1997) [arXiv:hep-ph/9610544].

[103] `http://www.atsweb.neu.edu/ialtunkaynak/heptools.html#parvicursor`

[104] A. Djouadi, J. L. Kneur and G. Moultaka, "SuSpect: A Fortran code for the supersymmetric and Higgs particle spectrum in the MSSM," Comput. Phys. Commun. **176**, 426 (2007) [arXiv:hep-ph/0211331].

[105] A. Djouadi, M. M. Muhlleitner and M. Spira, "Decays of Supersymmetric Particles: the program SUSY-HIT (SUspect-SdecaY-Hdecay-InTerface)," Acta Phys. Polon. B **38**, 635 (2007) [arXiv:hep-ph/0609292].

[106] J. L. Bourjaily, G. L. Kane, P. Kumar and T. T. Wang, "Outside the mSUGRA box," [arXiv:hep-ph/0504170].

[107] G. L. Kane, P. Kumar and J. Shao, "LHC String Phenomenology," J. Phys. G **34**, 1993 (2007) [arXiv:hep-ph/0610038].

[108] G. L. Kane, P. Kumar and J. Shao, "Unravelling Strings at the LHC," Phys. Rev. D **77**, 116005 (2008) [arXiv:0709.4259 [hep-ph]].

[109] G. Jungman, M. Kamionkowski and K. Griest, "Supersymmetric dark matter," Phys. Rept. **267**, 195 (1996) [arXiv:hep-ph/9506380].

[110] D. Hooper and E. A. Baltz, arXiv:0802.0702 [hep-ph].

[111] E. A. Baltz and J. Edsjo, "Positron propagation and fluxes from neutralino annihilation in the halo," Phys. Rev. D **59**, 023511 (1999) [arXiv:astro-ph/9808243].

[112] G. L. Kane, L. T. Wang and J. D. Wells, Phys. Rev. D **65**, 057701 (2002) [arXiv:hep-ph/0108138];
G. L. Kane, L. T. Wang and T. T. Wang, Phys. Lett. B **536**, 263 (2002) [arXiv:hep-ph/0202156].

[113] E. A. Baltz, J. Edsjo, K. Freese and P. Gondolo, arXiv:astro-ph/0211239;
E. A. Baltz, J. Edsjo, K. Freese and P. Gondolo, Phys. Rev. D **65**, 063511 (2002) [arXiv:astro-ph/0109318].

[114] S. Profumo and P. Ullio, JCAP **0407**, 006 (2004) [arXiv:hep-ph/0406018].

[115] M. Brhlik, D. J. H. Chung and G. L. Kane, Int. J. Mod. Phys. D **10**, 367 (2001) [arXiv:hep-ph/0005158].

[116] E. A. Baltz, M. Battaglia, M. E. Peskin and T. Wizansky, Phys. Rev. D **74**, 103521 (2006) [arXiv:hep-ph/0602187].

[117] W. M. Yao *et al.* [Particle Data Group], J. Phys. G **33**, 1 (2006).

[118] E. W. Kolb and M. S. Turner, Front. Phys. **69**, 1 (1990).

[119] L. Randall and R. Sundrum, Nucl. Phys. B **557**, 79 (1999) [arXiv:hep-th/9810155];
G. F. Giudice, M. A. Luty, H. Murayama and R. Rattazzi, JHEP **9812**, 027 (1998) [arXiv:hep-ph/9810442].

[120] N. Arkani-Hamed and S. Dimopoulos, JHEP **0506**, 073 (2005) [arXiv:hep-th/0405159];
G. F. Giudice and A. Romanino, Nucl. Phys. B **699**, 65 (2004) [Erratum-ibid. B **706**, 65 (2005)] [arXiv:hep-ph/0406088];
N. Arkani-Hamed, S. Dimopoulos, G. F. Giudice and A. Romanino, Nucl. Phys. B **709**, 3 (2005) [arXiv:hep-ph/0409232];

[121] J. D. Wells, Phys. Rev. D **71**, 015013 (2005) [arXiv:hep-ph/0411041].

[122] For a review, see Watson and Kane, to appear.

[123] T. Moroi and L. Randall, "Wino cold dark matter from anomaly-mediated SUSY breaking," Nucl. Phys. B **570**, 455 (2000) [arXiv:hep-ph/9906527].

[124] B. S. Acharya, P. Kumar, K. Bobkov, G. Kane, J. Shao and S. Watson, "Non-thermal dark matter and the Moduli Problem in String Frameworks," arXiv:0804.0863 [hep-ph].

[125] G. F. Giudice, E. W. Kolb and A. Riotto, "Largest temperature of the radiation era and its cosmological implications," Phys. Rev. D **64**, 023508 (2001) [arXiv:hep-ph/0005123].

[126] A. W. Strong and I. V. Moskalenko, "Propagation of cosmic-ray nucleons in the Galaxy," Astrophys. J. **509**, 212 (1998) [arXiv:astro-ph/9807150].

[127] J. F. Navarro, C. S. Frenk and S. D. M. White, "A Universal Density Profile from Hierarchical Clustering," Astrophys. J. **490**, 493 (1997) [arXiv:astro-ph/9611107].

[128] D. Merritt, J. F. Navarro, A. Ludlow and A. Jenkins, "A Universal Density Profile for Dark and Luminous Matter?," Astrophys. J. **624**, L85 (2005) [arXiv:astro-ph/0502515].

[129] G. Gentile, P. Salucci, U. Klein, D. Vergani and P. Kalberla, Mon. Not. Roy. Astron. Soc. **351**, 903 (2004) [arXiv:astro-ph/0403154].

[130] V. S. Ptuskin, I. V. Moskalenko, F. C. Jones, A. W. Strong and V. N. Zirakashvili, Astrophys. J. **642**, 902 (2006) [arXiv:astro-ph/0510335].

[131] E. S. Seo and V. S. Ptuskin, "Stochiastic Reacceleration of Cosmic Rays in Interstellar medium" Astrophysical Journal, 431, 705.

[132] V. N. Zirakashvili et al. "Magnetohydrodynamic wind driven by cosmic rays in a rotating galaxy" Astronomy and Astrophysics, 311, 113.

[133] A. W. Strong and I. V. Moskalenko, arXiv:astro-ph/9903370.

[134] F. Donato, N. Fornengo, D. Maurin, P. Salati and R. Taillet, "cosmic ray antiprotons from relic neutralinos in a diffusion model," arXiv:astro-ph/0306312.

[135] L. Bergstrom, J. Edsjo, M. Gustafsson and P. Salati, "Is the dark matter interpretation of the EGRET gamma excess compatible with antiproton measurements?," JCAP **0605**, 006 (2006) [arXiv:astro-ph/0602632].

[136] P. Gondolo, J. Edsjo, P. Ullio, L. Bergstrom, M. Schelke and E. A. Baltz, "DarkSUSY 4.00 neutralino dark matter made easy," New Astron. Rev. **49**, 149 (2005); P. Gondolo, J. Edsjo, P. Ullio, L. Bergstrom, M. Schelke and E. A. Baltz, "DarkSUSY: Computing supersymmetric dark matter properties numerically," JCAP **0407**, 008 (2004) [arXiv:astro-ph/0406204].

[137] S. W. Barwick *et al.* [HEAT Collaboration], "Cosmic ray positrons at high-energies: A New measurement," Phys. Rev. Lett. **75**, 390 (1995) [arXiv:astro-ph/9505141].

[138] S. W. Barwick *et al.* [HEAT Collaboration], "Measurements of the cosmic-ray positron fraction from 1-GeV to 50-GeV," Astrophys. J. **482**, L191 (1997) [arXiv:astro-ph/9703192].

[139] J. Olzem, UCLA DMS conference (2006) and arXiv:0704.3943;
A. Jacholkowska, Nucl. Phys. B Proc. Suppl. 165 (2007)324.

[140] S. Orito *et al.* [BESS Collaboration], Phys. Rev. Lett. **84**, 1078 (2000) [arXiv:astro-ph/9906426].

[141] D. P. Finkbeiner, "Microwave ISM Emission Observed by WMAP," Astrophys. J. **614**, 186 (2004) [arXiv:astro-ph/0311547].

[142] D. P. Finkbeiner, "WMAP microwave emission interpreted as dark matter annihilation in the inner Galaxy," arXiv:astro-ph/0409027.

[143] D. Hooper, D. P. Finkbeiner and G. Dobler, "Evidence Of dark matter Annihilations In The WMAP Haze," Phys. Rev. D **76**, 083012 (2007) [arXiv:0705.3655 [astro-ph]].

[144] D. N. Spergel *et al.* [WMAP Collaboration], "First Year Wilkinson Microwave Anisotropy Probe (WMAP) Observations: Determination of Cosmological Parameters," Astrophys. J. Suppl. **148**, 175 (2003) [arXiv:astro-ph/0302209].

[145] T. Maeno *et al.* [BESS Collaboration], Astropart. Phys. **16**, 121 (2001) [arXiv:astro-ph/0010381].

[146] K. Abe *et al.*, "Measurement of cosmic-ray low-energy antiproton spectrum with the first BESS-Polar Antarctic flight," arXiv:0805.1754 [astro-ph].

[147] D. Hooper, "Constraining Supersymmetric dark matter With Synchrotron Measurements," arXiv:0801.4378 [hep-ph].

[148] M. Regis and P. Ullio, arXiv:0802.0234 [hep-ph].

[149] G. Ghisellini, P. W. Guilbert, and R. Svensson, "The Synchrotron Boiler" Astrophys. J. **334**, L5.

[150] T. A. Porter and A. W. Strong, arXiv:astro-ph/0507119.

[151] I. V. Moskalenko, T. A. Porter and A. W. Strong, Astrophys. J. **640**, L155 (2006) [arXiv:astro-ph/0511149].

[152] P. Picozza at UCLA Dark Matter 2008.

[153] I. Cholis, L. Goodenough and N. Weiner, "High Energy Positrons and the WMAP Haze from Exciting dark matter," arXiv:0802.2922 [astro-ph].

[154] A. Masiero, S. Profumo and P. Ullio, Nucl. Phys. B **712**, 86 (2005) [arXiv:hep-ph/0412058].

[155] W. de Boer, C. Sander, V. Zhukov, A. V. Gladyshev and D. I. Kazakov, Phys. Rev. Lett. **95**, 209001 (2005) [arXiv:astro-ph/0602325].

[156] E. A. Baltz *et al.*, arXiv:0806.2911 [astro-ph].

[157] D. Hooper and B. L. Dingus, Phys. Rev. D **70**, 113007 (2004) [arXiv:astro-ph/0210617].

[158] S. Dodelson, D. Hooper and P. D. Serpico, Phys. Rev. D **77**, 063512 (2008) [arXiv:0711.4621 [astro-ph]].

[159] S. Asai, T. Moroi and T. T. Yanagida, Phys. Lett. B **664**, 185 (2008) [arXiv:0802.3725 [hep-ph]].

[160] O. Adriani *et al.*, arXiv:0810.4995 [astro-ph]; M. Casolino and P. Collaboration, arXiv:0810.4980 [astro-ph].

[161] E. A. Baltz, J. Edsjo, K. Freese and P. Gondolo, arXiv:astro-ph/0211239.

[162] E. A. Baltz, J. Edsjo, K. Freese and P. Gondolo, Phys. Rev. D **65**, 063511 (2002) [arXiv:astro-ph/0109318].

[163] G. L. Kane, L. T. Wang and J. D. Wells, Phys. Rev. D **65**, 057701 (2002) [arXiv:hep-ph/0108138].

[164] J. Hisano, M. Kawasaki, K. Kohri and K. Nakayama, arXiv:0812.0219 [hep-ph]; M. Ibe, H. Murayama and T. T. Yanagida, arXiv:0812.0072 [hep-ph]; M. Taoso, S. Ando, G. Bertone and S. Profumo, arXiv:0811.4493 [astro-ph]; K. Ishiwata, S. Matsumoto and T. Moroi, arXiv:0811.4492 [astro-ph]; K. M. Zurek, arXiv:0811.4429 [hep-ph]; I. Cholis, G. Dobler, D. P. Finkbeiner, L. Goodenough and N. Weiner, arXiv:0811.3641 [astro-ph]; C. R. Chen, F. Takahashi and T. T. Yanagida, arXiv:0811.3357 [astro-ph]; J. Kalinowski, S. F. King and J. P. Roberts, arXiv:0811.2204 [hep-ph]; S. Baek and P. Ko, arXiv:0811.1646 [hep-ph]; A. Ibarra and D. Tran, arXiv:0811.1555 [hep-ph]; M. Pospelov, arXiv:0811.1030 [hep-ph]; E. Ponton and L. Randall, arXiv:0811.1029 [hep-ph]; T. Hur, H. S. Lee and C. Luhn, arXiv:0811.0812 [hep-ph]; K. Hamaguchi, E. Nakamura, S. Shirai and T. T. Yanagida, arXiv:0811.0737 [hep-ph]; C. R. Chen, F. Takahashi and T. T. Yanagida, arXiv:0811.0477 [hep-ph]; P. J. Fox and E. Poppitz, arXiv:0811.0399 [hep-ph]; Y. Bai and Z. Han, arXiv:0811.0387 [hep-ph]; P. f. Yin, Q. Yuan, J. Liu, J. Zhang, X. j. Bi and S. h. Zhu, arXiv:0811.0176 [hep-ph]; D. Feldman, Z. Liu and P. Nath, arXiv:0810.5762 [hep-ph]; R. Harnik and G. D. Kribs, arXiv:0810.5557 [hep-ph]; Y. Nomura and J. Thaler, arXiv:0810.5397 [hep-ph]; I. Cholis, D. P. Finkbeiner, L. Goodenough and N. Weiner, arXiv:0810.5344 [astro-ph]; T. Bringmann, arXiv:0810.5304 [hep-ph]; P. D. Serpico, arXiv:0810.4846 [hep-ph]; E. Nardi, F. Sannino and A. Strumia, arXiv:0811.4153 [hep-ph].

[165] N. Arkani-Hamed, D. P. Finkbeiner, T. Slatyer and N. Weiner, arXiv:0810.0713 [hep-ph]; I. Cholis, L. Goodenough, D. Hooper, M. Simet and N. Weiner, arXiv:0809.1683 [hep-ph]; L. Bergstrom, T. Bringmann and J. Edsjo, arXiv:0808.3725 [astro-ph]; N. Arkani-Hamed and N. Weiner, arXiv:0810.0714 [hep-ph].

[166] M. Nagai and K. Nakayama, Phys. Rev. D **78**, 063540 (2008) [arXiv:0807.1634 [hep-ph]].

[167] K. Ishiwata, S. Matsumoto and T. Moroi, arXiv:0811.0250 [hep-ph].

[168] L. Randall and R. Sundrum, Nucl. Phys. B **557**, 79 (1999) [arXiv:hep-th/9810155]; G. F. Giudice, M. A. Luty, H. Murayama and R. Rattazzi, JHEP **9812**, 027 (1998) [arXiv:hep-ph/9810442].

[169] B. S. Acharya, P. Kumar, K. Bobkov, G. Kane, J. Shao and S. Watson, JHEP **0806**, 064 (2008) [arXiv:0804.0863 [hep-ph]].

[170] M. Cirelli, M. Kadastik, M. Raidal and A. Strumia, arXiv:0809.2409 [hep-ph].

[171] F. Donato, D. Maurin, P. Brun, T. Delahaye and P. Salati, arXiv:0810.5292 [astro-ph].

[172] D. Hooper, A. Stebbins and K. M. Zurek, arXiv:0812.3202 [hep-ph].

[173] P. Gondolo, J. Edsjo, P. Ullio, L. Bergstrom, M. Schelke and E. A. Baltz, New Astron. Rev. **49**, 149 (2005). P. Gondolo, J. Edsjo, P. Ullio, L. Bergstrom, M. Schelke and E. A. Baltz, JCAP **0407**, 008 (2004) [arXiv:astro-ph/0406204].

[174] E. A. Baltz and J. Edsjo, Phys. Rev. D **59**, 023511 (1999) [arXiv:astro-ph/9808243].

[175] Clem, J. M., *et. al.* Astrophysical Journal **v.464**, p.507 (1996).

[176] J. Olzem, H. Gast and S. Schael, Nucl. Phys. Proc. Suppl. **173**, 51 (2007).

[177] Private communication with Igor Moskalenko and Troy Porter.

[178] J. Lavalle, Q. Yuan, D. Maurin and X. J. Bi, arXiv:0709.3634 [astro-ph].

[179] J. F. Navarro *et al.*, arXiv:0810.1522 [astro-ph].

[180] A. W. Strong, I. V. Moskalenko and V. S. Ptuskin, Ann. Rev. Nucl. Part. Sci. **57**, 285 (2007) [arXiv:astro-ph/0701517].

[181] L. Bergstrom, P. Ullio and J. H. Buckley, Astropart. Phys. **9**, 137 (1998) [arXiv:astro-ph/9712318].

[182] S. Dodelson, D. Hooper and P. D. Serpico, Phys. Rev. D **77**, 063512 (2008) [arXiv:0711.4621 [astro-ph]].

[183] N. Fornengo, L. Pieri and S. Scopel, Phys. Rev. D **70**, 103529 (2004) [arXiv:hep-ph/0407342].

[184] A. W. Strong, I. V. Moskalenko and O. Reimer, Astrophys. J. **613**, 962 (2004) [arXiv:astro-ph/0406254].

[185] A. Cesarini, F. Fucito, A. Lionetto, A. Morselli and P. Ullio, Astropart. Phys. **21**, 267 (2004) [arXiv:astro-ph/0305075].

[186] W. de Boer, C. Sander, V. Zhukov, A. V. Gladyshev and D. I. Kazakov, Phys. Lett. B **636**, 13 (2006) [arXiv:hep-ph/0511154].

[187] F. W. Stecker, S. D. Hunter and D. A. Kniffen, Astropart. Phys. **29**, 25 (2008) [arXiv:0705.4311 [astro-ph]].

[188] I. V. Moskalenko, S. W. Digel, T. A. Porter, O. Reimer and A. W. Strong, Nucl. Phys. Proc. Suppl. **173**, 44 (2007) [arXiv:astro-ph/0609768].

[189] H. A. Mayer-Hasselwander *et al.*, Astron. Astrophys. **335**, 161 (1998).

[190] D. Hooper and B. L. Dingus, Phys. Rev. D **70**, 113007 (2004) [arXiv:astro-ph/0210617].

[191] M. Boezio *et al.*, arXiv:0810.3508 [astro-ph]; O. Adriani *et al.*, arXiv:0810.4994 [astro-ph].

[192] F. Donato, N. Fornengo, D. Maurin and P. Salati, Phys. Rev. D **69**, 063501 (2004) [arXiv:astro-ph/0306207].

[193] J. Chang *et al.*, Nature **456**, 362 (2008).

[194] M. Kuhlen, J. Diemand and P. Madau, arXiv:0805.4416 [astro-ph].

[195] V. Springel *et al.*, arXiv:0809.0894 [astro-ph].

[196] S. Profumo, arXiv:0812.4457 [astro-ph].